Magmatic Evolution following Damp Tholeiitic and Wet Calc-alkaline Liquid Lines of Descent: an Eastern Pontides (NE Turkey) Example

JOURNAL OF PETROLOGY

Journal of Petrology, 2021, 1–37
doi: 10.1093/petrology/egaa088
Advance Access Publication Date: 10 September 2020
Original Article

OXFORD

Magmatic Evolution following Damp Tholeiitic and Wet Calc-alkaline Liquid Lines of Descent: an Eastern Pontides (NE Turkey) Example

Ze Liu[1,2], Di-Cheng Zhu[1]*, Oliver Jagoutz[2], Hervé Rezeau[2], Qing Wang[1] and Yener Eyuboglu[3]

[1]State Key Laboratory of Geological Processes and Mineral Resources, and School of Earth Science and Resources, China University of Geosciences, Beijing 100083, China; [2]Department of Earth, Atmospheric and Planetary Sciences, Massachusetts Institute of Technology, Cambridge, MA 02139, USA; [3]Department of Geology, Karadeniz Technical University, Trabzon 61080, Turkey

*Corresponding author. Present address: State Key Laboratory of Geological Processes and Mineral Resources, China University of Geosciences, 29# Xue-Yuan Road, Haidian District, Beijing 100083, China. Telephone: 86 10 8232 2094. Fax: 86 10 8232 2094. E-mail: dchengzhu@163.com or dczhu@cugb.edu.cn

Received 11 September 2019; Accepted 28 August 2020

ABSTRACT

Associations between tholeiitic and calc-alkaline arc magmatism with close spatial and temporal relationships can provide critical constraints on magma genesis and allow the reconstruction of subduction polarity at convergent margins. This study identifies two compositionally distinct intrusive series from the Yusufeli region in the Eastern Pontides arc, NE Turkey. The intrusive rocks from the Yusufeli intrusive complex were emplaced at 179–170 Ma and are dominated by the low- to medium-K tholeiitic series, with depleted Hf isotopic compositions. In contrast, the intrusive rocks from the Camlikaya intrusive complex were emplaced at 151–147 Ma and are characterized by the medium- to high-K calc-alkaline series, with relatively enriched Hf isotopic compositions. The Al-in-hornblende geobarometer reveals that the magmas of both intrusive complexes crystallized at upper crustal levels (~150–250 MPa, ~5–8 km). The presence of patchy-textured plagioclase and the widespread occurrence of coeval dykes and magmatic mafic enclaves indicate that the two intrusive complexes are derived from multiple magma pulses in open magmatic systems. The mineral crystallization order of amphibole and plagioclase, the trace elemental signatures (e.g. Sr/Y and Y), and rare earth element modeling collectively suggest that the Yusufeli intrusive complex was dominated by plagioclase and clinopyroxene fractionation with earlier plagioclase crystallization than amphibole, whereas the Camlikaya intrusive complex was dominated by the fractionation of amphibole accompanied by co-crystallization of plagioclase. Such significant differences in the fractionating mineral assemblages at comparable intrusion pressures can be attributed to different initial H_2O contents of the Yusufeli and Camlikaya parental magmas, which ultimately control their distinct liquid lines of descent. In accord with thermodynamic modeling results derived using the Rhyolite-MELTS software, we propose that the Yusufeli intrusive rocks are derived from damp (~1–2 wt% H_2O) parental magmas formed dominantly by decompression melting of mantle wedge in a back-arc setting. In contrast, the wet parental magmas (>~2 wt% H_2O) of Camlikaya intrusive rocks are more hydrous and formed through flux melting of suprasubduction-zone mantle wedge. This conclusion, combined with the back-arc basin related Jurassic sedimentary and structural records previously determined in the Southern Zone of the Eastern Pontides, indicates that the geochemical compositions and spatial relationship of the Yusufeli and Camlikaya intrusive complexes are preferably explained by the southward subduction of the Paleotethys oceanic lithosphere in the Early to Late Jurassic.

Key words: calc-alkaline; Eastern Pontides; initial H_2O content; liquid line of descent; tholeiitic

INTRODUCTION

At convergent margins, mechanisms of both flux melting induced by dehydration of subducting oceanic lithosphere and decompression melting owing to adiabatically upwelling mantle trigger the production of arc magmas by partial melting of mantle wedge (e.g. Ringwood, 1974; Gill, 1981; Grove *et al.*, 2002, 2012; Jagoutz *et al.*, 2011; Schmidt & Jagoutz, 2017). Flux melting produces wet (>~2 wt% H_2O) parental magmas with significant initial H_2O content (up to 14 wt%; Anderson, 1979; Grove *et al.*, 2012), whereas decompression melting produces dry (<~1 wt% H_2O) and/or damp (~1–2 wt% H_2O) parental melts with a limited amount of initial H_2O content (Grove *et al.*, 2002, 2012; Mandler *et al.*, 2014). It is well known that the differences in initial H_2O content have a strong control over the liquid lines of descent (LLD) of cooling magmas with wet melts following a calc-alkaline differentiation trend and dry or damp melts following a tholeiitic differentiation trend (e.g. Grove & Baker, 1984; Sisson & Grove, 1993; Villiger *et al.*, 2004, 2006; Zimmer *et al.*, 2010; Jagoutz *et al.*, 2011; Nandedkar *et al.*, 2014; Müntener & Ulmer, 2018). This difference arises as higher H_2O content delays plagioclase crystallization and promotes amphibole and Fe-oxide crystallization during magma differentiation (e.g. Osborn, 1959; Sisson & Grove, 1993). In modern arcs (e.g. the Aegean Sea, Cascades, and the Scotia Sea), calc-alkaline magma generally dominates the main arc. However, tholeiitic magma is more common in the back-arc, although both tholeiitic and calc-alkaline magmas can coexist in the fore-arc, main arc, and back-arc (e.g. Hawkesworth *et al.*, 1977; Shervais, 1982; Hunter, 1998; Donnelly-Nolan *et al.*, 2008; Rowe *et al.*, 2009; Schmidt & Jagoutz, 2017; Francalanci & Zellmer, 2019). Thus, the spatial occurrence of arc tholeiitic and calc-alkaline magmas can be used as a paleo-reconstruction indicator of the locations of the main arc and back-arc (e.g. Miyashiro, 1974; Leeman *et al.*, 1990; Hunter & Blake, 1995; Grove *et al.*, 2002, 2009, 2012; Tatsumi *et al.*, 2008; Jagoutz *et al.*, 2011; Schmidt & Jagoutz, 2017).

In the western portion of the Alpine–Himalayan orogenic belt, the Eastern Pontides (NE Turkey) is a continental arc with a length of ~600 km and a width of ~200 km (Fig. 1a). The Jurassic subduction polarity (south versus north dipping) in the Eastern Pontides is highly debated and significantly restricts paleogeodynamic reconstruction of the arc. Two contrasting models have argued that the Eastern Pontides either was formed above the southward subduction of the Paleotethys oceanic lithosphere (e.g. Şengör *et al.*, 1980; Yilmaz *et al.*, 1998; Bektas *et al.*, 2001; Dokuz & Tanyolu, 2006; Dokuz *et al.*, 2010; Eyuboglu *et al.*, 2016; Karsli *et al.*, 2017) or the northward subduction of the northern branch of the Neotethys oceanic lithosphere (e.g. Adamia *et al.*, 1977; Okay & Şahintürk, 1997; Galoyan *et al.*, 2009; Topuz *et al.*, 2013; Okay *et al.*, 2014; Hässig *et al.*, 2017; Rolland *et al.*, 2020). In this paper, we intend to resolve this controversy by studying the petrogenesis and systematic spatio-temporal variation of the Jurassic arc magmatism in the Eastern Pontides.

Yusufeli region in the eastern part of the Eastern Pontides provides an opportunity to discriminate between north- and south-verging subduction as the Jurassic intrusive rocks here are well exposed and show variable geochemical affinities (Boztuğ & Harlavan, 2008; Dokuz *et al.*, 2010; Eyuboglu *et al.*, 2016). Previously, the generation of these rocks has been attributed to partial melting of K_2O-poor and K_2O-rich underplated materials at the base of crust in response to the normal subduction and slab break-off of the southward subduction of the Paleotethys oceanic lithosphere (Dokuz *et al.*, 2010). Alternatively, the partial melting of spinel lherzolite or crustal lithologies could explain Jurassic mafic and felsic rocks in the Yusufeli region, respectively. This partial melting is hypothesized to be a result of slab rollback of southward subducting Paleotethys oceanic lithosphere (Eyuboglu *et al.*, 2016). This study recognizes two compositionally distinct Jurassic intrusive complexes in the Yusufeli region: the Early–Middle Jurassic Yusufeli tholeiitic intrusive complex and the Late Jurassic Camlikaya calc-alkaline intrusive complex. Here, we present new petrographic observations combined with *in situ* zircon U–Pb and Hf isotopic data, as well as whole-rock and mineral geochemistry from the Yusufeli and Camlikaya intrusive complexes. Our new data and modeling results allow us (1) to identify distinct geochemical differentiation paths for each intrusive complex, (2) to present quantitative *P–T* constraints for magma crystallization in crustal magma chambers, (3) to provide relative estimates of the initial H_2O contents of the parental magmas that formed the two intrusive complexes, and (4) to reconstruct the Jurassic subduction polarity in combination with regional sedimentary and structural records.

GEOLOGICAL BACKGROUND

Regional geology

The northward convergence of Arabia with respect to Eurasia led to the formation of the Eastern Turkish Plateau (also known as the Eastern Anatolian Plateau), with an average elevation of ~2 km (e.g. Dewey *et al.*, 1973; Şengör *et al.*, 2008). From north to south, the Eastern Turkish Plateau consists of the Eastern Pontides, Eastern Taurides, and Arabian Platform, which are separated by the İzmir–Ankara–Erzincan (IAE) suture zone in the north and the Bitlis–Zagros fold–thrust (BZ) suture zone in the south, respectively

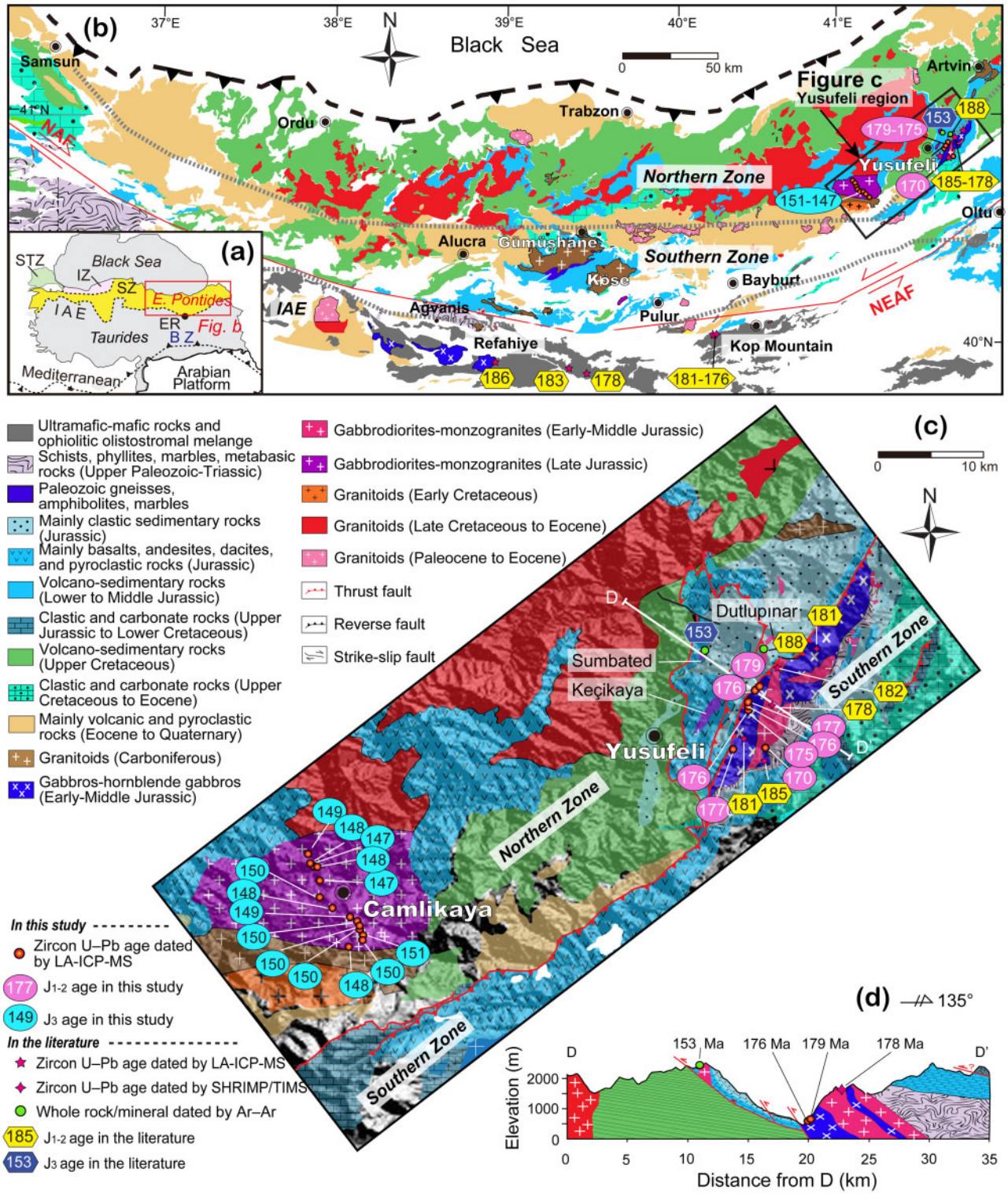

Fig. 1. (a) Tectonic framework of Turkey showing its major subdivisions (Şengör & Yilmaz, 1981). BZ, Bitlis–Zagros suture; ER, Erzincan; IAE, İzmir–Ankara–Erzincan suture zone; IZ, Istanbul Zone; STZ, Strandja Zone; SZ, Sakarya Zone. (b) Simplified geological map of the Eastern Pontides. The two thick gray dotted lines separate the Eastern Pontides into Northern Zone and Southern Zone. NAF, North Anatolian fault; NEAF, Northeast Anatolian fault. (c) Geological map of the Yusufeli region, modified from Eyuboglu *et al.* (2016). The zircon U–Pb isotopic ages from this study (ovals with numerals) are listed in Table 2. The zircon U–Pb and hornblende ^{40}Ar–^{39}Ar ages in the literature (hexagons with numerals) are from Dokuz *et al.* (2010), Topuz *et al.* (2013), Uysal *et al.* (2015) and Eyuboglu *et al.* (2016). (d) Geological cross-section showing field relationships of the intrusive rocks and volcano-sedimentary strata in the Yusufeli region.

(Fig. 1a) (e.g. Okay & Tüysüz, 1999; Parlak, 2016). From west to east, the Pontides includes the Strandja Zone (STZ), the İstanbul Zone (IZ), and the Sakarya Zone (SZ), and the Eastern Pontides is located in the eastern SZ (Fig. 1a). The Eastern Pontides is interpreted as a continental margin that has been active since the Late Paleozoic. This is based on an interpreted sedimentary protolith for most pre-Permian metamorphic massifs (e.g. Pulur and Ağvanis) (Okay, 1984; Topuz *et al.*, 2004) and a transition of Upper Jurassic–Lower Cretaceous sedimentary strata from platform carbonate deposition in the north to pelagic carbonates and calciturbidites in the south (Okay & Şahintürk, 1997). The basement rocks of the Eastern Pontides consist of Carboniferous intrusive rocks (e.g. Gümüşhane and Köse batholiths), Carboniferous–Permian metamorphic massifs (e.g. Pulur and Ağvanis massifs), and Late Carboniferous–Early Jurassic Alaskan-type ultramafic–mafic intrusions (e.g. Topuz *et al.*, 2004, 2007; Dokuz, 2011; Eyuboglu *et al.*, 2016; Kaygusuz *et al.*, 2016). The aforementioned basement lithologies are unconformably overlain by Lower Jurassic–Eocene volcano-sedimentary strata and sporadic Neogene–Quaternary volcanic rocks (e.g. Güven, 1993; Korkmaz *et al.*, 1995; Eyuboglu, 2015). Based on different sedimentary facies, igneous rock assemblages, and structural characteristics, the Eastern Pontides can be further divided into the Northern Zone, dominated by abundant Late Cretaceous–Eocene intrusive and volcanic rocks, and the Southern Zone, characterized by widespread Jurassic igneous rocks and Eocene volcano-sedimentary strata (Fig. 1b) (e.g. Güven, 1993; Bektas *et al.*, 1995; Arslan & Aliyazıcıoğlu, 2001; Eyuboglu *et al.*, 2007, 2017; Kaygusuz *et al.*, 2014; Dokuz *et al.*, 2017; Liu *et al.*, 2018). In the south, the IAE suture zone consists of Silurian–Jurassic gabbros and diorites, serpentinized ultramafic–mafic massifs of unknown age (e.g. Erzincan and Kop Mountain), Middle–Upper Cretaceous ophiolitic olistostromal mélanges, and Miocene volcanic and associated pyroclastic rocks (e.g. Eyuboglu *et al.*, 2010, 2016; Topuz *et al.*, 2013; Uysal *et al.*, 2015).

Geology of the Yusufeli region

The Yusufeli region is located at the transition between the Northern Zone and Southern Zone in the Eastern Pontides (Fig. 1b). Late Paleozoic granitoids, gneisses, amphibolites, and schists constitute the local crystalline basement rocks (Fig. 1c) (Ustaömer *et al.*, 2013; Eyuboglu *et al.*, 2016), and are unconformably overlain by Lower to Middle Jurassic volcano-sedimentary strata (Hamurkesen Formation) comprising two units (e.g. Dokuz & Tanyolu, 2006; Şen 2007; Koch *et al.*, 2008; Kandemir & Yılmaz 2009). The lower unit is characterized by lacustrine sediments, interbedded with pillow basalt, massive basalt, and basaltic andesite. The upper unit represents shallow-marine sediments and undergoes a transition southwards to deep-marine sediments, with large lateral and vertical variations in both bed thickness and grain size (e.g. Robinson et al., 1995; Okay & Şahintürk, 1997; Yilmaz *et al.*, 1998; Dokuz & Tanyolu, 2006). These sediments were accumulated in basins bounded by conjugate normal fault systems (Eyuboglu, 2006), which are cross-cut by syn-extensional neptunian dykes (Bektas *et al.*, 2001). Such sedimentary and structural observations are interpreted as evidence for a back-arc basin setting (e.g. Şengör *et al.*, 1980; Dokuz & Tanyolu, 2006). The Upper Jurassic–Lower Cretaceous (Berdiga Formation) strata consist of shallow-marine platform carbonates with minor clastic sedimentary rocks. All these sediments are uncomfortably overlain by Eocene conglomerates and sandstones as a result of regional exhumation since ~13 Ma (Ballato *et al.*, 2018).

The Yusufeli region hosts two intrusive complexes (Fig. 1c): the Early–Middle Jurassic Yusufeli intrusive complex (~200 km^2), emplaced into the Carboniferous granitic crustal basement, and the Late Jurassic Camlikaya intrusive complex (~250 km^2), emplaced into the Upper Paleozoic–Triassic metamorphic basement. These two intrusive complexes consist of gabbrodiorite, diorite, tonalite, granodiorite, and monzogranite. Additionally, the Yusufeli intrusive complex contains gabbro and hornblende gabbro. Both intrusive complexes are cross-cut by (gabbro-) dioritic and rhyolitic dykes (Dokuz *et al.*, 2010; Eyuboglu *et al.*, 2016). Published zircon U–Pb and hornblende ^{40}Ar–^{39}Ar dates constrain emplacement at 185–178 Ma for the Yusufeli intrusive complex (Fig. 1c) (Eyuboglu *et al.*, 2016). Three small intrusions (<4 km^2), the Dutlupınar, Sumbated, and Keçikaya intrusions, comprising diorite, monzodiorite, quartz monzodiorite, tonalite, and granodiorite are exposed in the west of the Yusufeli intrusive complex (Fig. 1c). The Dutlupınar and Sumbated intrusions have been dated at 188 ± 4 Ma and 153 ± 3 Ma by hornblende ^{40}Ar–^{39}Ar dating, respectively (Dokuz *et al.*, 2010).

FIELD OBSERVATIONS AND PETROGRAPHY

The descriptions of 26 intrusive rocks, representative of the Yusufeli and Camlikaya intrusive complexes, are listed in Table 1 and illustrated in Figs 2 and 3. The mineral proportions (%) were visually estimated from petrographic observations.

The Yusufeli intrusive complex

The Yusufeli intrusive complex is composed of gabbro, hornblende gabbro, gabbrodiorite, diorite, tonalite, granodiorite, and monzogranite intrusions. Most intrusions are cross-cut by widespread gabbrodioritic dyke and rhyolitic dykes (Table 1). The rhyolitic dykes represent the final stage of the Early–Middle Jurassic magmatic activity in the Yusufeli region (Eyuboglu *et al.*, 2016). In the field, the presence of rhyolitic dykes cross-cutting the pre-Jurassic pillow basalts indicates that the Yusufeli intrusive complex has been exhumed and tilted to the surface in the Middle Jurassic (Fig. 2c)

Table 1: A summary of petrographic descriptions of the intrusive rocks in the Yusufeli and Camlikaya intrusive complexes

Sample	Rock type	Latitude (°N)	Longitude (°E)	Mineral proportion (%)					Accessory	
				Cpx	Pl	Hbl	Bt	Kfs	Qz	
Yusufeli intrusive complex										
16TK32-4	Cumulate hornblende gabbro	40·8407	41·6728	3–5	50–60	30–45	—	—	—	Act, Ap, Chl, Prg, Zrn, and Ilm
16TK33-1	Cumulate hornblende gabbro	40·8569	41·7003	3–5	50–60	30–45	—	—	—	Act, Ap, Chl, Prg, Zrn, and Ilm
16TK33-3	Cumulate hornblende gabbro	40·8559	41·7004	3–5	50–60	30–45	—	—	—	Act, Ap, Chl, Prg, Zrn, and Ilm
16TK32-3	Hornblende gabbro	40·8407	41·6728	3–5	55–60	30–35	1–3	3–5	1–3	Ap, Chl, Zrn, and Ilm
16TK32-2	Gabbrodioritic dyke	40·8407	41·6728	—	55–60	25–30	3–5	3–5	1–3	Ap, Chl, Zrn, Ilm, Ttn, and Mag
16TK33-2	Diorite	40·8559	41·7004	—	55–60	25–30	1–3	0–5	3–5	Ap, Chl, Cum, Ep, Zo, Zrn, Ilm, Ttn, and Mag
16TK33-4	Tonalite	40·8559	41·7004	—	55–60	15–20	—	0–5	10–15	Ap, Chl, Ep, Zo, Zrn, Ilm, Ttn, and Mag
16TK32-1	Monzogranite	40·8407	41·6728	—	40–45	5–15	—	15–25	20–30	Ap, Zrn, Ilm, Ttn, and Mag
16TK34-1	Monzogranite	40·8013	41·6530							
16TK35-1	Rhyolitic dyke	40·7840	41·6912	—	30–35	5–10	—	30–35	20–25	Chl, Zrn, Ilm, Ttn, and Mag
Camlıkaya intrusive complex										
16TK48-3	Gabbrodiorite	40·6867	41·1273	—	55–65	20–35	1–3	3–5	3–5	Ap, Ep, Ser, Zo, Zrn, Ilm, Ttn, and Mag
16TK53-2	Gabbrodiorite	40·6338	41·1764	—	55–65	20–35	1–3	3–5	3–5	Ap, Ep, Ser, Zo, Zrn, Ilm, Ttn, and Mag
16TK53-3	Gabbrodiorite	40·6338	41·1764	—	55–65	20–35	1–3	3–5	3–5	Ap, Ep, Ser, Zo, Zrn, Ilm, Ttn, and Mag
16TK48-2	Gabbrodioritic MME	40·6867	41·1273	—	60–65	25–30	3–5	3–5	3–5	Act, Ap, Zrn, Ilm, Ttn, and Mag
16TK55-2	Dioritic dyke	40·6182	41·1823	—	50–60	20–25	0–5	5–10	3–5	Ap, Chl, Zrn, Ilm, Ttn, and Mag
16TK54-2	Dioritic dyke	40·6317	41·1792	—	50–60	20–25	0–5	5–10	3–5	Ap, Chl, Zrn, Ilm, Ttn, and Mag
16TK47-1	Tonalite	40·6962	41·1232	—	35–40	5–20	0–10	10–15	10–20	Ap, Chl, Ep, Zo, Zrn, Ilm, Ttn, and Mag
16TK49-1	Tonalite	40·6718	41·1304	—	35–40	5–20	0–10	10–15	10–20	Ap, Chl, Ep, Zo, Zrn, Ilm, Ttn, and Mag
16TK53-4	Tonalite	40·6338	41·1764	—	35–40	5–20	0–10	10–15	10–20	Ap, Chl, Ep, Zo, Zrn, Ilm, Ttn, and Mag
16TK54-1	Tonalite	40·6317	41·1792	—	35–40	5–20	0–10	10–15	10–20	Ap, Chl, Ep, Zo, Zrn, Ilm, Ttn, and Mag
16TK48-1	Granodiorite	40·6867	41·1273	—	30–40	5–20	0–10	15–20	20–25	Ap, Chl, Ep, Zo, Zrn, Ilm, Ttn, and Mag
16TK50-1	Granodiorite	40·6566	41·1368	—	30–40	5–20	0–10	15–20	20–25	Ap, Chl, Ep, Zo, Zrn, Ilm, Ttn, and Mag
16TK51-1	Granodiorite	40·6476	41·1496	—	30–40	5–20	0–10	15–20	20–25	Ap, Chl, Ep, Zo, Zrn, Ilm, Ttn, and Mag
16TK55-1	Granodiorite	40·6182	41·1823	—	30–40	5–20	0–10	15–20	20–25	Ap, Chl, Ep, Zo, Zrn, Ilm, Ttn, and Mag
16TK52-1	Monzogranite	40·6378	41·1728	—	25–30	5–20	0–5	20–25	25–30	Ap, Chl, Ep, Zo, Zrn, Ilm, Ttn, and Mag
16TK53-1	Monzogranite	40·6338	41·1764	—	25–30	5–20	0–5	20–25	25–30	Ap, Chl, Ep, Zo, Zrn, Ilm, Ttn, and Mag

Act, actinolite; Ap, apatite; Bt, biotite; Chl, chlorite; Cpx, clinopyroxene; Cum, cummingtonite; Ep, epidote; Hbl, hornblende; Ilm, ilmenite; Kfs, K-feldspar; Mag, magnetite; Pl, plagioclase; Prg, pargasite; Qz, quartz; Ser, sericite; Ttn, titanite; Zo, zoisite; Zrn, zircon.

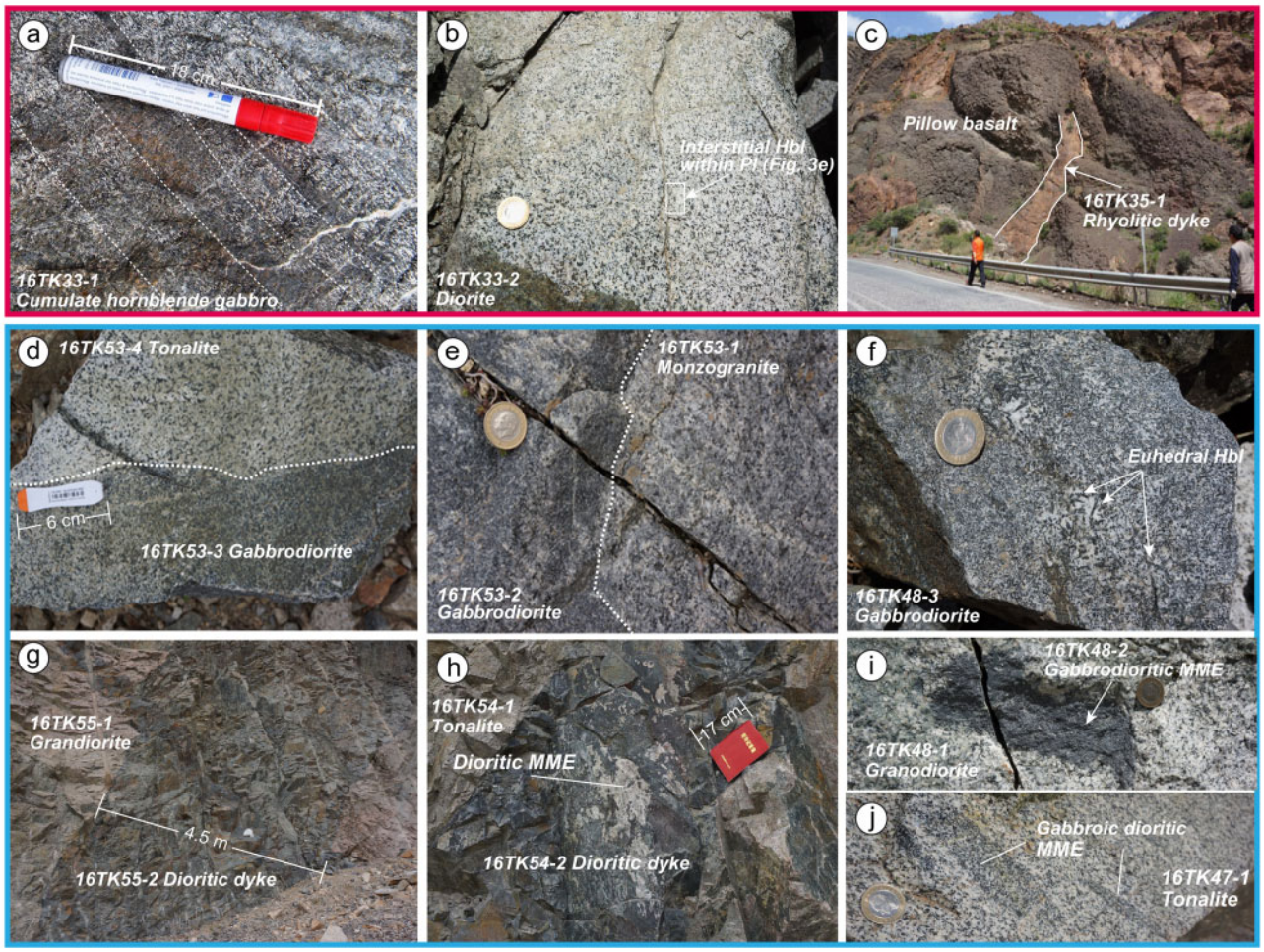

Fig. 2. Field photographs of representative cumulate hornblende gabbro, diorite, and rhyolitic dyke samples exposed in the Yusufeli intrusive complex (a–c) and representative gabbrodiorite, tonalite, granodiorite, monzogranite, dioritic dyke and MME, and gabbrodioritic MME samples exposed in the Camlikaya intrusive complex (d–j). The white dotted lines in (a) indicate the orientation of the mineral cumulate layer. (See text for detailed descriptions.)

(Eyuboglu *et al.*, 2016). The intrusive complex was thrust over the Upper Jurassic–Lower Cretaceous clastic rocks and the Lower–Middle Jurassic and the Upper Cretaceous volcanic rocks on regional NE–SW Eocene faults (south-dipping) (Fig. 1c and d).

In the field, fine- to medium-grained (~0·1–2 mm) hornblende gabbro intrusions can be divided into two types. The first type of hornblende gabbro displays a layered cumulate texture (~2–10 mm wide for each layer) (Fig. 2a), defined by the crystal preferred orientation of plagioclase (Fig. 3a). The cumulate hornblende gabbro is dominantly composed of fine-grained plagioclase (50–60 %), hornblende (30–45 %), and minor clinopyroxene (3–5 %). The occurrence of resorbed clinopyroxene inclusions in hornblende suggests the growth of hornblende at the expense of clinopyroxene (clinopyroxene + melt = hornblende; Fig. 3b). Tabular plagioclase also occurs as inclusions in hornblende (Fig. 3c). The second type of hornblende gabbro lacks a cumulate texture. Instead, it is characterized by a subophitic texture (i.e. hornblende embraced by plagioclase), and contains fine-grained plagioclase (55–60 %), hornblende (30–35 %), clinopyroxene (3–5 %), K-feldspar (1–3 %), biotite (1–3 %), and quartz (1–3 %). In both types of hornblende gabbro, plagioclase displays a euhedral habit, and hornblende is interstitial to plagioclase, indicating that the hornblende crystallized later than plagioclase (Fig. 3a). Some of the (cumulate) hornblende gabbros are cross-cut by gabbrodioritic dykes, which vary in width from 10 cm to 2 m and are composed of hornblende phenocrysts (25–30 %), with plagioclase (55–60 %), biotite (3–5 %), K-feldspar (3–5 %), and quartz (1–3 %) in the matrix.

Some diorite intrusions cross-cut the massive (cumulate) hornblende gabbros with sharp margins, indicating that one unit cooled and crystallized before the next intrusive event. Diorite intrusions generally display fine- to medium-grained (~0·2–2 mm) textures (Fig. 2b) dominated by plagioclase (55–60 %) and hornblende (25–30 %), together with minor quartz (3–5 %),

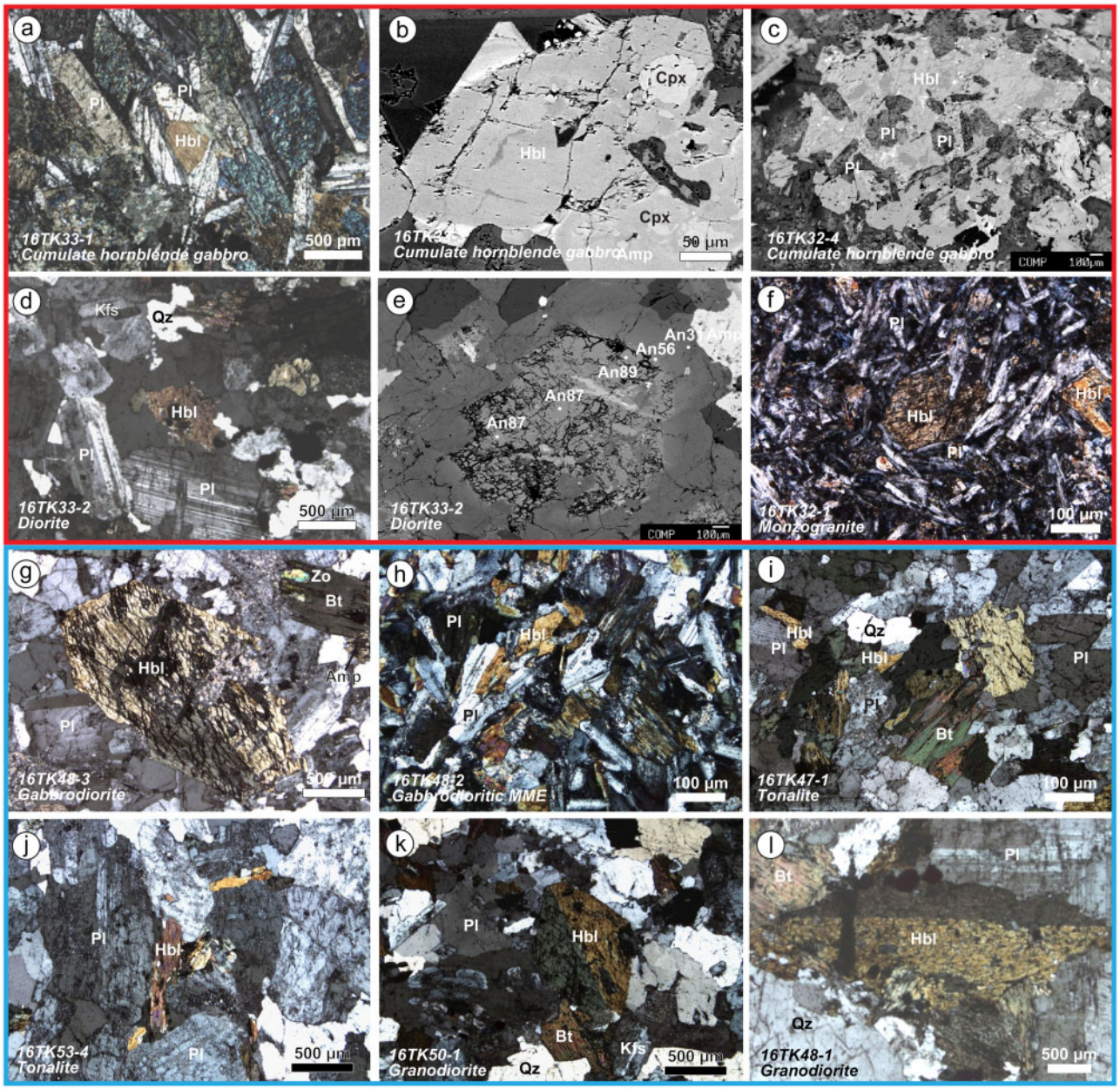

Fig. 3. Photomicrographs of thin-section and backscattered electron (BSE) images showing representative textures of the Yusufeli (a–f) and Camlikaya (g–l) intrusive rocks. Bt, biotite; Cpx, clinopyroxene; Hbl, hornblende; Kfs, K-feldspar; MME, magmatic mafic enclaves; Pl, plagioclase; Qz, quartz; Zo, zoisite. (See text for detailed descriptions.)

K-feldspar (3–5 %), and biotite (1–3 %). The anhedral hornblende and quartz crystals are interstitial to plagioclase (Figs 2b and 3d).

Tonalite intrusions have fine-grained (∼0·1–1 mm) textures and consist of plagioclase (55–60 %), hornblende (15–20 %), quartz (10–15 %), and minor K-feldspar (0–5 %). All anhedral hornblende crystals are interstitial to euhedral plagioclase crystals.

Monzogranite intrusions typically have fine-grained (∼0·1–1 mm) textures, although in some places, they display a porphyritic (∼1–2 mm plagioclase and amphibole phenocrysts) texture (Fig. 3f). They are composed of plagioclase (40–45 %), quartz (20–30 %), K-feldspar (15–25 %), and hornblende (5–15 %).

Rhyolitic dykes cross-cut most of the intrusions emplaced in the area. These dykes are composed of 20–25 % quartz phenocrysts (∼1–2 mm), with 30–35 % K-feldspar, 30–35 % plagioclase, and 5–10 % hornblende constituting the fine-grained matrix (<0·2 mm).

Accessory phases in the Yusufeli intrusive complex comprise apatite, pargasite, zircon, ilmenite, titanite, and magnetite, which are listed for each sample in Table 1. Deuteric actinolite, cummingtonite, epidote, chlorite, and zoisite are metamorphic in origin. Based

on mineral and textural relationships, we constrain the magmatic mineral differentiation sequence in the Yusufeli intrusive complex to clinopyroxene → plagioclase → hornblende → biotite → K-feldspar + quartz.

The Camlikaya intrusive complex

The Camlikaya intrusive complex mainly consists of gabbrodiorite, diorite, tonalite, granodiorite, and monzogranite intrusions, as well as dioritic dykes (Table 1). Sharp contact boundaries between all these intrusion phases are well exposed in the field (Fig. 2d and e).

The gabbrodiorite intrusions exhibit fine- to medium-grained (~0·3–3 mm) textures and are composed of plagioclase (55–65 %), hornblende (20–35 %), K-feldspar (3–5 %), quartz (3–5 %), and biotite (1–3 %). Both euhedral and anhedral hornblende crystals are observed to be interspersed with plagioclase and biotite, suggesting that hornblende crystallized before or with plagioclase (Figs 2f and 3g). Gabbrodiorite magmatic mafic enclaves (MMEs) range in size from a few centimeters to a half meter in length and are widespread in the granodiorite, tonalite, and monzogranite intrusions (Fig. 2i and j). The gabbrodioritic MMEs consist of plagioclase (60–65 %), hornblende (25–30 %), biotite (3–5 %), quartz (3–5 %), and K-feldspar (3–5 %) (Fig. 3h).

Numerous dioritic dykes, varying in width from 5 cm to 4·5 m, cross-cut tonalite, granodiorite, and monzogranite intrusions (Fig. 2g and h). They all show porphyritic textures, with quartz and hornblende phenocrysts (~1–2 mm) embedded in a fine-grained matrix (<0·1 mm) composed of 50–60 % plagioclase, 20–25 % hornblende, 5–10 % K-feldspar, 3–5 % quartz, and 0–5 % biotite.

Tonalite intrusions are fine- to medium-grained (<0·1–2 mm) and are composed of plagioclase (35–40 %), K-feldspar (10–15 %), quartz (10–20 %), hornblende (5–20 %), and biotite (0–10 %) (Table 1). Anhedral hornblende crystals are interstitial to the euhedral to subhedral plagioclase (Fig. 3i and j).

Fine- to medium-grained (~0·5–5 mm) granodiorite and monzogranite intrusions show similar mineral assemblages of 25–40 % plagioclase, 20–30 % quartz, 15–25 % K-feldspars, 5–20 % hornblende, and 0–10 % biotite (Fig. 3k). Some euhedral hornblende crystals in the granodiorites display resorbed textures (Fig. 3l).

In the Camlikaya intrusive complex, accessory phases comprise deuteric apatite, zircon, ilmenite, titanite, and magnetite (Table 1). Actinolite, epidote, chlorite, zoisite, and sericite are of metamorphic origin. Based on mineral and textural relationships, we constrain the mineral differentiation sequence in the Camlikaya intrusive complex to hornblende + plagioclase → biotite → K-feldspar + quartz.

ANALYTICAL METHODS

Zircon LA-ICP-MS U–Pb and Hf isotope data

Zircons crystallized in the Yusufeli and Camlikaya intrusive complexes were separated using standard heavy liquid techniques and mounted in epoxy. A Tescan MIRA 3 field emission scanning electron microscope (SEM) was used for collecting detailed cathodoluminescence (CL) images using operating conditions of 4 nA and 15 kV at Beijing Zhongke Kuangyan Test Technology Co., Ltd. Zircon laser ablation inductively coupled plasma mass spectrometry (LA-ICP-MS) U–Pb dating was carried out at the Mineral Laser Microprobe Analysis Laboratory (Milma Lab), China University of Geosciences, Beijing (CUGB), China. Laser sampling was performed using a NewWave 193^{UC} excimer laser ablation system. The ablated material was transported by a carrier gas into the plasma source of an Agilent 7900 ICP-MS system. Detailed setting parameters for the instruments and experimental process have been given by Zhang *et al.* (2019). Zircon standard 91500 was used as an external standard for U–Pb dating. Zircon standards GJ-1 and Plesovice were analyzed as unknown samples inserted between 91500 and the samples (i.e. two 91500 + one GJ-1 + one Plesovice + six zircon samples + two 91500) to control the analytical reproducibility. Time-dependent drifts of U–Th–Pb isotopic ratios were corrected using linear interpolation (with time) for every 10 analyses based on the variations of 91500. The detailed calibration formula and the calculation of standard error have been given by Liu *et al.* (2010). NIST SRM 610 was used as an external standard for U, Th, and Pb contents calibration. The NIST SRM 610 was analyzed every 20 analyses to correct for the mass discrimination and time-drift of sensitivity for the analyses of U, Th, and Pb. Off-line selection and integration of background and analyte signals, time-drift correction, quantitative calibration for U, Th, and Pb contents, and U–Pb dating were performed using ICPMSDataCal software. Common Pb corrections were calculated using ComPbCorr#3.17 (Andersen, 2002). Concordia diagrams and $^{206}Pb/^{238}U$ weighted mean plots were made using the Isoplot software (Ludwig, 2011).

The weighted mean $^{206}Pb/^{238}U$ ages for 91500, GJ-1, and Plesovice are 1062·0 ± 1·6 Ma (2σ, $n = 132$; MSWD = 0·3), 600·8 ± 1·0 Ma (2σ, $n = 72$; MSWD = 0·5), and 337·2 ± 0·5 Ma (2σ, $n = 69$; MSWD = 0·5), respectively, which are in good agreement with the recommended values of Wiedenbeck *et al.* (1995), Jackson *et al.* (2004), and Sláma *et al.* (2008) (Supplementary Data Electronic Appendix 1 and Supplementary Data Fig. S1; supplementary data are available for downloading at http://www.petrology.oxfordjournals.org). The reported errors in Table 2 are presented as '$2\sigma_{sample + std.}$', which correspond to the propagation of analytical uncertainties from the measurements on the sample (two standard deviations, 2σ) and the reproducibility of the measurements on standards GJ-1 and Plesovice. For each sample, the mean square weighted deviation (MSWD) and the weighted mean of single $^{206}Pb/^{238}U$ analyses are calculated from all concordant zircon grains (concordance between 98 and 102 %). The weighted mean $^{206}Pb/^{238}U$ age is interpreted as the magma crystallization age (Table 2).

Table 2: A summary of zircon U–Pb age and Hf results of the intrusive rocks in the Yusufeli and Camlikaya intrusive complexes

Sample	U (μg/g)	Th/U	Weighted mean of $^{206}Pb/^{238}U$ age (Ma)	$2\sigma_{sample + std}$	Number of analyses	Age range (Ma)	$\varepsilon_{Hf}(t)$
Yusufeli intrusive complex							
16TK32-3	460–1914	0·72–2·33	175·4 (MSWD = 0·5)	0·7	13 out of 18	177·3 to 174·3	+8·1 to +12·3
16TK32-4	35–101	0·53–1·07	176·8 (MSWD = 0·4)	2·0	6 out of 12	178·0 to 172·8	+10·4 to +14·6
16TK33-2	113–669	0·59–1·77	176·0 (MSWD = 0·7)	1·0	11 out of 18	177·9 to 173·6	+10·3 to +12·9
16TK33-4	69–712	0·50–1·38	178·8 (MSWD = 2·6)	2·4	7 out of 22	185·0 to 176·6	+8·4 to +12·6
16TK32-1	320–421	0·70–1·07	176·3 (MSWD = 0·4)	1·0	10 out of 23	176·5 to 168·7	+10·9 to +13·3
16TK34-1	1135–2844	2·57–4·86	176·5 (MSWD = 1·0)	1·0	7 out of 24	181·1 to 171·6	+11·2 to +15·8
16TK35-1	182–801	0·72–1·32	170·1 (MSWD = 1·9)	1·6	13 out of 27	177·6 to 174·5	+8·5 to +12·9
Camlıkaya intrusive complex							
16TK48-2	405–2431	0·31–2·48	147·2 (MSWD = 7·7)	1·4	23 out of 41	155·0 to 142·4	+6·4 to +10·3
16TK48-3	519–2928	0·30–1·11	148·2 (MSWD = 1·2)	0·6	18 out of 30	150·4 to 145·6	+6·0 to +8·3
16TK53-2	184–1280	0·31–1·70	150·3 (MSWD = 4·9)	1·0	33 out of 42	156·3 to 144·8	+7·2 to +12·2
16TK54-2	56–122	0·65–0·99	150·3 (MSWD = 0·03)	1·4	9 out of 18	150·7 to 149·5	+6·8 to +9·1
16TK49-1	157–245	0·48–0·77	146·9 (MSWD = 1·4)	1·6	8 out of 18	148·7 to 143·8	+5·3 to +7·3
16TK47-1	89–242	0·70–1·15	149·0 (MSWD = 0·8)	1·1	11 out of 18	153·1 to 147·2	+6·6 to +8·7
16TK53-4	155–546	0·57–0·85	150·4 (MSWD = 0·6)	0·9	11 out of 18	152·9 to 147·5	–
16TK54-1	236–497	0·61–0·84	150·6 (MSWD = 0·5)	1·0	7 out of 18	152·6 to 149·6	+7·7 to +9·2
16TK50-1	292–687	0·54–0·98	149·6 (MSWD = 0·04)	0·8	9 out of 17	149·9 to 149·3	+4·8 to +7·8
16TK51-1	252–656	0·54–0·83	148·0 (MSWD = 0·3)	0·8	9 out of 18	149·4 to 147·3	–
16TK48-1	288–909	0·41–1·65	147·9 (MSWD = 2·3)	2·1	6 out of 18	150·9 to 146·2	+4·1 to +8·1
16TK55-1	166–544	0·55–1·13	148·4 (MSWD = 0·8)	0·8	12 out of 18	150·8 to 146·5	+6·9 to +8·9
16TK53-1	245–647	0·51–0·83	150·3 (MSWD = 0·3)	0·7	12 out of 18	150·8 to 148·1	+6·9 to +9·3
16TK52-1	336–822	0·58–1·00	149·4 (MSWD = 0·2)	0·6	15 out of 24	150·4 to 148·2	+4·9 to +8·8

$2\sigma_{sample + std}$ is composed of the propagation of analytical uncertainties from the measurements on sample (two standard deviations, 2σ) and the reproducibility of the measurements on standards GJ-1 and Plesovice. (See details of zircon U–Pb and Hf isotopic compositions in Supplementary Data Electronic Appendix 1 and Supplementary Data Electronic Appendix 2, respectively.) MSWD, mean square weighted deviation.

In situ zircon Hf isotopic analyses were conducted using a Neptune Plus multicollector (MC-)ICP-MS system and a NewWave 193^{UC} excimer laser ablation system at Milma Lab, CUGB. The beam diameter used was 35 μm, with 8 Hz frequency and 3·7 J cm^{-2} energy density. Makeup gas of argon and carrier gas of helium with the addition of nitrogen were mixed before introduction into the MC-ICP-MS system. A gentle re-polish was conducted prior to the Hf isotopic analysis. All the ablation pits for Hf isotope analysis coincide with spots used for U–Pb dating. Zircon 91500 was used as an external standard for correcting mass discrimination and time-drift (Blichert-Toft, 2008). Zircon standard Plesovice (Sláma *et al.*, 2008) and GJ-1 (Morel *et al.*, 2008) were analyzed as unknown samples that were regularly measured between zircon 91500 and the samples. For each sample, we analyzed 91500, GJ-1, and Plesovice every nine unknown analyses (i.e. one 91500 + one GJ-1 + one Plesovice + nine zircon samples + one 91500). Interference correction for Yb and Lu is important for precise *in situ* measurements of zircon Hf isotopes (Woodhead *et al.*, 2004). Applying an exponential fractionation law (Russell *et al.*, 1978), the mass fractionations of Hf and Yb were calculated using values of 0·7325 for $^{179}Hf/^{177}Hf$ and 1·1248 for $^{173}Yb/^{171}Yb$ (Blichert-Toft *et al.*, 1997). Because Lu and Yb have similar physicochemical properties, the mass fractionation of Yb was used to correct the mass fractionation of Lu. Using the calculated mass fractionation of Yb, the fractionation-corrected $^{176}Hf/^{177}Hf$ ratios of the samples were then calibrated against 91500 using the recommended $^{176}Hf/^{177}Hf$ ratio of 0·282308 ± 0·000006 (2σ) (Blichert-Toft, 2008). The correction factor is 0·46 ± 0·03 %. Finally, off-line selection and integration of background and analyte signals, and interference and mass fractionation correction and external calibration of Lu–Hf isotopic ratios were performed using Iolite software. The detailed operation procedure has been described by Paton *et al.* (2011). Initial isotopic ratios were calculated for the corresponding crystallization age of each zircon grain. The weighted mean $^{176}Hf/^{177}Hf$ ratios for 91500, GJ-1, and Plesovice are 0·282304 ± 0·000007 (2σ, $n = 41$; MSWD = 0·3), 0·282477 ± 0·000005 (2σ, $n = 38$; MSWD = 0·6), and 0·282011 ± 0·000007 (2σ, $n = 38$; MSWD = 0·4), respectively, which are consistent with the recommended values of Blichert-Toft (2008), Morel *et al.* (2008), and Sláma *et al.* (2008) (Supplementary Data Electronic Appendix 2 and Supplementary Data Fig. S2). These results indicate that direct *in situ* measurements of zircon Hf isotopes on the same pit as used for U–Pb dating do not affect Hf isotopic data.

Whole-rock major and trace elemental data

Approximately 1 kg of fresh sample was crushed, and about 0·5 g of rock powder was mixed with 5 g compound flux ($LiBO_2$ and $Li_2B_4O_7$) and fused in a Au–Pt crucible by heating at 1050 °C for 10 min. The homogenized mixture was then poured into a mold to form a flat disc. Whole-rock major element compositions were determined by X-ray fluorescence spectroscopy (XRF)

at the State Key Laboratory of Geological Processes and Mineral Resources, China University of Geosciences (Wuhan) (CUGW). For the whole-rock trace element analyses, the rock powders (~100 mg) were dissolved in a Teflon bomb with HNO_3 and HF mixture, and then the mixture was heated at 180 °C for 24 h. After evaporating the solution, the sample was redissolved using 30 % HNO_3, and then heated at 180 °C for 24 h. Finally, the solution was diluted to ~100 g with 2 % HNO_3 for analysis. We used ICP-MS (Elan 6100 DRC) to determine the trace elements at CUGW, and the standards BHVO-2, BCR-2, AGV-1, and G-2 were used to monitor the data quality.

Mineral geochemistry

We used a JEOL JXA-8200 Superprobe electron probe micro-analyzer (EPMA) to obtain mineral chemical compositions and back-scattered electron (BSE) images at Massachusetts Institute of Technology, Cambridge, USA. An accelerating voltage of 15 kV, a beam current of 10 nA, and 40–60 s counting times per element (10 s for Na) were used for wavelength-dispersive spectrometry (WDS) to analyze minerals. We used a 10 μm beam diameter for hydrous minerals and plagioclase, and used a focused beam (1 μm) for small grains. For anhydrous minerals, such as clinopyroxene, the focused beam (1 μm) was applied. The standard deviation (1σ) of counts is between 0·5 and 1 %, and all the raw data were corrected for matrix effects by the CITZAF package (Armstrong, 1995).

RESULTS

Zircon isotope geochemistry

U–Pb age and Hf isotopic data, and zircon CL images are given in Table 2 and Figs 4–6. The detailed U–Pb dating and Hf isotopic results and concordia diagrams of standards and samples can be found in Supplementary Data Electronic Appendixes 1 and 2 and Supplementary Data Fig. S3.

A total of 144 zircon grains from seven samples were analyzed from the Yusufeli intrusive complex, of which 67 yielded concordant U–Pb dates. A total of 316 zircon grains from 14 samples were analyzed from the Camlikaya intrusive complex, of which 67 yielded concordant U–Pb dates. For both intrusive complexes, zircon grains display euhedral–subhedral tabular habits with varying grains length (40–400 μm) and aspect ratios (1:1–5:1) (Fig. 4). Most zircons exhibit clear oscillatory zoning, with rare homogeneous grains crystallizing in the most mafic samples; that is, hornblende gabbro and (gabbro-) diorite (Fig. 4). The above morphological characteristics, together with high Th/U ratios (0·3–4·9) (Table 2), indicate that these analyzed zircons are magmatic in origin (Kirkland *et al.*, 2015).

In the Yusufeli intrusive complex, ages obtained from two hornblende gabbro intrusions yield overlapping weighted mean ages of 176·8 ± 2·0 Ma (MSWD = 0·4) and 175·4 ± 0·7 Ma (MSWD = 0·5). Of two diorite intrusions analyzed, one yields a weighted mean age of 176·0 ± 1·0 Ma (MSWD = 0·7), whereas another falls within a range of 185·0–176·6 Ma with a weighted mean age of 178·8 ± 2·4 Ma (MSWD = 2·6). Two monzogranite intrusions have the same age within error: 176·3 ± 1·0 Ma (MSWD = 0·4) and 176·5 ± 1·0 Ma (MSWD = 1·0). A single rhyolitic dyke gives a weighted mean age of 170·1 ± 1·6 Ma (MSWD = 1·9). In the Yusufeli intrusive complex, 129 zircons from seven samples yield positive $\varepsilon_{Hf}(t)$ values ranging from +8·1 to +15·8, and the weighted mean $\varepsilon_{Hf}(t)$ values of each sample are tightly constrained between +10·6 ± 1·1 and +13·0 ± 1·3 (Fig. 6).

In the northern part of the Camlikaya intrusive complex, the dated zircons from a gabbrodioritic MME show a large range of ages (155·0–142·4 Ma) with a weighted mean age of 147·2 ± 1·4 Ma (MSWD = 7·7). This is similar to the age range of 156·3–144·8 Ma obtained from a gabbrodiorite intrusion, whose weighted mean age is 150·3 ± 1·0 Ma (MSWD = 4·9). In contrast, a second gabbrodiorite intrusion and a single dioritic dyke yield weighted mean ages of 148·2 ± 0·6 Ma (MSWD = 1·2) and 150·3 ± 1·4 Ma (MSWD = 0·03), respectively. From north to south, four tonalite, four granodiorite, and two monzogranite intrusions exhibit similar ages, constrained between 150·6 ± 1·0 Ma (MSWD = 0·05) and 146·9 ± 1·6 Ma (MSWD = 1·4). In the Camlikaya intrusive complex, 217 zircons from 12 samples display positive $\varepsilon_{Hf}(t)$ values ranging from +4·1 to +12·2 (Fig. 6). The weighted mean $\varepsilon_{Hf}(t)$ values of each sample are similar, varying from +6·1 ± 0·8 to +9·3 ± 1·0, and are less positive than those of the Yusufeli intrusive complex (Fig. 6).

Sample 16TK33-4, from the Yusufeli intrusive complex, and samples 16TK48-2 and 16TK53-2, from the Camlikaya intrusive complex, display a wide range in zircon $^{206}Pb/^{238}U$ ages. Relatively younger zircon $^{206}Pb/^{238}U$ ages may reflect Pb loss. The zircons with relatively older zircon $^{206}Pb/^{238}U$ ages are interpreted as xenocrysts probably assimilated from the pre-existing crust during magma ascent (Davidson *et al.*, 2007*a*; Miller *et al.*, 2007). The xenocrystic zircons could have undergone partial or complete resetting of the U–Pb isotope system at the time of incorporation into the hot, ascending magma (Bomparola *et al.*, 2007; Davidson *et al.*, 2007*a*). The dates of each sample are subject to a normal probability density distribution following the method of Vermeesch (2012) (Supplementary Data Fig. S4), and we have no strong evidence to discard any of these grains. Therefore, we calculate weighted mean ages and interpret them as magma crystallization ages, which are synchronous with other surrounding intrusions (Fig. 5).

Whole-rock major and trace elemental data

One of the sampled dioritic dykes (16TK55-2) was observed to have a high loss on ignition (LOI) value of

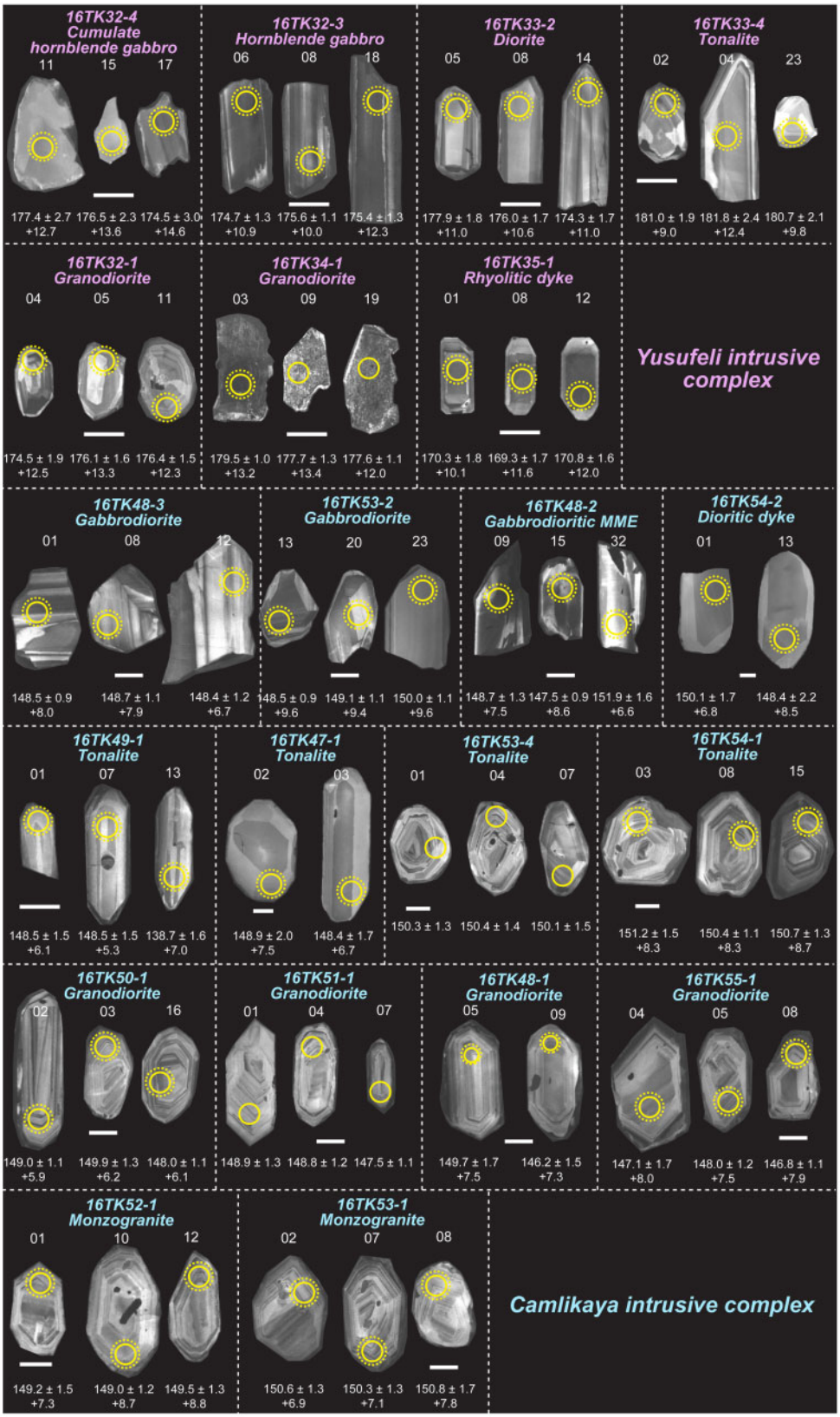

Fig. 4. Cathodoluminescence (CL) images of representative zircons of the Yusufeli and Camlikaya intrusive rocks. Continuous-line and dotted-line circles indicate the locations of U–Pb and Hf isotopic analyses, respectively. The scale-bar length in the CL image represents 50 μm. The numbers on the first and second lines below each zircon represent the weighted mean $^{206}Pb/^{238}U$ ages in Ma and $\varepsilon_{Hf}(t)$ values. (See details of zircon U–Pb and Hf isotopic results in Supplementary Data Electronic Appendix 1 and Supplementary Data Electronic Appendix 2, respectively.)

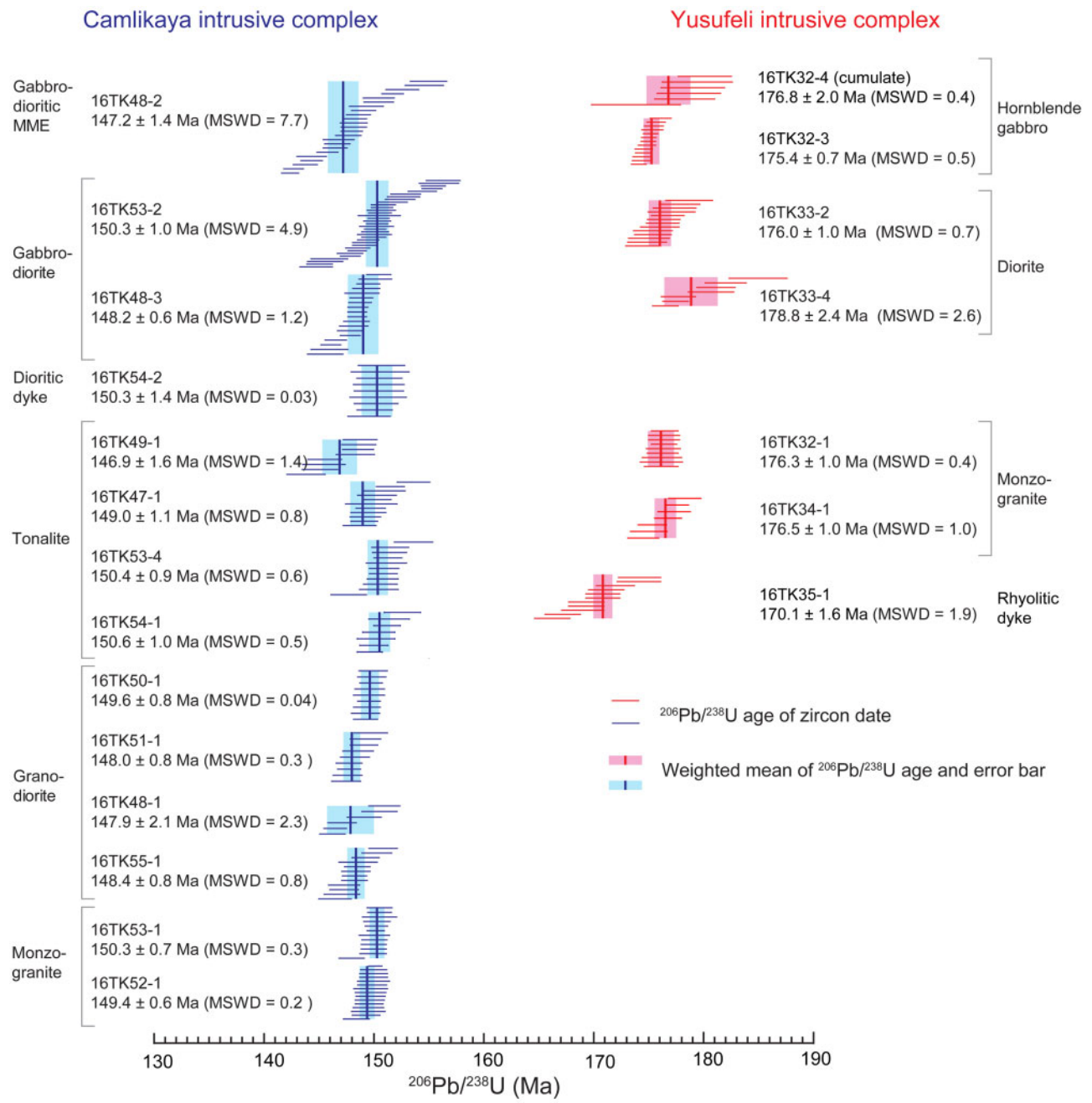

Fig. 5. Geochronology of the Yusufeli and Camlikaya intrusive rocks. The data sources are the same as in Fig. 4. MSWD, mean square weighted deviation.

7·3 wt%. Apart from this sample, the whole-rock compositions of most samples show low LOI values (<3 wt%), indicative of limited alteration. Sample 16TK55-2 is probably significantly altered, and so is excluded from the following discussion. All whole-rock major and trace elemental data are listed in Table 3. Major element compositions are re-normalized to 100 wt% on a volatile-free basis in the following discussion. In this study, we use the geochemical indices of Sr/Nd >50 and/or Eu/Sm >0·46, or SiO_2 <50 wt%, and Si/Al <2·9, as recommended by Jagoutz *et al.* (2011), to identify cumulate rocks. We regard the other, compositionally complementary intrusive rocks as differentiated rocks, which are representative of the LLD. As a result, three hornblende gabbros from the Yusufeli intrusive complex are identified as cumulate rocks, whereas the other samples are classified as differentiated rocks.

As shown in the $Na_2O + K_2O$ vs SiO_2 diagram (Fig 7a) (Middlemost, 1994), the intrusive rocks from the Yusufeli intrusive complex display a compositional range spanning hornblende gabbro, diorite, tonalite, monzogranite, and rhyolitic dyke (SiO_2 = 49·4–75·0 wt%). Most of these rocks are classified in the low-K field, with some plotting in the medium-K field

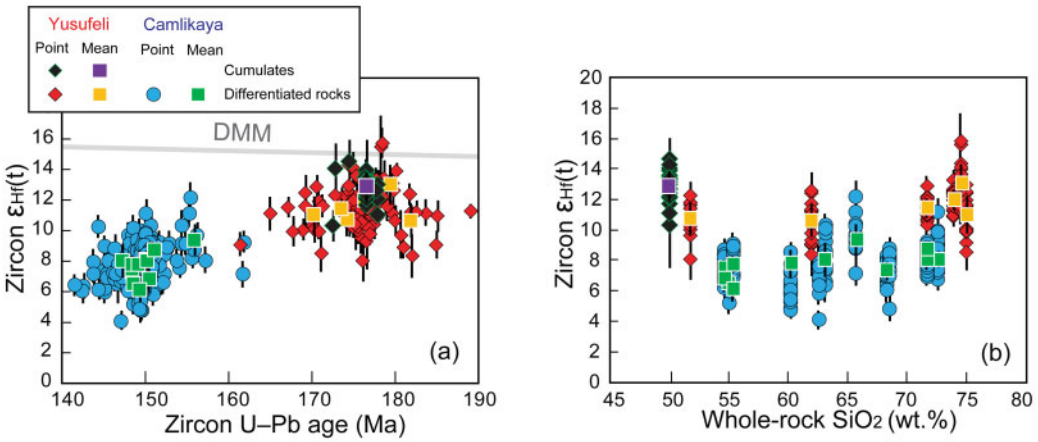

Fig. 6. (a) Zircon $\varepsilon_{Hf}(t)$ vs zircon U–Pb age diagram. (b) Zircon $\varepsilon_{Hf}(t)$ vs whole-rock SiO_2 diagram. The data and errors (2σ) sources of U–Pb and Hf isotopes are the same as in Fig. 4. Mean $\varepsilon_{Hf}(t)$ values of each sample are calculated from $\varepsilon_{Hf}(t)$ values of all zircon grains. The Hf isotopic evolutional trends of the depleted MORB mantle (DMM) are from Workman & Hart (2005).

(Fig. 7b) (Rickwood, 1989). In the AFM (Alkali–FeO_{total}–MgO) diagram (Fig. 7c) and the FeO_{total} vs MgO diagram (Fig. 7d), the whole-rock compositions display an early enrichment in iron, followed by a decrease, which reflects a tholeiitic differentiation path (Irvine & Baragar, 1971). The studied samples vary from metaluminous to slightly peraluminous for the most differentiated rocks, with A/CNK [molar $Al_2O_3/(CaO + Na_2O + K_2O)$] values of 0·5–1·1. On Harker diagrams, Mg# [Mg# = molar $Mg/(Mg + Fe^{2+})$], MgO, and CaO show negative correlations with SiO_2 (Fig. 8a–c). In contrast, Al_2O_3, FeO_{total}, TiO_2, and P_2O_5 increase and subsequently decrease with SiO_2 (Fig. 8d–g). Most of the differentiated rocks exhibit higher Na_2O contents (2·5–7·6 wt%, mean = 5·4 wt%) than those of the Camlikaya intrusive complex at a given SiO_2 (Fig. 8h).

The Camlikaya intrusive complex is composed of gabbrodiorite, diorite, to monzogranite (SiO_2 = 54·6–72·6 wt%) (Fig. 7a). No cumulate rocks are identified. All the differentiated rocks are characterized by higher K_2O contents (0·7–3·9 wt%) than those of the Yusufeli intrusive complex at a given SiO_2. Most of the rocks plot in the medium-K field, and a few analyses straddle the low- to medium-K and medium- to high-K boundaries (Fig. 7b). The differentiated rocks with relatively lower FeO_{total} contents than those of Yusufeli intrusive complex, at a given MgO, follow a typical calc-alkaline trend (Fig. 7c and d) and are characterized as metaluminous (A/CNK = 0·8–1·0). On Harker diagrams, Mg#, MgO, CaO, Al_2O_3, FeO_{total}, TiO_2, and P_2O_5 are all negatively correlated with SiO_2 (Fig. 8a–g).

The cumulate rocks in the Yusufeli intrusive complex have the lowest rare earth element (REE) values of the Yusufeli intrusive complex and are characterized by flat REE patterns, low La/Yb ratios of 0·9–2·5, and positive Eu anomalies [Eu_N/Eu^* = 1·1–1·9, $Eu^* = (Sm_N \times Gd_N)^{0.5}$, where subscript N denotes normalization to the chondritic values of Sun & McDonough, 1989] (Fig. 9a). The primitive mantle-normalized trace element patterns of the cumulate rocks show that they are slightly enriched in large ion lithophile elements (LILE; e.g. Rb, Ba, and Pb) and display negative anomalies for Nb, Ta, and Ti (Fig. 9b). In contrast, the REE contents increase progressively with SiO_2 enrichment in the differentiated rocks, as well as displaying steeper light REE (LREE) and middle REE (MREE) compared with heavy REE (HREE) [La/Yb = 2·1–6·5, $(Dy/Yb)_N$ = 0·8–1·2]. The Eu anomalies (Eu_N/Eu^* = 0·5–1·1) of the differentiated rocks vary from slightly positive to pronounced negative values, as SiO_2 increases (Fig. 9a). The primitive mantle-normalized trace element patterns show that the contents of incompatible elements increase from mafic to felsic compositions, which is associated with decreasing Sr/Y ratios ranging from 24·2 to 0·6. These samples also display negative anomalies in Nb, Ta, and Ti (Fig. 9b).

In the Camlikaya intrusive complex REE pattern for diorite to granodiorite are characterized by a concave-up shape (i.e. spoon-shaped), increasing La/Yb (from 5·4 to 32·0) and Sr/Y (from 18·9 to 87·1) ratios, and decreasing $(Dy/Yb)_N$ (from 1·4 to 1·0) ratios, as a function of SiO_2 (Fig. 9c). The Eu anomalies (Eu_N/Eu^* = 0·7–1·7) are negatively correlated with SiO_2 (Fig. 9c). All the Camlikaya differentiated rocks are enriched in LILE (e.g. Rb, Ba, and Pb) and show negative Nb, Ta, and Ti anomalies (Fig. 9d).

Mineral geochemistry

Summaries of plagioclase, amphibole (pargasite, hornblende, and cummingtonite), and biotite geochemistry are listed in Tables 4–6, respectively. Detailed mineral geochemistry data can be found in Supplementary Data Electronic Appendix 3.

Clinopyroxene

Clinopyroxene observed only in the cumulate hornblende gabbro (sample 16TK33-1) as resorbed crystals in amphibole. Three analyses exhibit homogeneous compositions of diopside ($Wo_{46–47}En_{43–45}Fs_{9–10}$), with

Table 3: Whole-rock major and trace elemental data of the intrusive rocks in the Yusufeli and Camlikaya intrusive complexes

Sample:	16TK32-4	16TK33-1	16TK33-3	16TK32-3	16TK32-2	16TK33-4	16TK33-2	16TK32-1	16TK34-1	16TK35-1
Lithology:	Chgb	Chgb	Chgb	Hgb	Gbdd	To	Diorite	MG	MG	RD
Yusufeli intrusive complex										
Major element (wt%)										
SiO_2	48·79	49·32	49·13	50·93	53·86	60·74	58·62	72·71	73·27	72·48
TiO_2	0·74	0·45	0·97	0·45	1·01	0·37	1·02	0·32	0·22	0·23
Al_2O_3	21·42	15·09	16·83	17·68	17·18	19·46	18·40	14·03	12·87	12·66
Fe_2O_3	5·90	6·77	9·24	6·77	8·34	2·11	6·64	2·80	3·16	2·12
MnO	0·10	0·13	0·16	0·12	0·17	0·04	0·21	0·08	0·05	0·06
MgO	5·00	10·18	8·41	7·76	3·65	0·92	2·19	0·87	0·25	0·58
CaO	11·68	15·53	12·45	11·52	6·76	6·85	6·45	1·20	1·76	1·85
Na_2O	3·31	1·44	2·15	2·43	5·61	7·49	4·44	5·65	6·72	4·36
K_2O	0·61	0·14	0·10	0·69	0·11	0·02	0·56	0·69	0·07	2·30
P_2O_5	0·04	0·02	0·09	0·08	0·23	0·08	0·32	0·08	0·02	0·04
LOI	3·23	1·27	0·85	1·93	2·95	1·92	1·43	1·28	1·11	3·03
Sum	100·82	100·33	100·37	100·35	99·85	100·01	100·28	99·70	99·49	99·70
FeO_{total}	5·31	6·09	8·31	6·09	7·50	1·90	5·98	2·52	2·84	1·91
Trace element ($\mu g\ g^{-1}$)										
Li	6·28	2·30	0·58	2·36	5·35	0·42	2·62	2·15	0·46	5·52
Be	0·30	0·12	0·33	0·31	0·71	0·58	0·65	1·02	1·72	1·30
Sc	19·74	56·53	34·64	31·70	25·84	6·03	24·39	5·46	2·81	4·77
V	118	189	213	150	231	20·3	53·4	21	1·39	4·52
Cr	30·7	174	279	233	6·64	0·64	0·87	1·33	0·44	0·64
Co	27·7	36·4	40·0	32·6	22·9	4·21	5·67	2·68	1·37	1·19
Ni	24·8	94·0	94·5	68·9	12·1	2·53	1·43	1·16	0·66	0·91
Cu	3·57	114	17·9	8·94	58·6	2·79	2·93	4·45	0·82	4·27
Zn	34·3	36·4	52·4	40·0	69·4	18·1	81·0	32·8	24·3	58·9
Ga	15·6	11·1	14·9	12·9	19·2	11·8	18·4	14·8	22·7	18·8
Rb	10·7	2·49	0·62	12·7	1·06	0·57	11·4	12·2	0·97	38·8
Sr	273	130	171	244	141	21·1	262	110	59·9	52·3
Y	6·68	9·42	21·0	10·1	25·5	36·2	27·9	21·8	78·1	55·2
Zr	22·7	12·7	59·8	40·6	92·4	171·6	52·6	146	398	244
Nb	1·07	0·27	1·68	1·64	4·07	4·12	2·03	4·80	22·9	17·5
Sn	0·39	0·30	0·97	0·55	0·85	0·44	0·67	0·65	3·15	3·22
Cs	0·24	0·12	0·02	0·25	0·04	0·08	0·39	0·16	0·03	0·47
Ba	127	48·6	17·4	180	36·0	5·3	107	102	24·3	354
La	1·88	0·85	4·53	5·50	11·5	10·7	6·29	16·0	40·7	28·5
Ce	6·31	2·52	11·0	10·9	25·7	27·9	16·5	28·8	80·6	57·9
Pr	0·69	0·43	1·64	1·39	3·29	3·37	2·15	3·21	9·49	6·85
Nd	3·09	2·56	8·12	6·10	14·7	13·9	10·7	12·4	39·1	28·4
Sm	0·96	1·03	2·53	1·58	3·51	3·85	3·36	2·77	9·45	6·77
Eu	0·66	0·49	0·97	0·58	1·23	0·68	1·42	0·78	1·96	1·10
Gd	1·20	1·51	3·16	1·80	3·85	4·20	4·34	2·87	10·5	7·47
Tb	0·24	0·28	0·55	0·29	0·66	0·83	0·74	0·50	1·94	1·42
Dy	1·35	1·86	3·75	1·88	4·28	5·78	4·93	3·29	13·2	9·44
Ho	0·31	0·38	0·78	0·38	0·89	1·28	1·02	0·71	2·83	2·04
Er	0·75	1·04	2·17	1·06	2·48	3·78	2·72	2·11	8·13	5·78
Tm	0·15	0·15	0·34	0·17	0·42	0·69	0·45	0·36	1·36	0·98
Yb	0·75	0·96	2·06	1·06	2·55	4·97	2·70	2·46	8·64	6·36
Lu	0·15	0·14	0·33	0·17	0·40	0·87	0·45	0·42	1·37	1·00
Hf	0·69	0·47	1·66	1·09	2·34	4·98	1·56	3·72	10·4	6·95
Ta	0·13	0·03	0·11	0·13	0·28	0·24	0·13	0·38	1·27	1·04
Pb	2·39	1·06	0·50	0·92	3·46	1·60	2·96	1·45	1·30	6·58
Th	0·28	0·09	0·62	1·10	2·60	4·81	1·19	5·85	6·70	7·34
U	0·12	0·04	0·14	0·25	1·59	1·16	0·32	1·00	1·46	2·06

(continued)

Table 3: Continued

Sample:	16TK48-3	16TK53-2	16TK53-3	16TK48-2	16TK55-2	16TK54-2	16TK47-1	16TK49-1	16TK53-4	16TK54-1
Lithology:	Gbd	Gbd	Gbd	Gbdm	Dd	Dd	To	To	To	To
Camlikaya intrusive complex										
Major element (wt%)										
SiO_2	53·79	54·19	55·32	53·39	54·98	58·85	62·63	61·89	64·70	63·61
TiO_2	1·15	0·73	0·75	0·81	0·61	0·75	0·68	0·60	0·51	0·58
Al_2O_3	17·98	17·91	18·11	19·02	14·94	16·42	16·42	17·08	17·75	16·50
Fe_2O_3	7·74	6·97	6·18	7·82	5·21	3·57	5·30	5·29	2·17	4·93
MnO	0·11	0·09	0·09	0·15	0·07	0·04	0·09	0·09	0·04	0·03
MgO	4·97	5·03	5·11	3·68	6·32	5·76	2·99	2·76	2·48	2·00
CaO	8·09	8·42	8·28	6·57	5·04	4·95	5·38	5·56	6·47	3·95
Na_2O	3·65	3·17	3·62	3·99	4·31	6·54	3·82	3·83	4·57	4·59
K_2O	0·90	1·29	1·11	1·44	1·03	0·67	1·82	1·69	0·83	2·38
P_2O_5	0·17	0·18	0·19	0·25	0·31	0·24	0·18	0·15	0·18	0·17
LOI	1·62	1·69	1·73	2·19	7·27	2·00	1·12	1·10	0·91	0·96
Sum	100·16	99·67	100·49	99·30	100·08	99·79	100·44	100·04	100·59	99·69
FeO_{total}	6·96	6·27	5·56	7·04	4·69	3·21	4·77	4·76	1·95	4·44
Trace element ($\mu g\ g^{-1}$)										
Li	4·40	8·81	8·34	5·59	26·85	8·53	2·83	8·35	3·23	7·03
Be	0·90	0·89	0·88	1·41	1·48	1·28	1·29	1·33	1·17	1·74
Sc	25·90	18·65	22·50	13·27	9·74	13·87	12·45	10·82	5·79	8·92
V	191	145	145	128	72·3	112	96·4	96·9	80·7	81·2
Cr	3·08	67·0	66·9	2·98	236	180	34·2	8·39	12·1	11·6
Co	24·8	23·8	18·2	18·6	20·1	9·24	13·4	12·3	5·73	8·06
Ni	14·1	44·6	32·0	17·4	188	108	22·5	11·4	15·7	8·31
Cu	22·0	22·8	8·63	15·7	4·03	1·54	16·6	2·85	11·6	7·82
Zn	53·9	33·8	28·0	75·5	119	23·4	50·7	47·3	12·4	16·8
Ga	17·7	16·3	16·3	20·0	18·2	17·2	17·3	17·7	16·9	17·8
Rb	17·1	35·2	28·4	39·4	24·2	21·7	37·5	40·4	13·1	52·7
Sr	504	595	587	557	209	353	481	471	610	414
Y	21·8	12·7	15·3	20·4	15·8	18·7	16·1	14·8	7·01	19·5
Zr	62·7	59·3	89·3	101	136	153	130	83·2	97·5	173
Nb	6·79	7·02	8·08	10·0	8·60	11·7	10·6	7·92	9·28	19·5
Sn	0·83	0·75	1·13	1·41	0·65	0·99	1·31	1·09	0·89	1·19
Cs	0·39	0·60	0·48	0·37	0·51	0·20	0·38	0·88	0·36	0·60
Ba	196	244	175	318	115	85·1	455	330	166	370
La	13·0	15·3	16·2	11·0	27·4	21·3	21·0	37·1	24·5	35·9
Ce	28·4	28·8	31·5	28·7	58·2	43·1	41·7	61·8	39·9	60·0
Pr	3·41	3·17	3·52	3·78	6·92	5·14	4·62	6·06	3·63	6·19
Nd	14·3	12·6	13·9	16·9	27·2	20·2	17·2	20·4	11·9	21·6
Sm	3·48	2·63	2·87	3·82	4·90	4·15	3·24	3·40	1·75	3·81
Eu	1·24	0·94	1·00	1·27	1·50	1·15	1·04	0·96	0·89	0·83
Gd	3·87	2·61	2·76	3·76	4·00	3·71	3·01	3·10	1·54	3·56
Tb	0·64	0·41	0·47	0·58	0·55	0·58	0·47	0·45	0·22	0·53
Dy	4·08	2·51	2·77	3·60	2·79	3·38	2·79	2·76	1·26	3·20
Ho	0·81	0·48	0·54	0·71	0·48	0·65	0·55	0·53	0·25	0·65
Er	2·21	1·36	1·50	2·08	1·17	1·76	1·58	1·51	0·73	1·91
Tm	0·32	0·23	0·25	0·31	0·16	0·27	0·23	0·22	0·12	0·33
Yb	2·07	1·24	1·39	2·02	0·83	1·78	1·53	1·44	0·81	2·10
Lu	0·32	0·22	0·23	0·30	0·13	0·29	0·27	0·24	0·13	0·36
Hf	2·05	1·66	2·31	2·57	3·33	3·83	3·28	2·34	2·40	4·55
Ta	0·54	0·51	0·55	0·64	0·46	0·76	0·72	0·78	0·63	1·77
Pb	5·10	3·41	2·27	7·04	3·81	1·61	6·62	5·59	3·05	4·93
Th	5·07	4·04	3·55	3·16	5·80	7·34	4·45	13·7	7·13	16·82
U	1·58	1·34	1·05	1·15	1·62	2·57	1·62	1·85	1·61	3·58

(continued)

Table 3: Continued

Sample:	16TK48-1	16TK50-1	16TK51-1	16TK55-1	16TK52-1	16TK53-1
Lithology:	Gd	Gd	Gd	Gd	MG	MG
Camlikaya intrusive complex						
Major element (wt%)						
SiO_2	67·63	64·80	67·82	67·66	71·06	71·15
TiO_2	0·44	0·53	0·46	0·46	0·26	0·30
Al_2O_3	15·27	16·12	15·25	15·19	14·15	14·51
Fe_2O_3	3·63	4·48	3·91	3·79	1·69	2·63
MnO	0·07	0·05	0·07	0·04	0·01	0·01
MgO	1·74	2·10	1·93	1·70	0·68	1·05
CaO	3·75	4·27	3·55	3·16	2·76	2·26
Na_2O	3·50	3·87	3·70	4·02	4·21	3·53
K_2O	2·97	2·29	2·65	2·61	3·04	3·83
P_2O_5	0·12	0·15	0·13	0·14	0·07	0·08
LOI	0·95	0·88	1·14	1·31	2·23	0·72
Sum	100·06	99·54	100·61	100·07	100·15	100·08
FeO_{total}	3·27	4·03	3·52	3·41	1·52	2·36
Trace element ($\mu g\ g^{-1}$)						
Li	3·19	7·14	8·35	5·65	4·18	5·24
Be	1·31	1·49	1·46	1·54	1·57	1·18
Sc	7·22	8·02	7·43	6·51	3·34	4·66
V	58·5	73·1	61·3	67·4	28·1	36·4
Cr	10·8	11·0	11·8	7·13	3·69	4·64
Co	7·57	9·91	8·61	7·55	2·57	5·80
Ni	9·49	11·3	10·1	5·92	3·57	4·04
Cu	5·71	4·55	1·46	2·71	0·91	33·9
Zn	35·2	24·7	30·5	17·1	6·33	9·69
Ga	15·1	16·9	15·5	15·7	13·5	13·5
Rb	49·6	54·2	59·7	51·6	49·4	55·4
Sr	350	456	356	389	262	311
Y	12·5	12·9	12·6	11·5	8·81	8·58
Zr	112	114	118	149	108	124
Nb	11·1	10·6	11·6	11·9	11·7	9·83
Sn	1·03	1·15	1·03	0·93	0·60	0·43
Cs	0·34	0·69	0·44	0·72	0·46	0·53
Ba	611	479	485	501	500	850
La	31·3	19·8	45·8	23·4	22·1	11·5
Ce	53·2	37·0	73·8	42·3	35·5	20·7
Pr	5·09	4·08	6·87	4·25	3·34	2·09
Nd	16·7	15·3	21·4	14·8	10·6	7·62
Sm	2·80	2·94	3·24	2·63	1·53	1·46
Eu	0·75	0·83	0·74	0·81	0·50	0·53
Gd	2·33	2·67	2·45	2·30	1·51	1·46
Tb	0·39	0·41	0·37	0·37	0·24	0·23
Dy	2·33	2·43	2·25	2·20	1·45	1·50
Ho	0·46	0·48	0·44	0·44	0·30	0·30
Er	1·27	1·40	1·33	1·24	0·93	0·92
Tm	0·22	0·22	0·22	0·24	0·16	0·16
Yb	1·50	1·51	1·43	1·35	0·97	0·99
Lu	0·25	0·24	0·25	0·26	0·20	0·18
Hf	3·12	3·00	3·19	3·83	3·06	3·14
Ta	1·08	0·81	1·00	0·99	1·15	0·73
Pb	8·23	7·44	6·62	4·76	4·48	4·98
Th	15·8	7·30	15·54	13·08	11·6	7·58
U	3·13	2·14	3·44	2·95	2·03	1·71

$FeO_{total} = Fe_2O_3 \times 0{\cdot}8998$. Chgb, cumulate hornblende gabbro; Dd, dioritic dyke; Gbd, gabbrodiorite; Gbdd, gabbrodioritic dyke; Gbdm, gabbrodioritic MME; Gd, granodiorite; Hgb, hornblende gabbro; LOI, loss on ignition; MG, monzogranite; Rd, rhyolitic dyke.

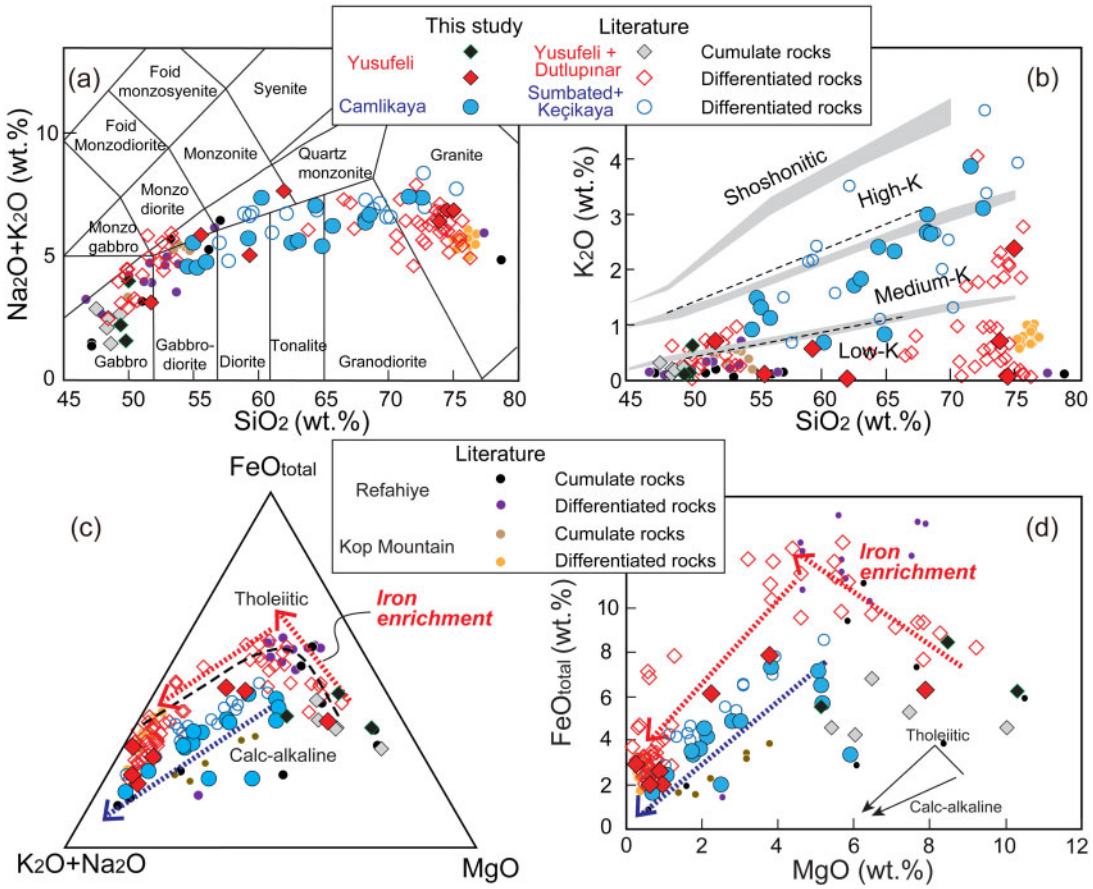

Fig. 7. Chemical classification and nomenclature diagrams for the Yusufeli and Camlikaya intrusive rocks. (a) $Na_2O + K_2O$ vs SiO_2 diagram for classification (Middlemost, 1994). (b) K_2O vs SiO_2 diagram (Rickwood, 1989). (c) AFM diagram (Irvine & Baragar, 1971). All Fe_2O_3 is considered as FeO_{total}. (d) FeO_{total} vs MgO diagram. (See details of whole-rock geochemistry data in Table 3.) The literature data for the Early–Middle Jurassic and Late Jurassic intrusive rocks in the Yusufeli region are from Dokuz *et al.* (2010) and Eyuboglu *et al.* (2016), respectively. The literature data for the Early–Middle Jurassic intrusive rocks in Refahiye and Kop Mountain are from Topuz *et al.* (2013), Uysal *et al.* (2015) and Eyuboglu *et al.* (2016).

Mg# (all Fe^{2+}) values of 81–83, TiO_2 contents of 0·1–0·3 wt%, and Al_2O_3 contents of 0·7–1·1 wt%.

Plagioclase

In the Yusufeli intrusive complex, the anorthite content (An) in plagioclase varies from bytownit (An_{89}) to oligoclase (An_{27}) with normal zoning (Fig. 10a). In cumulate hornblende gabbro, plagioclase crystals grade from bytownite cores (An_{79}) to andesine rims (An_{41}) (Fig. 10a). Plagioclase crystals in one diorite intrusion vary from bytownite cores (An_{72}) to oligoclase rims (An_{27}) (Fig. 10a). Patchy textures (Humphreys *et al.*, 2006) can also be observed in some plagioclase crystals and are characterized by an irregular, resorbed bytownite core ($An_{87–89}$) overgrown by labradorite–andesine ($An_{56–31}$) (Fig. 3f).

In the Camlikaya intrusive complex, the compositions of plagioclase crystals from one gabbrodioritic MME range from labradorite cores (An_{57}) to oligoclase rims (An_{28}) with normal zoning (Fig. 10a). From core to rim, plagioclase crystals from the tonalite and granodiorite intrusions display decreasing An contents, varying from An_{41} to An_{29} and from An_{42} to An_{19}, respectively (Fig. 10a).

Amphibole

Amphibole from the Yusufeli intrusive complex has variable compositions, including pargasite, hornblende, cummingtonite, and actinolite, according to the classification scheme of Leake *et al.* (1997) (Fig. 10b). The pargasite and hornblende are of primary origin. The cummingtonite and actinolite grains are of secondary origin, and thus they are not incorporated in petrogenesis discussion. In cumulate hornblende gabbros, pargasite grains are characterized by Si of 6·26–6·27 a.p.f.u, Mg# of 74, Ti of 0·27–0·33 a.p.f.u, and Al^{IV} of 1·73–1·74 a.p.f.u (Fig. 10b and c). Hornblende crystals have Si of 6·90–7·36 a.p.f.u, Mg# of 73–80, Ti of 0·03–0·08 a.p.f.u, and Al^{IV} of 0·64–1·10 a.p.f.u (Fig. 10b and c). In one diorite intrusion, hornblende crystals are present with Si of 6·93–7·08 a.p.f.u, Mg# of 66–70, Ti of 0·09–0·13 a.p.f.u, and Al^{IV} of 0·92–1·07 a.p.f.u (Fig. 10b and c).

Amphibole found in gabbrodioritic MMEs, and tonalite and granodiorite intrusions from the Camlikaya

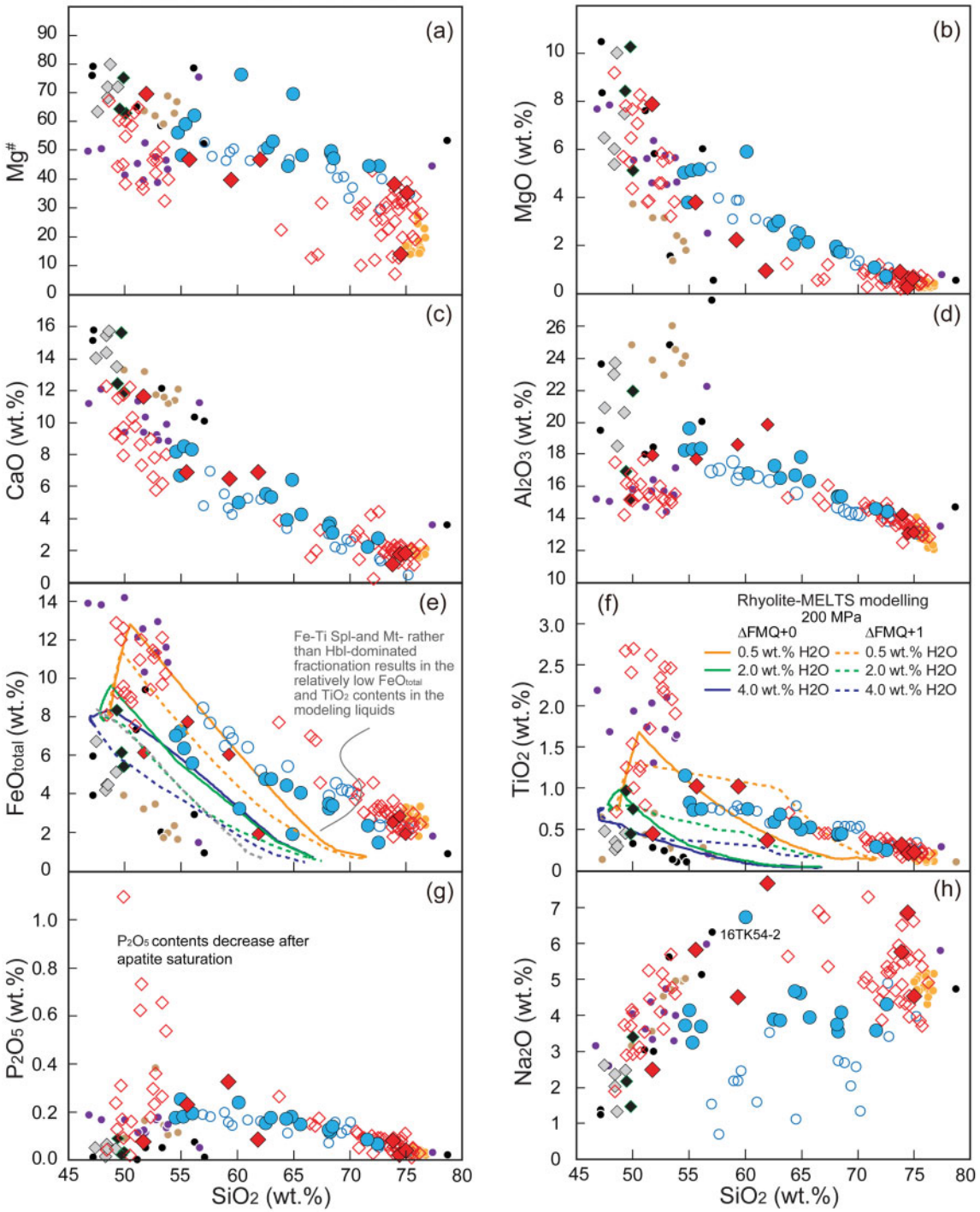

Fig. 8. Harker variation diagrams selected major elements of the Yusufeli and Camlikaya intrusive rocks. All the data resources are the same as in Fig. 7. The Rhyolite-MELTS (Gualda *et al.*, 2012; Ghiorso & Gualda, 2015) modeling of LLDs for fractional crystallization illustrates the effects of initial H_2O content, pressure, and oxygen fugacity buffers on magma differentiation. Hbl, hornblende; Mt, magnetite; Spl, spinel. (See text for detailed descriptions.)

intrusive complex includes hornblende and actinolite (Fig. 10b). For the hornblende crystals, the Mg# values (65–82) are negatively correlated with Ti content (0·04–0·18 a.p.f.u) (Fig. 10c), and they display a similar range of Si of 6·73–7·44 a.p.f.u and Al^{IV} of 0·56–1·27 a.p.f.u across all intrusion types.

Biotite

Analyses of biotite ($n = 18$) crystallized in tonalite and granodiorite intrusions in the Camlikaya intrusive complex range from annite to eastonite–siderophyllite in composition, with Mg# values of 53–58 to 63–64, as well as Al^{IV} of 2·36–2·45 to 2·55–2·56 a.p.f.u (Fig. 10d).

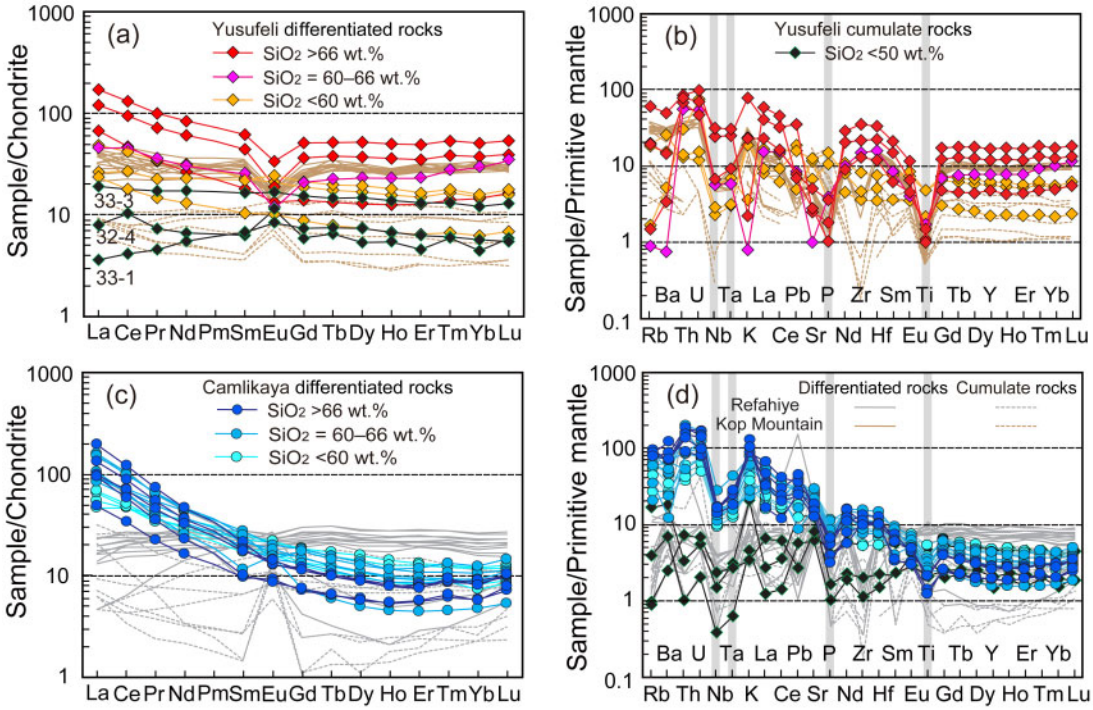

Fig. 9. Chondrite-normalized REE and primitive-mantle-normalized trace element patterns of the Yusufeli and Camlikaya intrusive rocks. Data for normalization are from Sun & McDonough (1989). All the data resources are the same as in Fig. 7.

Although based on only three analyses, the Yusufeli biotites of one diorite intrusion are classified as siderophyllite characterized by lower Mg# values of 51 and higher Al^{IV} of 2·77–2·88 a.p.f.u compared with those of Camlikaya (Fig. 10d).

Geothermobarometry

Pressure

Following the calibration of Mutch *et al.* (2016), we calculate magma emplacement pressure of the Yusufeli and Camlikaya intrusive complexes based on the Al-in-magmatic amphibole (pargasite and hornblende) composition of amphibole rims that are in contact with plagioclase, together with the appropriate mineral assemblage of amphibole + biotite + plagioclase + K-feldspar + quartz + magnetite + ilmenite/titanite + apatite. The results are shown in Table 7. Errors on pressure include the propagation of analytical uncertainties (one standard deviation, 1σ) from the sample analyses and the method of Mutch *et al.* (2016) corresponding to ±16 %.

In the Yusufeli intrusive complex, only one diorite (sample 16TK33-2) meets the criteria of the eight-mineral assemblage buffer and yields a pressure of 210 ± 35 MPa (Table 7). As this diorite intruded into the cumulate hornblende gabbros, we infer that these cumulate rocks formed at a minimum pressure of 210 MPa. In the Camlikaya intrusive complex, all the investigated rocks display the appropriate mineral assemblage. Pressure estimates from a gabbrodioritic MME (sample 16TK48-2), two tonalites (samples 16TK47-1 and 16TK53-4), and two granodiorites (samples 16TK48-1 and 16TK50-1) indicate emplacement at upper crustal conditions of 228 ± 40 MPa, from 137 ± 27 to 257 ± 44 MPa, and from 161 ± 36 to 185 ± 34 MPa, respectively (Table 7). Overall, the two intrusive complexes were emplaced in the upper crust between ∼150 and ∼250 MPa (∼5–8 km).

Temperature

The temperatures magmatic amphibole (pargasite and hornblende) crystallization in the Yusufeli and Camlikaya intrusive complexes are calculated using the amphibole–plagioclase geothermometer formulated by Holland & Blundy (1994) and the amphibole-only geothermometer proposed by Putirka (2016). Following the criteria of Holland & Blundy (1994), we analyzed amphibole–plagioclase pairs close to mineral rim contacts. Analyses of core and rim compositions of amphibole grains are used separately to calculate a temperature using the amphibole-only geothermometer of Putirka (2016). Errors on temperature include the propagation of one standard deviation (1σ) of our sample measurements, and the respective uncertainties associated with the methods of Holland & Blundy [1994, equation (B)] and Putirka (2016), which correspond to ±40 °C (1σ) and ±30 °C (1SE, standard error), respectively. The results are shown in Table 7.

In the Yusufeli intrusive complex, as outlined above, the minimum pressure of the cumulate hornblende gabbros (samples 16TK33-1 and 16TK33-3) is ∼210 MPa. Thus we use 210 MPa to calculate their

Table 4: Average mineral geochemistry of plagioclase from the intrusive rocks in the Yusufeli and Camlikaya intrusive complexes

Sample	Plagioclase of the Yusufeli intrusive complex																			
	Cumulate hornblende gabbro								Diorite								Plagioclase of the Camlikaya intrusive complex			
																	Gabbrodioritic MME			
	16TK33-1				16TK33-3				16TK33-2								16TK48-2			
	core		rim		core		rim		core		rim		high-Ca core		high-Ca rim		core		rim	
Mean of:	$n = 1$*	1σ	$n = 5$	1σ	$n = 6$	1σ	$n = 9$	1σ	$n = 8$	1σ	$n = 17$	1σ	$n = 1$*	1σ	$n = 2$	1σ	$n = 4$	1σ	$n = 12$	1σ
SiO_2 (wt%)	48.16	0·48	49·61	1·88	49·58	0.54	53·78	1·68	53·87	2·21	59·00	1·48	45·74	0·46	45·83	0·01	56·83	2·80	59·05	1·36
Al_2O_3	33·27	48.16	32·06	1·02	32·07	0·57	29.61	1·15	29·11	1·50	25·35	0·99	34·59	0·35	34·58	0·18	26·77	1·89	25·24	0·71
FeO	0·19	0·01	0·19	0·03	0·30	0·20	0·22	0.05	0·14	0·03	0·22	0·05	0·17	0·01	0·18	0·04	0·27	0·05	0·33	0·08
CaO	16·24	0.16	14·83	1·30	15·09	0·59	11·82	1·41	11·44	1.61	7·15	1·20	17·93	0·18	18·01	0·26	8·92	1·96	7·17	0·81
Na_2O	2·41	0.02	3·15	0·73	3·00	0·30	4·94	0.81	5·04	0·96	7.60	0·74	1·40	0·01	1·35	0·16	6·47	1·24	7·70	0·45
K_2O	0·02	0·01	0·02	0·01	0·03	0·01	0·04	0.01	0·12	0·03	0·17	0·03	0·04	0·01	0·03	0·01	0·20	0·12	0·15	0·04
Total	100·28	1.00	99·87	0·52	100·23	0·32	100.41	0·33	99.72	0·33	99·49	0·64	99·86	1·00	99·97	0·32	99·48	0·38	99·65	0·60
An	79	1	72	6	3	3	57	7	55	8	34	6	87	1	88		43	10	34	4
Ab	21	0	28	6	6	3	43	7	44	8	65	6	12	1	12		56	10	65	4

Sample	Plagioclase of the Camlikaya intrusive complex															
	Tonalite								Granodiorite							
	16TK47-1				16TK53-4				16TK50-1				16TK48-1			
	core		rim		core		rim		core		rim		core		rim	
Mean of:	$n = 4$	1σ	$n = 6$	1σ	$n = 4$	1σ	$n = 12$	1σ	$n = 4$	1σ	$n = 12$	1σ	$n = 4$	1σ	$n = 12$	1σ
SiO_2 (wt%)	60·39	0·51	60·55	0·22	57·74	1·19	58·37	0.63	57·71	0·62	62·35	0·40	59·12	1·19	61·62	0·44
Al_2O_3	25·15	0·35	24.86	0·16	26·02	0·98	25·65	0·41	26.44	0·35	23·43	0.35	25·40	0·82	23·65	0·14
FeO	0·13	0·02	0.15	0·04	0·20	0·10	0·25	0·10	0·13	0.03	0·20	0·03	0·15	0.05	0·21	0·05
CaO	6·59	0·27	6.31	0·11	8·20	1·01	7·66	0·42	8·26	0.36	4·81	0·39	7·19	0.97	5·18	0·19
Na_2O	7·87	0·21	8.04	0·06	7·04	0·52	7·40	0·33	6·78	0.34	8·90	0·28	7·58	0.57	8·88	0·14
K_2O	0·17	0·04	0.15	0·03	0·27	0·08	0·25	0·10	0·17	0.04	0·17	0·03	0·19	0.06	0·15	0·04
Total	100·31	0·34	100·06	0·17	99·53	0·51	99·65	0·82	99.48	0·50	99·85	0·22	99·64	0·37	99·70	0·31
An	31	1	30	0	39	5	36	2	40	2	23	2	34	5	24	1
Ab	68	1	9	0	60	5	63	2	59	2	76	2	65	5	75	1

Atomic proportions of plagioclase are calculated based on structural formula with eight oxygens.
*The error on only one analyzed grain is assumed to be 1% of the major oxide concentration, and the minimum value is 0·01 wt%.

Table 5: Average mineral geochemistry of representative amphibole for the intrusive rocks in the Yusufeli and Camlikaya intrusive complexes

Sample	Amphibole of the Yusufeli intrusive complex																			
	Cumulate hornblende gabbro												Diorite							
	16TK33-1 hornblende				16TK33-1 pargasite				16TK33-3 hornblende				16TK33-2 hornblende				16TK33-2 cummingtonite			
	core		rim		core		rim		core		rim		core		rim		core		rim	
Mean of:	$n=1$*	1σ	$n=2$	1σ	$n=1$*	1σ	$n=2$	1σ	$n=6$	1σ	$n=9$	1σ	$n=6$	1σ	$n=17$	1σ	$n=4$	1σ	$n=4$	1σ
SiO_2 (wt%)	48·37	0·48	48·54	0·30	42·91	0·43	43·03	0·05	50.18	1·08	49·14	1·21	48·27	0·35	47·69	0·28	53·25	0·67	52·85	0·72
TiO_2	0·55	0·01	0·56	0·01	3·04	0·03	2·74	0·35	0·47	0·13	0·57	0·12	1·00	0·09	1·02	0.11	0·18	0·09	0·35	0·06
Al_2O_3	7·38	0·07	6·95	0·09	11·37	0·11	11·47	0·29	5·77	0·97	6.96	0·95	5·85	0·24	6.45	0·25	1·49	0·57	2·29	0·35
FeO	10·86	0·11	10·77	0·45	12·24	0·12	12·32	0·11	12·24	0·53	12.53	0·63	16·31	0·31	16.52	0·36	21·99	0·31	21·72	0·42
MnO	0·21	0·00	0·21	0·03	0·18	0·00	0·19	0·01	0·24	0·02	0·23	0.01	0·86	0·05	0·89	0·07	1·93	0·10	1·85	0·09
MgO	16·60	0·17	16·67	0.35	13·43	0·13	13·57	0·00	15·75	0·62	15.05	0·66	14·11	0·28	13.35	0·43	17·40	0·63	16·51	0·32
CaO	11·55	0·12	11·62	0.04	11·53	0·12	11·62	0·20	11·77	0·10	11.83	0·11	9·80	0·16	10.22	0·23	1·95	0·63	2·96	0·64
Na_2O	1·59	0·02	1·49	0.00	2·54	0·03	2·44	0·13	0·82	0·16	0·90	0·17	0·94	0·06	0·98	0.07	0·17	0·06	0·31	0·07
K_2O	0·08	0·00	0·07	0.02	0·32	0·00	0·26	0·04	0·10	0·03	0·13	0.03	0·27	0·03	0·32	0.04	0·03	0·02	0·06	0·02
Cr_2O_3	0·06	0·00	0·06	0.01	0·23	0·00	0·15	0·01	0·22	0·18	0.01	0·02	0·01	0·02	0·00	0.00	0·01	0·01	0·03	0·02
Total	97·31	0·97	97·01	0·19	98·00	0·98	97·95	0·09	97·62	0.20	97·42	0·23	97·51	0·64	97·54	0·30	98·43	0·37	98·96	0·26
Mg# (all Fe^{2+})	79·56	0.80	79·76	1·00	73·64	0·74	73·72	0·17	76.59	1·48	75·33	1·69	68.81	0·78	67·28	1·13	66·81	0·84	65·93	0·56
Si	6·95	0·07	7·00	0·01	6·26	0·06	6·27	0·01	7·19	0·13	7·07	0.14	7·05	0·02	6·99	0·03	7·64	0·07	7·56	0·07
Al^{IV}	1·05	0·01	1·00	0.01	1·74	0·02	1·73	0·01	0·81	0·13	0·93	0·14	0·95	0·02	1·01	0.03	0·25	0·10	0·39	0·06
Al^{VI}	0·20	0·00	0·18	0.02	0·21	0·01	0·24	0·06	0·17	0·04	0·26	0·04	0·06	0·02	0·10	0.02	0·00	0·00	0·00	0·00
Ti	0·06	0·00	0·06	0·00	0·33	0·01	0·30	0·04	0·05	0·01	0·06	01	0·11	0·01	0·11	0·01	0·02	0·01	0·04	0·01

Sample	Amphibole of the Camlikaya intrusive complex																			
	Gabbrodioritic MME				Tonalite								Granodiorite							
	16TK48-2 hornblende				16TK47-1 hornblende				16TK53-4 hornblende				16TK50-1 hornblende				16TK48-1 hornblende			
	core		rim		core		rim		core		rim		core		rim		core		rim	
Mean of:	$n=8$	1σ	$n=12$	1σ	$n=6$	1σ	$n=12$	1σ	$n=8$	1σ	$n=12$	1σ	$n=8$	1σ	$n=12$	1σ	$n=8$	1σ	$n=12$	1σ
SiO_2 (wt%)	47·29	0·38	47·21	0.47	47·41	2·26	46·86	0·91	51·24	0·85	50.93	0·73	48·94	0·67	49·57	0.91	49·00	1·11	48·74	0·62
TiO_2	0·89	0·07	0·90	0·07	1·26	0·35	1·15	0·27	0·72	0·16	0·75	0·15	0.85	0·15	0·74	0·16	0·81	0·13	0·87	0·12
Al_2O_3	6·84	0·26	6·85	0·34	6·61	1·46	7·26	0·55	4·24	0·58	4·64	0·47	5.65	0·48	5·26	0·67	5·72	0·70	5.88	0·37
FeO	15·65	0·30	16·00	0·47	15.29	2·16	15·62	0·79	10·95	0·41	10·84	0.42	14·87	0·38	14·52	0·46	14·38	0.62	14·48	0·33
MnO	0·57	0·03	0·57	0·02	0·48	0.05	0·44	0·03	0·29	0·02	0·23	0·01	0.62	0·04	0·61	0·04	0·66	0·06	0.63	0·03
MgO	13·18	0·19	12·92	0·32	13.22	1·82	12·85	0·52	17·11	0·45	17·09	0.37	14·09	0·40	14·47	0·48	14·15	0.53	13·88	0·36
CaO	11·83	0·13	11·77	0·11	11.54	0·34	11·64	0·24	12·18	0·11	12·18	0.11	11·55	0·17	11·67	0·17	11·65	0.30	11·73	0·18
Na_2O	0·85	0·10	0·80	0·08	1·14	0·33	1·02	0·20	0·49	0·08	0·54	0·13	0.90	0·14	0·82	0·16	0·89	0·21	0·89	0·15
K_2O	0·42	0·09	0·48	0·07	0·67	0.21	0·72	0·12	0·32	0·07	0·35	0·05	0.40	0·05	0·38	0·04	0·46	0·09	0.48	0·06
Cr_2O_3	0·01	0·01	0·02	0·01	0·01	0·01	0·01	0·01	0·03	0·02	0·03	0·02	0.00	0·00	0·00	0·01	0·03	0·02	0.03	0·02
Total	97·58	0·13	97·55	0·37	97·84	0·46	97·74	0·40	97·66	0·17	97·65	0.33	98·00	0·20	98·14	0·28	97.82	0·28	97·66	0·33
Mg# (all Fe^{2+})	68·19	0·70	67.28	1·16	68·53	5·57	67·68	1·93	80·92	1.00	80·05	0·95	70·68	1·11	71·72	1.32	71·44	1·59	70·93	0·97
Si	6·93	0·05	6·93	0·06	6·94	0.24	6·87	0·11	7·31	0·09	7·27	0·08	7·10	0.08	7·16	0·10	7·11	0·12	7·09	0·06
Al^{IV}	1·07	0·05	1·07	0·06	1·06	0·24	1·13	0·11	0·69	0·09	0·73	0·08	0.90	0·08	0·84	0·10	0·89	0·12	0·91	0·06
Al^{VI}	0·11	0·01	0·11	0·02	0·08	0·03	0·13	0·03	0·02	0·01	0·05	0·01	0.07	0·02	0·06	0·02	0·09	0·02	0·10	0·02
Ti	0·10	0·01	0·10	0·01	0·14	0.04	0·13	0·03	0·08	0·02	0·08	0·02	0·09	0.02	0·08	0·02	0·09	0·01	0·10	0·01

Amphibole stoichiometry an nomenclature were determined using Le *et al.* (1997), and atomic proportions are calculated based on structural formula with 23 oxygens.
*The error on only one analyzed grain is assumed to be 1% of the major oxide concentration, and the minimum value is 0·01 wt%.

Table 6: Average mineral geochemistry of biotite from the intrusive rocks in the Yusufeli and Camlikaya intrusive complexes

Sample	Biotite of the Yusufeli intrusive complex				Biotite of the Camlikaya intrusive complex													
	Cumulate hornblende gabbro				Tonalite						Granodiorite							
	16TK33-1 siderophyllite				16TK47-1 annite				16TK53-4 siderophyllite		16TK50-1 annite				16TK48-1 annite			
	core		rim		core		rim		core		core		rim		core		rim	
Mean of:	$n=2$	1σ	$n=1^*$	1σ	$n=3$	1σ	n = 2	1σ	$n=3$	1σ	$n=3$	1σ	$n=2$	1σ	$n=3$	1σ	$n=2$	1σ
SiO_2(%)	32·63	0·48	33·93	0.34	36·90	0·14	37·05	0·68	35·17	0·09	37·16	0·23	37.48	0·23	36·86	0·25	36·80	0·35
TiO_2	3·28	0·47	3·25	0·03	3·34	0.19	3·26	0·34	2·77	0·12	3·55	0·23	3·36	0·14	3.74	0·23	3·50	0·22
Al_2O_3	14·97	0.03	14·73	0·15	14.86	0·32	15·12	0·45	15·21	0·10	14·32	0·17	14·45	0.02	14·50	0·06	14·46	0·06
FeO	22.7	0·34	21·79	0·22	18.90	0·02	18·69	0·14	16·26	0·13	18·53	0·27	18·33	0.39	18·07	0·19	17·80	0·11
MnO	0.39	0·02	0·38	0·01	0·29	0.01	0·29	0·02	0·09	0·01	0·06	0·01	0·07	0·01	0·41	0.01	0·40	0·01
MgO	13·27	0·08	12·72	0·13	12.02	0·06	12·00	0·27	15·72	0·10	13·24	0·25	13·40	0.14	12·92	0·28	13·28	0·37
CaO	0.89	0·28	0·57	0·01	0·02	0.02	0·01	0·01	0·50	0·18	0·02	0·03	0·01	0·01	0·01	0·01	0·01	0·01
Na_2O	0·12	0·01	0·23	0·01	0·16	0.05	0·10	0·04	0·12	0·01	0·12	0·03	0·08	0.01	0.10	0·04	0·08	0·02
K_2O	2·92	0.47	4·30	0·04	9·19	0.02	9·18	0·01	4·59	0·19	8·78	0·27	8·90	0·33	8·87	0.16	8·97	0·13
Cr_2O_3	0·03	0.04	0·02	0·01	0·09	0·04	0·04	0·01	0·01	0·02	0·06	0·02	0·04	0·01	—	—	0·01	0·01
Total	91·25	0·20	92·02	0·92	96.12	0·42	96·15	0·55	90·72	0·27	96·14	0·16	96·40	0.45	95·73	0·42	95·56	0·12
Mg#	1·26	0·23	51·24	0·51	53.37	0·14	53·61	0·37	63·50	0·07	56·25	0·54	56·83	0.78	56·28	0·61	57·30	0·54
Al^{IV}	2.82	0·08	2·66	0·03	2·41	0.01	2·40	0·06	2·55	0·01	2·40	0·02	2·38	0·01	2.42	0·02	2·43	0·04

Biotite stoichiometry and nomenclature were determined using Deer *et al.* (1992), and atomic proportions of biotite are calculated based on structural formula with 22 oxygens.
*The error on only one analyzed grain is assumed to be 1 % of the major oxide concentration, and the minimum value is 0·01 wt%.

minimum temperatures following the method of Holland & Blundy (1994). The pargasite–plagioclase pairs and hornblende–plagioclase pairs in sample 16TK33-1 yield similar rim temperatures of 948 ± 43 and 927 ± 40 °C, which are consistent with the amphibole-only geothermometer results for pargasite rim and core temperatures of 941 ± 31 and 951 ± 30 °C. However, these temperatures are higher than the hornblende rim and core temperatures of 803 ± 30 and 811 ± 30 °C, respectively, given from the amphibole-only geothermometer. This difference may reflect disequilibrium between hornblende and plagioclase. An anorthite content of $An_{32–40}$ would be required in the calculation of the Holland & Blundy (1994) geothermometer to yield consistent temperatures between the two geothermometers. Such a low An content is not recorded in plagioclase, and it may indicate that hornblende probably crystallized late with respect to plagioclase. The hornblende–plagioclase pairs in sample 16TK33-3 yield a rim temperature of 754 ± 55 °C, which is consistent with temperatures of 760 ± 35 and 744 ± 31 °C calculated by the amphibole-only geothermometer for the hornblende rim and core. Sample 16TK33-2 (diorite) also displays similar rim (738 ± 41 °C by hornblende–plagioclase pair and 741 ± 31 °C by amphibole-only geothermometer) and core (733 ± 30 °C by amphibole-only geothermometer) temperatures.

In the Camlikaya intrusive complex, hornblende–plagioclase pairs from the gabbrodioritic MME (sample 16TK48-2), tonalites (samples 16TK47-1 and 16TK53-4), and granodiorites (samples 16TK48-1 and 16TK50-1) yield rim temperatures of 721 ± 48 °C, from 673 ± 44 to 717 ± 47 °C, and from 658 ± 47 to 670 ± 45 °C, respectively. The crystallization temperatures using the amphibole-only geothermometer for both of the hornblende rims and cores in the gabbrodioritic MME (from 747 ± 31 to 751 ± 31 °C), tonalites (from 737 ± 31 to 771 ± 31 °C), and granodiorites (729 ± 34 to 742 ± 31 °C) overlap within error.

DISCUSSION

Evidence for juvenile Jurassic magmatism in the Eastern Pontides

In the Yusufeli and Camlikaya intrusive complexes, our new zircon U–Pb dating highlights two main magmatic events at 179–170 Ma and 151–147 Ma for each intrusive complex, respectively (Fig. 5). The main body of nested intrusions in the Yusufeli intrusive complex yields a duration of ~4 Myr up to 9 Myr if we include the late emplacement of rhyolitic dykes. The Camlikaya intrusive complex is characterized by a duration of ~4 Myr. These results are in agreement with previous regional studies that reported a similar range of zircon U–Pb and hornblende ^{40}Ar–^{39}Ar ages of 185–178 Ma, 188 ± 4 Ma, and 153 ± 3 Ma for the Yusufeli intrusive complex, the Dutlupınar intrusion, and the Sumbated intrusion (Fig. 1c) (Dokuz *et al.*, 2010; Eyuboglu *et al.*, 2016), respectively. However, the results are older than the hornblende ^{40}K–^{39}Ar age of 139 ± 2 Ma for the Camlikaya intrusive complex (Boztuğ & Harlavan, 2008).

In situ zircon $\varepsilon_{Hf}(t)$ isotope values are positive and range from +8·1 to +15·8 (mean = +11·7 ± 2·8, 2σ) for the Yusufeli intrusive complex, and from +4·1 to +12·2 (mean = +7·8 ± 2·4, 2σ) for the Camlikaya intrusive

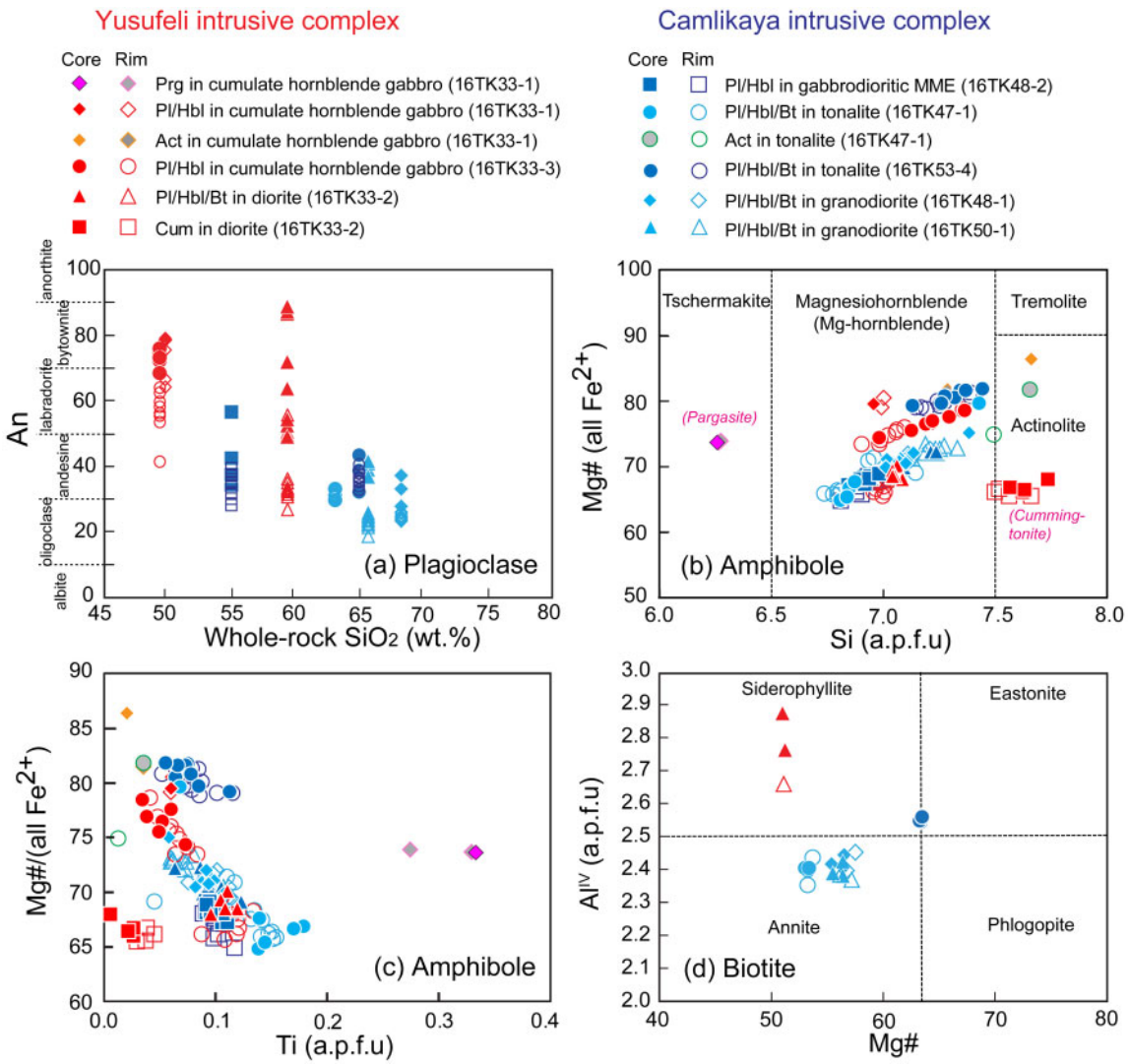

Fig. 10. Mineral compositions of representative plagioclase, amphibole, and biotite from the Yusufeli and Camlikaya intrusive rocks. (a) An vs whole-rock SiO_2 diagram. (b) Classification of amphibole according to the nomenclature of Leake *et al.* (1997). (c) Mg# (all Fe^{2+}) vs Ti diagram. (d) Biotite classification scheme after Deer *et al.* (1992). (See detailed plagioclase, amphibole, and biotite compositions in Supplementary Data Electronic Appendix 3.) Act, actinolite; Bt, biotite; Hbl, hornblende; Pl, plagioclase; Prg, pargasite.

complex (Fig. 6a). This observation is consistent with the $\varepsilon_{Nd}(t)$ values reported in previous studies (Dokuz *et al.*, 2010; Eyuboglu *et al.*, 2016), where the Yusufeli intrusions display higher $\varepsilon_{Nd}(t)$ values (+1·5 to +6·4, mean = +4·5 ± 3·2, 2σ) than those of Camlikaya (+1·9 to +2·5, mean = +2·3 ± 0·4, 2σ). Therefore, these intrusive complexes represent relatively juvenile magmatism derived from a depleted mantle source. However, they do not represent typical pristine melts derived from the depleted mid-ocean ridge basalt (MORB) mantle, characterized by higher ε_{Hf}(180–150 Ma) values of +15·0 to +15·5 and ε_{Nd}(180–150 Ma) values of +8·4 to +8·6 (Workman & Hart, 2005). This indicates the involvement of enriched isotopic components either in the mantle source or by assimilation of overlying continental crust. We do not observe any correlations between SiO_2 and zircon $\varepsilon_{Hf}(t)$ (Fig. 6b). The investigated samples lack inherited zircon cores and display similar Th and U contents of zircons (Table 2). Although the presence of xenocrysts in a few samples (16TK33-4, 16TK48-2, and 16TK53-2) indicates incorporation of the crustal component during magma ascent, the observations listed above support limited crustal assimilation from an old radiogenic basement or metasedimentary components during magma differentiation. Therefore, we suggest that enriched isotopic components (i.e. subduction-related fluids and/or melts derived from subducting lithosphere) were involved in the mantle sources of the Yusufeli and Camlikaya intrusive complexes, and that the two intrusive complexes crystallized from metasomatized, mantle-derived, juvenile melts that have assimilated a limited amount of isotopically enriched crustal components.

Table 7: Pressure and temperature results for the intrusive rocks in the Yusufeli and Camlikaya intrusive complexes

Sample	Rock type	Mineral pairs	*P* (MPa)*	Error	*T* (°C)†	Error	*T* (°C)‡	Error	*T* (°C)§	Error
Yusufeli intrusive complex										
16TK33-1	Cumulate hornblende gabbro	Prg–Pl	210	—	948	43	941	31	951	30
16TK33-1	Cumulate hornblende gabbro	Hbl–Pl	210	—	927	40	803	30	811	30
16TK33-3	Cumulate hornblende gabbro	Hbl–Pl	210	—	754	55	760	35	744	31
16TK33-2	Diorite	Hbl–Pl	210	18	738	41	741	31	733	30
Camlikaya intrusive complex										
16TK48-2	Gabbrodioritic MME	Hbl–Pl	228	40	721	48	747	31	751	31
16TK47-1	Tonalite	Hbl–Pl	257	44	717	47	771	31	752	36
16TK53-4	Tonalite	Hbl–Pl	137	27	673	44	742	32	737	31
16TK48-1	Granodiorite	Hbl–Pl	185	34	670	45	742	31	740	31
16TK50-1	Granodiorite	Hbl–Pl	161	36	658	47	729	34	737	31

*Pressure for amphibole calculated by the method of Mutch *et al.* (2016).
†Temperature for amphibole–plagioclase pair calculated by the method of Holland & Blundy [1994, equation (B)].
‡Temperature for amphibole rim calculated by the method of Putirka [2016, equation (5)].
§Temperature for amphibole core calculated by the method of Putirka [2016, equation (5)]. Errors on pressure include the propagation of analytical uncertainties (1σ) from the sample analyses and also the method of Mutch *et al.* (2016) corresponding to ±16%. Errors on temperature include the propagation of one standard deviation (1σ) of our sample measurements and the respective uncertainties associated with the methods of Holland & Blundy [1994, equation (B)] and Putirka (2016) corresponding to ±40 °C (1σ) and ±30 °C (1SE, standard error), respectively. Hbl, hornblende; Pl, plagioclase; Prg, pargasite. (See text for detailed descriptions.)

Geochemical evolution of the two intrusive complexes

The Yusufeli and Camlikaya intrusive complexes are characterized by similar lithologies, except for the presence of hornblende gabbro and gabbro in the Yusufeli intrusive complex. The whole-rock trace element compositions of the two intrusive complexes are characterized by negative anomalies in Nb, Ta, and Ti, which is the hallmark of subduction-related arc magmatism (Fig. 9b and d) (e.g. Gill, 1981; Hawkesworth *et al.*, 1993; Pearce & Peate, 1995).

The Yusufeli and Camlikaya differentiated rocks differ in their potassium content, such that the Yusufeli lithologies belong to the low- to medium-K series, whereas the Camlikaya rocks are part of the medium- to high-K series (Fig. 7b). In addition, the Yusufeli differentiated rocks show higher Na_2O contents than those of Camlikaya at a given SiO_2 (Fig. 8h). Based on existing experimental petrology studies, the potassium series is fundamentally controlled by the initial alkali content of the parental magma, and potassium enrichment is ultimately related to the SiO_2 enrichment (e.g. Beard, 1995; Rapp & Watson, 1995; Ratajeski *et al.*, 2005; Sisson *et al.*, 2005; Jagoutz, 2013; Müntener & Ulmer, 2018). Thus, it can be inferred that there was a progressive enrichment in the K_2O content of the magma source from the Early–Middle to Late Jurassic. This change in K_2O content is consistent with the variation of Hf–Nd isotopic compositions of the two intrusive complexes from higher $\varepsilon_{Hf}(t)$ (+8·1 to +15·8) and $\varepsilon_{Nd}(t)$ (+1·5 to +6·4) values to lower $\varepsilon_{Hf}(t)$ (+4·1 to +12·2) and $\varepsilon_{Nd}(t)$ (+1·9 to +2·5) values over time. Both elemental and isotopic data suggest that the younger Camlikaya intrusive complex is derived from a mantle-related source that has been metasomatized by subduction-related fluids and/or melts derived from subducting lithosphere relative to the less-metasomatized mantle source involved in the formation of the older Yusufeli intrusive complex.

Except for K_2O and Na_2O, the other major elements of the Yusufeli and Camlikaya differentiated rocks behave similarly for rocks with $SiO_2 \geq 55$ wt% (Fig. 8a–g). However, the trace element patterns are significantly different for the two intrusive complexes (Fig. 9). The Yusufeli differentiated rocks are characterized by the progressive development of negative Eu anomalies and decreasing Dy/Yb ratios (from 1·8 to 1·2) as SiO_2 content increases. This is indicative of plagioclase, amphibole and/or clinopyroxene fractionation, with no evidence of garnet crystallization, during magma differentiation (Figs 9a and 11a; Macpherson *et al.*, 2006; Davidson *et al.*, 2007*b*; Jagoutz, 2010; Jagoutz *et al.*, 2011, 2013). As SiO_2 increases, the increase in Y content (from 10·1 to 78·1 $\mu g\,g^{-1}$) associated with decreasing Sr/Y ratio (from 24·2 to 0·6) in the Yusufeli differentiated rocks further supports the prominent role of plagioclase and clinopyroxene fractionation with limited amphibole crystallization during magma differentiation (Fig. 11b) (e.g. Moyen *et al.*, 2009). This is also supported by the occurrence of cumulate hornblende gabbros that show the lowest REE contents of the Yusufeli intrusive complex, as well as positive anomalies in Eu, indicating plagioclase (± amphibole ± clinopyroxene) accumulation (Fig. 9a).

In contrast, the Camlikaya differentiated rocks generally lack negative Eu anomalies in their spoon-shaped REE pattern. As SiO_2 increases, their Y contents (from 21·8 to 7·0 $\mu g\,g^{-1}$) decrease whereas Sr/Y ratios (from 18·9 to 87·1) increase (Figs 9c and 11b). Their Dy/Yb ratios (from 2·0 to 1·5) decrease as SiO_2 increases (Fig. 11a). Altogether, this suggests that the fractionating mineral assemblage for the Camlikaya intrusive complex is dominated by amphibole together with subsidiary plagioclase and clinopyroxene, which is consistent with our petrographic observations.

In summary, the differences highlighted between the Yusufeli and Camlikaya intrusive complexes may stem

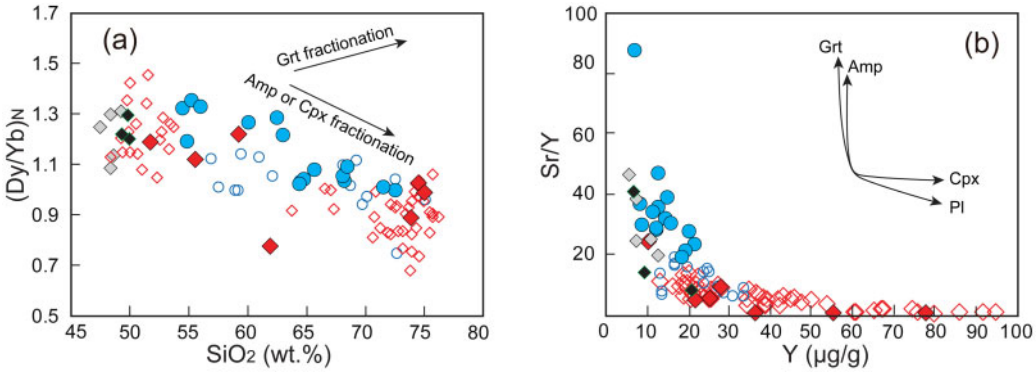

Fig. 11. (a) $(Dy/Yb)_N$ vs. SiO_2 diagram. Dy and Yb for normalization are from Sun & McDonough (1989). (b) Sr/Y vs Y diagram. Arrows indicate the effects of amphibole (Amp), clinopyroxene (Cpx), garnet (Grt), and plagioclase (Pl) fractionation for liquid composition. All the data resources are the same as in Fig. 7. (See text for detailed descriptions.)

from different magmatic source compositions and differentiation processes characterized by different crystallization sequences, which are further discussed below.

Geochemical modeling of the two intrusive complexes

Following the discussion above, we attempt to quantitatively constrain the fractional crystallization process. Owing to a lack of exposed associated ultramafic–mafic cumulate rocks in the region, it is difficult to constrain the full sequence of crystallization from the lower crust to the upper crust (e.g. Jagoutz, 2010; Dessimoz *et al.*, 2012; Bucholz *et al.*, 2014; Walker *et al.*, 2015). Instead, we model the relative fractional crystallization that occurred in the upper crust using the Rayleigh fractionation equation $C_{liq}/C_i = F^{(D-1)}$ for REE (Fig. 12), where C_{liq} is the content of a given element in the residual liquid, C_i is the initial content of an element i in the starting composition, F is the remaining liquid fraction, and D is the bulk partition coefficient. The starting composition corresponds to the least differentiated sample for each intrusive complex, and we model the fractionation of the major rock-forming silicates observed in thin section (i.e. clinopyroxene, amphibole, and plagioclase) and an accessory mineral (i.e. zircon). The respective mineral partition coefficients used in the modeling and detailed calculations are given in Supplementary Data Electronic Appendix 4.

For the Yusufeli intrusive complex, the starting composition corresponds to the sample YE-89 (microgabbro in the Yusufeli intrusive complex) from Eyuboglu *et al.* (2016), as it is the closest to primitive arc melts (i.e. SiO_2 = 48·4 wt%, MgO = 9·2 wt%, and Mg# = 67) (Kelemen *et al.*, 2014; Schmidt & Jagoutz, 2017). The model can reasonably reproduce the evolution of the REE patterns observed in the Yusufeli differentiated rocks using a mineral assemblage of 52% clinopyroxene, 34% plagioclase, 14% amphibole, and 0·05% zircon, for F ranging from 54 to 6% (Fig. 12a). It should be noted that only one differentiated sample of hornblende gabbro (sample 16TK32-3) is characterized by significantly lower HREE content (Fig. 12a), and this can be modeled by increasing the relative proportion of amphibole (40%) with respect to plagioclase (10%) in the fractionated mineral assemblage at F = 70% (Fig. 12a). As the Camlikaya intrusive complex lacks samples with near-primitive melt compositions, we use the least differentiated sample (sample 16TK48-3, gabbrodiorite in the Camlikaya intrusive complex) as the starting composition, which has SiO_2 = 54·6 wt%, MgO = 5·0 wt%, and Mg# = 56. According to our modeling results, the REE patterns of the Camlikaya differentiated rocks can be reproduced through crystallization of 18% clinopyroxene, 20% plagioclase, 62% amphibole, and 0·05% zircon, for F ranging from 100 to 23% (Fig. 12b).

For each intrusive complex, the REE patterns of the differentiated rocks can be reasonably reproduced through Rayleigh fractionation. The differences in the REE patterns between two intrusive complexes result primarily from low (14%) and high (62%) proportions of crystallized amphibole. We acknowledge that some of the differentiated rock REE patterns are not well reproduced by our model, which probably reflects the limitations of such simple modeling to reproduce complex open magmatic systems. It also should be noted that the constant partition coefficient for each element applied in our Rayleigh fractionation modeling over a wide crystallization range is an oversimplification.

Petrogenesis of the two intrusive complexes

Magmatic processes and emplacement onditions

Based on geothermobarometry, we estimate that the Yusufeli magmas crystallized at a pressure of ~210 MPa (~7 km) and the Camlikaya magmas crystallized at pressures between ~150 (~5 km) and ~250 MPa (~8 km). This indicates that the intrusions were emplaced within the upper crust. Most of the estimated temperatures of the intermediate–felsic intrusions vary from ~660 to ~770 °C with hornblende gabbros characterized by higher crystallization temperatures of ~800 to ~950 °C (Fig. 13a). For each intrusive complex, pressure estimates are consistent with the experiments of Moore &

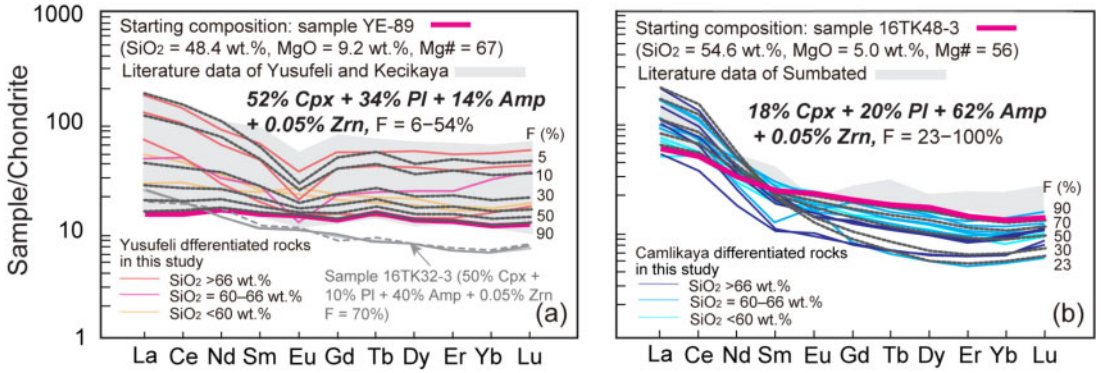

Fig. 12. Chondrite-normalized REE patterns of the modeling results. Data for normalization are from Sun & McDonough (1989). The sample YE-89 from Eyuboglu *et al.* (2016) and sample 16TK48-3 in this study are taken as starting compositions for the Yusufeli and Camlikaya intrusive rocks, respectively. The black and gray dashed lines are the modeling results. The gray shaded area represents the literature data of the intrusive rocks in the Yusufeli region. All the data resources are the same as in Fig. 7. Amp, amphibole; Cpx, clinopyroxene; Pl, plagioclase; Zrn, zircon. (See text for detailed descriptions.)

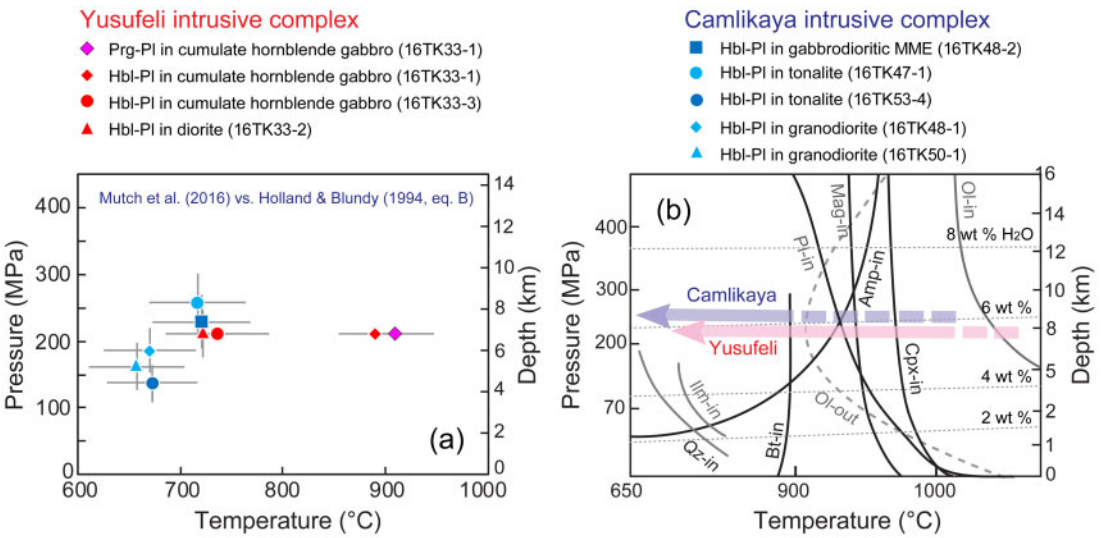

Fig. 13. Pressure vs temperature diagram. The pressure and temperature results in (a) are calculated by the method of Mutch *et al.* (2016) and Holland & Blundy [1994, equation (B)], respectively. The results of pressure–temperature and associated errors are listed in Table 7. Subhorizontal dashed lines in (b) are isopleths of H_2O solubility from Moore & Carmichael (1998). The mineral stability fields are based on the experimental data of Merzbacher & Eggler (1984), Ulmer (1988), Moore & Carmichael (1998), Grove *et al.* (2003) and Rutherford & Devine (2003), and they may vary as a function of temperature, pressure, initial H_2O content, liquid composition, and oxygen fugacity. The blue and pink trends exhibit the inferred isobaric fractional crystallization process for the Camlikaya and Yusufeli magmas, respectively. Amp, amphibole; Bt, biotite; Cpx, clinopyroxene; Hbl, hornblende; Ilm, ilmenite; Mag, magnetite; Ol, olivine; Pl, plagioclase; Prg, pargasite; Qz, quartz. (See text for detailed descriptions.)

Carmichael (1998). The experiments indicate co-crystallization of hornblende and plagioclase at a pressure of ~180–250 MPa (~970–1000 °C) in the H_2O-saturated basaltic andesitic–andesitic liquids [nickel–nickel oxide (NNO) buffer], whereas plagioclase would crystallize prior to hornblende at lower pressures of <180–250 MPa (Fig. 13b). Furthermore, the experimental observations are also consistent with our petrographic observations showing that plagioclase crystallized prior to hornblende in the Yusufeli intrusive complex, whereas plagioclase co-crystallized with hornblende in the Camlikaya intrusive complex (Fig. 3). Our results contrast with the wide range of pressure (90–900 MPa) and temperature (720–1270 °C) reported by Eyuboglu *et al.* (2016) for the Yusufeli intrusive complex. Such a wide range of pressure and temperature over a limited area seems unreasonable and may arise from applying Al-in-hornblende geothermobarometry to rocks without the required mineral assemblages.

The presence of cross-cutting relationships among various types of intrusions illustrates the incremental growth of each magmatic complex through multiple, successive magma pulses (Wiebe & Collins, 1998; Miller *et al.*, 2007; Rezeau *et al.*, 2016, 2018). The widespread occurrence of dykes with variable compositions cross-cutting the main intrusions (Fig. 2g and h), together with the presence of MMEs (Fig. 2i and j), indicates interaction between melts of distinct

compositions as a result of magma recharge (e.g. McNulty *et al.*, 1996; Petford, 1996; Coleman *et al.*, 2004). Therefore, both intrusive complexes represent open magmatic systems. This inference is further supported by the occurrence of resorbed An-rich plagioclase cores overgrown by An-poorer rims (patchy textures; Humphreys *et al.*, 2006) in the Yusufeli diorite (Fig. 3f). Such chemical and mineral textural features indicate episodes of crystallization at different pressures, related to a combination of cooling and decompression for the Yusufeli magmas (Jorgenson, 1971; Panjasawatwong *et al.*, 1995; Humphreys *et al.*, 2006). Plagioclase crystals from the two intrusive complexes are dominantly characterized by a continuous decrease in An content from core to rim, which supports the interpretation that most intrusions crystallized upon cooling.

In summary, we propose that both of the Yusufeli and Camlikaya intrusive complexes represent open magmatic systems crystallized at upper crustal depths of ~5–8 km (~150–250 MPa) upon cooling and/or decompression.

A relative estimate of initial H_2O content in parental magma

Textural observations, trace element ratios, and REE modeling show that the Yusufeli intrusive complex is dominated by plagioclase and clinopyroxene fractionation for comparable differentiated rock compositions, with plagioclase crystallization prior to amphibole. In contrast, the Camlikaya intrusive complex is dominated by plagioclase and amphibole co-crystallization (Figs 11 and 12). This suggests that the relative appearance of plagioclase and amphibole on the respective LLD is different for each intrusive complex. Experiments have demonstrated that the timing of plagioclase crystallization with respect to amphibole is ultimately controlled by the initial H_2O content, whereby relatively high H_2O content, in wet magma, delays the appearance of plagioclase and promotes early crystallization of amphibole and Fe–Ti oxides on the LLD (Fig. 14a) (e.g. Sisson & Grove, 1993; Grove *et al.*, 2003; Villiger *et al.*, 2004, 2006; Nandedkar *et al.*, 2014; Ulmer *et al.*, 2018). This is generally proposed to be the main controlling factor in the generation of tholeiitic versus calc-alkaline magmas, where increased H_2O leads to the depletion of FeO_{total} and TiO_2 contents of calc-alkaline magma during the early stages of magma differentiation (e.g. Sisson & Grove, 1993; Grove *et al.*, 2002; Zimmer *et al.*, 2010; Jagoutz *et al.*, 2011; Müntener & Ulmer, 2018). Volcanic rocks generated in different tectonic settings (e.g. main arc, back-arc, and mid-ocean ridge) show distinct evolution trends in the TiO_2 vs MgO diagram (Fig. 14b), suggesting that different initial H_2O contents have a strong control over the LLD as discussed above (e.g. Ulmer *et al.*, 2018). As shown in Fig. 14b, the dry to damp tholeiitic magmas that compose the global mid-ocean ridges and the Mariana Trough have a significant TiO_2 enrichment whereas wet calc-alkaline magmatism dominates in the Mariana and Cascades main arcs. The Mariana fore-arc basalts are products of the initial stage of subduction, and they display a TiO_2 vs MgO pattern similar to those shown by main arc magmas (Fig. 14b) (Reagan *et al.*, 2010; Ishizuka *et al.*, 2014). As discussed above, the TiO_2 vs MgO diagram is useful in evaluating magma differentiation series and related tectonic settings.

Although most of the major elements display similar trends between the Yusufeli and Camlikaya differentiated rocks, we note that the Yusufeli differentiated rocks exhibit significant enrichment in FeO_{total} and TiO_2 at the early stage of magma differentiation (SiO_2 = ~48–54 wt%, MgO = ~4–9 wt%; Figs 7c, d, 8e, f and 14b). This indicates magma differentiation with a tholeiitic affinity. Similar differentiated rocks from the Camlikaya intrusive complex show systematic lower FeO_{total} and TiO_2 contents in the AFM, FeO_{total} vs MgO, and TiO_2 vs MgO diagrams, compared with the Yusufeli differentiated rocks (Figs 7c, d and 14b). This strongly suggests an early FeO_{total} and TiO_2 depletion indicative of a calc-alkaline affinity.

A kink in P_2O_5 at ~50 wt% SiO_2 is observed for the Yusufeli differentiated rocks and is absent for the Camlikaya differentiated rocks (Fig. 8g). This may relate to a lower H_2O content in magma, as higher H_2O contents in magma can promote apatite crystallization (Lee & Bachmann, 2014). Furthermore, we also observed significantly higher Na_2O contents in the Yusufeli differentiated rocks compared with those of Camlikaya, at a given SiO_2 (Fig. 8h). Based on the studies on the Newberry Volcano lavas from the Cascades and experimental results, Mandler *et al.* (2014) proposed that both dry and wet magmas have Na_2O depletion relative to those of damp magma. This is because dry magma crystallizes abundant Na-rich plagioclases during the early stages of crystallization, and wet magma can promote stable Na-bearing hornblende fractionation, thus resulting in the extraction of Na from the liquids (e.g. Sisson & Grove, 1993; Panjasawatwong *et al.*, 1995). In contrast, damp magmas will crystallize a relatively low Na_2O content plagioclase and will also partly destabilize Na-bearing amphibole (e.g. Sisson & Grove, 1993; Mandler *et al.*, 2014). Considering that the Yusufeli and Camlikaya intrusive complexes are derived from two temporally distinct sources, we cannot rule out the role of variable initial Na_2O content in the respective parental magma.

To test the influence of initial H_2O content on the whole-rock geochemical trends for the two intrusive complexes, we use the thermodynamically calibrated Rhyolite-MELTS program (Gualda *et al.*, 2012; Ghiorso & Gualda, 2015). However, we acknowledge that Rhyolite-MELTS has issues with predicting phase equilibria of hydrous minerals (e.g. amphibole and biotite). This approach has been shown to reasonably reproduce the tholeiitic and calc-alkaline LLDs for volcanic rocks along the Aleutian island arc (Zimmer *et al.*,

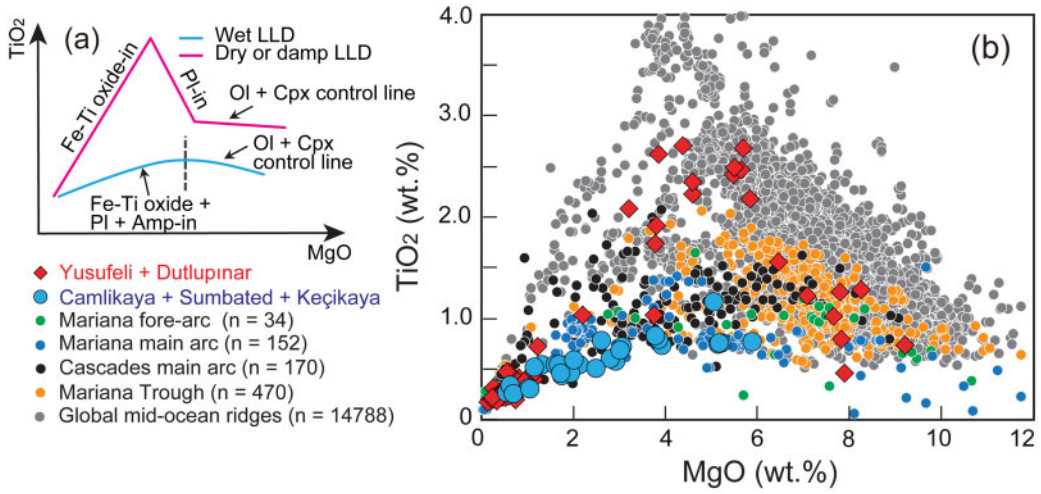

Fig. 14. (a) Schematic illustration showing the effects of magmatic H_2O on the LLD (after Deng *et al.*, 2019). (b) TiO_2 vs MgO diagram. The compiled data of the volcanic rocks in the Mariana fore-arc and main arc are from Stern & Bibee (1984), Bloomer *et al.* (1989), de Moor *et al.* (2005), Wade *et al.* (2005), Kohut *et al.* (2006), Stern *et al.* (2006), Reagan *et al.* (2008, 2010), Marske *et al.* (2011), Woodhead *et al.* (2011), Kelley & Cottrell (2012) and Ikeda *et al.* (2016). The compiled data of volcanic rocks in the Mariana Trough are from Hart *et al.* (1972), Dietrich *et al.* (1978), Fryer *et al.* (1982, 1997), Hawkins & Melchior (1985), Hawkins *et al.* (1990), Lonsdale & Hawkins (1985), Fine & Stolper (1986), Sinton and Fryer (1987), Volpe *et al.* (1987), Bloomer *et al.* (1989), Stern *et al.* (1989, 1990), Gribble *et al.* (1996, 1998), Ikeda *et al.* (1998, 2016), Sano *et al.* (1998), Tamura *et al.* (2011) and Kurzawa *et al.* (2019). The geochemical dataset of global mid-ocean ridge basalts is from Gale *et al.* (2013). The data of volcanic rocks in the Cascades main arc are from du Bray *et al.* (2006). Amp, amphibole; Cpx, clinopyroxene; LLD, liquid line of descent; Ol, olivine; Pl, plagioclase. (See text for detailed descriptions.)

2010), which ultimately demonstrates the role of initial H_2O content in controlling the evolution of FeO_{total}–MgO. Our computations include input parameters based on our study; that is, pressure, temperature, and starting composition corresponding to the sample YE-89.

Calculations were set up for isobaric fractional crystallization scenarios at pressure conditions of 200 and 400 MPa, for initial H_2O content that varies from 0·5 to 4·0 wt% and redox conditions, using the fayalite–magnetite–quartz (FMQ) buffers, of +0, +1, and +2. The detailed modeling results can be found in the Supplementary Data Fig. S5. In this discussion, we focus on FeO_{total} and TiO_2 trends as they represent the most distinctive geochemical characteristics between the two intrusive complexes.

At 200 MPa, the compositional evolution trend of the Yusufeli LLD can be reproduced by fractional crystallization of a parental magma characterized by 0·5–2·0 wt% H_2O at ΔFMQ +0 and +1, whereas the Camlikaya LLD is better reproduced with parental magmas having 2·0–4·0 wt% H_2O at ΔFMQ +1. It is noteworthy that modeling at ΔFMQ +2 at any initial melt H_2O contents prevents FeO_{total} and TiO_2 enrichment necessary to reproduce the LLD observed in Yusufeli (Fig. 8e and f). The upward kinks in FeO_{total} and TiO_2 at ~50 wt% SiO_2 for the modeled LLD with 0·5–2 wt% initial melt H_2O content indicate the onset of Fe–Ti-oxide crystallization. Models with 4 wt% initial melt H_2O content lack such kinks owing to delayed plagioclase crystallization (i.e. it suppresses a significant increase in FeO_{total} and TiO_2 contents prior to the Fe–Ti-oxide crystallization) and promote early crystallization of Fe–Ti-oxide (Fig. 8e and f). The Yusufeli differentiated rocks show higher TiO_2 contents (up to 2·7 wt%) than our modeling results, indicating that the starting composition used in modeling has lower initial TiO_2 content than the magma source (Fig. 8f). It is noteworthy that all the modeled liquids of the two intrusive complexes display lower FeO_{total} and TiO_2 contents at a high SiO_2 content (>~60 wt%) (Fig. 8e and f and Supplementary Data Fig. S5). This stems from the over-suppression of hornblende in our Rhyolite-MELTS modeling system, where hornblende does not appear or appears only at the last stage of magma differentiation (<~800 °C). In contrast, Rhyolite-MELTS forces abundant Fe–Ti spinel (hercynite and ulvöspinel) and magnetite crystallization. The abundant crystallization of spinel and magnetite leads to a rapid depletion of FeO_{total} and TiO_2 during crystallization. If amphibole crystallization was accurately modeled, we would observe a smoother depletion of FeO_{total} and TiO_2 content resulting in a better match with our samples. Despite the mismatch of absolute values of FeO_{total} and TiO_2, our modeling reasonably reproduces the distinctive FeO_{total} and TiO_2 LLDs that differentiate the two intrusive complexes. Such differences between the Yusufeli and Camlikaya LLDs are indicative of the role of the initial melt H_2O content and oxygen fugacity condition in controlling tholeiitic and calc-alkaline differentiation trends, whereas the pressure plays a minor or insignificant role (Fig. 8e and f; Supplementary Data Fig. S5). It is extremely difficult to provide a quantitative estimate of the initial H_2O content for the parental magmas and the oxygen fugacity condition during magma

differentiation of the Yusufeli and Camlikaya intrusive complexes. According to our modeling, we propose that the Yusufeli and Camlikaya parental magmas should be damp and wet at ΔFMQ +0 to +1, respectively.

Geodynamic interpretations

The subduction polarity (south vs north dipping) in the Eastern Pontides during the Jurassic is highly debated. Two geodynamic models have been proposed. Several previous studies have suggested that this arc can be attributed to the northward subduction of the northern branch of the Neotethys oceanic lithosphere (e.g. Adamia *et al.*, 1977; Okay & Şahintürk, 1997; Galoyan *et al.*, 2009; Topuz *et al.*, 2013; Okay *et al.*, 2014; Hässig *et al.*, 2017; Rolland *et al.*, 2020). This interpretation is primarily based on the presence of the Permian–Triassic Karakaya oceanic accretionary complex in the Southern Zone (Tokat and Ağvanis massifs) and the Jurassic–Cretaceous ophiolites (ultramafic–mafic massifs; e.g. Refahiye and Kop Mountain) along the IAE suture zone. These observations suggest that the Southern Zone represents a northward subduction-related fore-arc (e.g. Okay & Şahintürk, 1997; Bektas *et al.*, 2001; Topuz *et al.*, 2013; Rolland *et al.*, 2020).

In contrast, others have argued that the Eastern Pontides arc was associated with the southward subduction of the Paleotethys oceanic lithosphere (e.g. Şengör *et al.*, 1980; Yilmaz *et al.*, 1998; Bektas *et al.*, 2001; Dokuz & Tanyolu, 2006; Dokuz *et al.*, 2010, 2019; Eyuboglu *et al.*, 2016, 2019; Karsli *et al.*, 2017). In the Southern Zone, the Lower–Middle Jurassic strata vary from lacustrine to shallow- and deep-marine facies and display large lateral and vertical variations in both bed thickness and grain size. These features, together with the presence of coeval, regional-scale networks of conjugate normal faults and neptunian dykes, have been considered as strong evidence that the Southern Zone represents a southward subduction-related back-arc basin (e.g. Şengör *et al.*, 1980; Robinson *et al.*, 1995; Bektas *et al.*, 2001; Dokuz & Tanyolu, 2006; Eyuboglu, 2006). Furthermore, the Karakaya complex has been interpreted as an oceanic accretionary prism owing to the identification of blue amphibole-bearing metagabbro exposed in the Tokat massif (Fig. 1b) (e.g. Catlos *et al.*, 2013). However, a recent study has shown that the blue amphibole in the metagabbro is magnesioriebeckite that forms under greenschist-facies conditions (rather than glaucophane, which is a product of blueschist facies) (Eyuboglu *et al.*, 2018). This, together with the absence of other minerals typical of the blueschist facies (e.g. lawsonite and aragonite), led Eyuboglu *et al.* (2018) to argue for the previous idea of Şengör *et al.* (1980), that the formation of the Karakaya complex was related to a back-arc marginal basin rather than a fore-arc basin. In addition, new zircon U–Pb ages of gabbros and diorites that intrude into the ultramafic–mafic massifs (e.g. Erzincan and Kop Mountain) along the IAE yield a broad age spectrum ranging from the Silurian to the Jurassic (Eyuboglu *et al.*, 2016). The ultramafic–mafic massifs should be, at least, older than Silurian, rather than the Jurassic age for the ophiolites assumed by the northward subduction model (Eyuboglu *et al.*, 2016). Therefore, the Northern and Southern Zones of the Eastern Pontides were proposed to represent the southward subduction-related main arc and back-arc regions, respectively (e.g. Bektas *et al.*, 2001; Dokuz & Tanyolu, 2006; Dokuz *et al.*, 2010, 2019; Eyuboglu *et al.*, 2016, 2019).

In the Yusufeli region, both of the Yusufeli and Camlikaya intrusive complexes were emplaced into the Paleozoic–Triassic basement, indicating intrusion into continental lithosphere (Fig. 1c). The Yusufeli intrusive complex is positioned in the hanging wall of the regional NE–SE Eocene thrusts whereas the Camlikaya intrusive complex, with similar volume to the Yusufeli intrusive complex, belongs to the footwall of the thrusts (Fig. 1c and d). This observation suggests that the Yusufeli intrusive complex has been thrust from SE to NW, and the Yusufeli and Camlikaya intrusive complexes were emplaced at a greater distance apart in the Jurassic than their present-day locations. However, it is difficult to reconstruct their locations at that time. In the context of the regional geology of the Eastern Pontides and the two geodynamic models discussed above, we put forward two possible scenarios that could explain the petrogenesis and the spatial distribution of the Yusufeli and Camlikaya intrusive complexes.

In scenario 1, the tholeiitic Yusufeli and the calc-alkaline Camlikaya intrusive complexes were generated in the fore-arc and the main arc, respectively. This scenario can be attributed to the northward subduction of the northern branch of the Neotethys oceanic lithosphere (Fig. 15a). In this case, the damp tholeiitic parental magma of the Yusufeli intrusive complex is derived from the mantle wedge beneath the fore-arc, produced by decompression melting, and follows a tholeiitic differentiation trend. Decompression melting beneath the fore-arc is potentially related to the extensional setting recorded in the Lower–Middle Jurassic sediments and structures (e.g. Yilmaz *et al.*, 1998; Dokuz & Tanyolu, 2006). In general, the low temperature (~600–800 °C) of the mantle wedge corner cannot result in amphibole and chlorite (± serpentine) breakdown at the vapor-saturated solidus, and the magma without or with little H_2O would be frozen as being thermally equilibrated with the surrounding mantle peridotite (e.g. Grove *et al.*, 2009, 2012). However, primitive dry or damp magma has been proposed to be generated in the fore-arc to the main arc during a transient episode of hot, shallow mantle melting in the Cascades (Elkins-Tanton *et al.*, 2001; Grove *et al.*, 2002). Other studies have also suggested that mantle upwelling and decompression melting related to the initial subduction process produced tholeiitic magmatism in the Izu–Bonin–Mariana fore-arc (e.g. Reagan *et al.*, 2008; Ishizuka *et al.*, 2018). After subduction initiation, during the northward

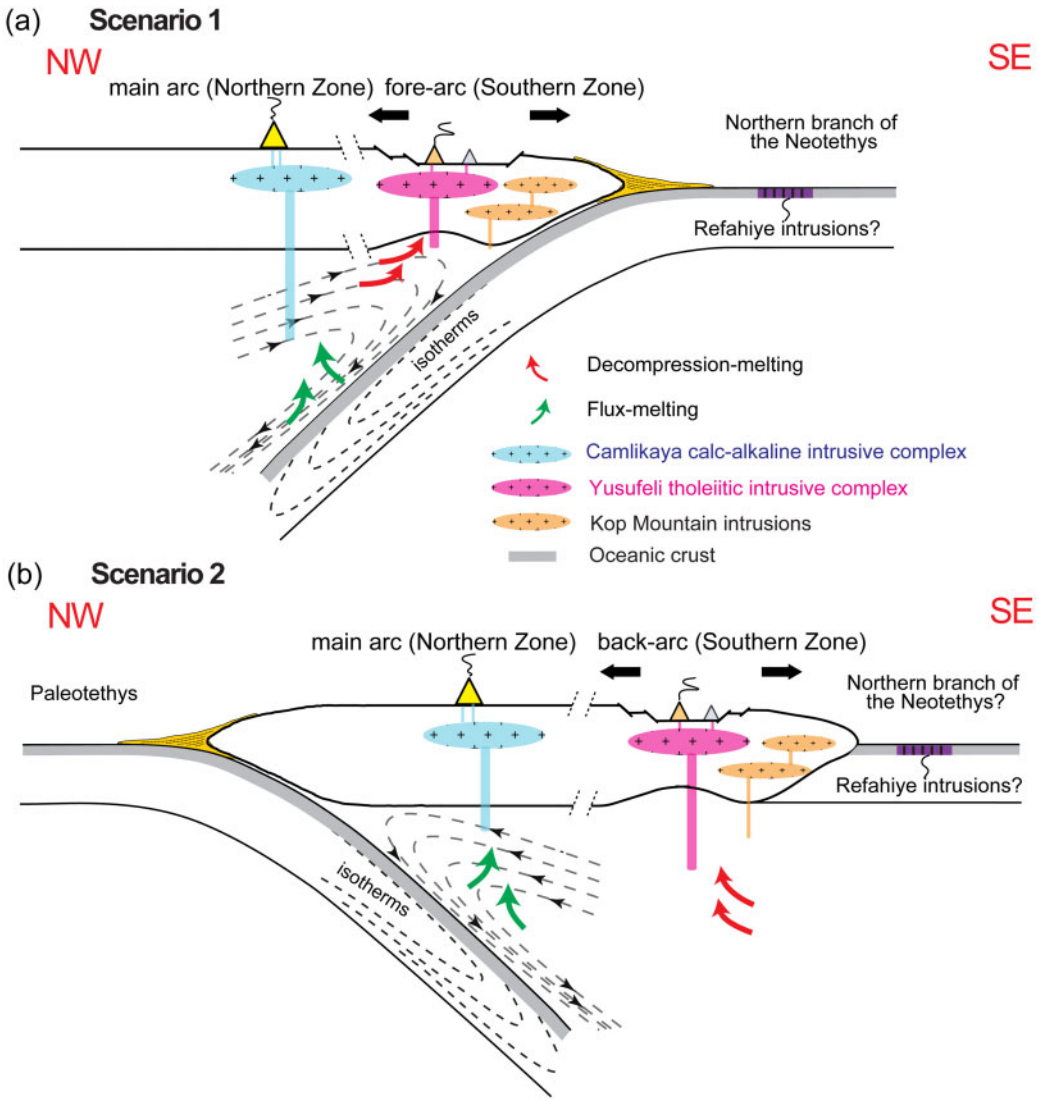

Fig. 15. Schematic illustrations showing two possible scenarios for the geodynamic evolution of the Eastern Pontides during the Jurassic. In scenario 1, the tholeiitic Yusufeli and calc-alkaline Camlikaya intrusive complexes are interpreted to be produced in the fore-arc and the main arc, respectively, corresponding to the northward subduction of the northern branch of the Neotethys oceanic lithosphere. In scenario 2, the southward subduction of the Paleotethys oceanic lithosphere generated the tholeiitic Yusufeli and calc-alkaline Camlikaya intrusive complexes in the back-arc and the main arc, respectively. (See text for detailed descriptions.)

subduction of the northern branch of the Neotethys oceanic lithosphere, the dehydration of hydrous minerals in the subducting oceanic lithosphere and sediments (e.g. chlorite, serpentine, and amphibole) can release fluids, which trigger the flux-melting of the mantle wedge to produce the wet parental magma of the Camlikaya intrusive complex (e.g. Schmidt & Poli 1998; Grove *et al.*, 2002, 2012). Subsequently, the wet Camlikaya parental magma follows a calc-alkaline differentiation trend at crustal levels.

In an alternative scenario 2, the generation of the Yusufeli and Camlikaya intrusive complexes is related to the southward subduction of the Paleotethys oceanic lithosphere (Fig. 15b). This interpretation assumes that during the Early–Middle Jurassic, the opening of a back-arc basin in the Southern Zone may have resulted in the generation of the damp tholeiitic magmatism that produced the Yusufeli intrusive complex (e.g. Yilmaz *et al.*, 1998; Dokuz & Tanyolu, 2006; Dokuz *et al.*, 2010; Eyuboglu *et al.*, 2016), as a result of decompression melting of the mantle wedge in an extensional setting. In contrast, the generation of the wet calc-alkaline magmatism that formed the Camlikaya intrusive complex can be linked with flux melting of the mantle wedge in the main arc. Some of the geochemical characteristics would be consistent with this scenario (i.e. TiO_2; Fig. 14b), as most of the Yusufeli intrusive rocks follow the LLDs displayed by the volcanic rocks in the Mariana Trough dominated by H_2O-poor tholeiitic rocks (e.g. Brounce *et al.*, 2014). The LLD of the Camlikaya intrusive rocks matches those of volcanic rocks from the Mariana and Cascades main arcs. In addition, scenario

2 would be consistent with global observations in modern arcs showing that tholeiitic magmatism predominates in back-arc settings compared with the voluminous calc-alkaline magmatism in the main arc settings (e.g. Hawkesworth *et al.*, 1977; Hunter, 1998; Donnelly-Nolan *et al.*, 2008; Grove *et al.*, 2012; Francalanci & Zellmer, 2019).

We note that coeval (hornblende) gabbro and tonalite intrusions (~181–176 Ma) and trondhjemite and (hornblende) gabbro intrusions (~186–178 Ma) were also documented in Kop Mountain and Refahiye within the İzmir–Ankara–Erzincan suture zone (Fig. 1b). The Kop Mountain intrusions are characterized by bimodal distributions in terms of major elements (Figs 7 and 8) and approximately flat REE patterns (Fig. 9a and b). These intrusions have been suggested to be generated in a rifted back-arc environment or an incipient subduction zone (i.e. fore-arc) in analogy to the Oman ophiolites (Eyuboglu *et al.*, 2016). Within the frame of our proposed scenarios, the Kop Mountain intrusions can be interpreted either as fore-arc magmatism corresponding to the initial magmatism during the northward subduction of the northern branch of the Neotethys oceanic lithosphere in scenario 1 or as back-arc magmatism related to the southward subduction of the Paleotethys oceanic lithosphere in scenario 2 (Fig. 15). The Refahiye intrusions characterized by MORB-like REE patterns are proposed to represent part of ophiolites formed in a mid-ocean ridge or suprasubduction-zone settings (Topuz *et al.*, 2013; Uysal *et al.*, 2015). Therefore, in both scenarios 1 and 2, the Refahiye intrusions should be the relicts of the northern branch of the Neotethys (Fig. 15).

In conclusion, the geochemical compositions and spatial relationship of the tholeiitic Yusufeli and the calc-alkaline Camlikaya intrusive complexes tend to favor scenario 2 (southward subduction) compared with scenario 1 (northward subduction). However, we acknowledge that the geochemical data alone cannot preclude the possibility of scenario 1 (i.e. the northward subduction of the northern branch of the Neotethys). It is noteworthy that an ~20 Myr time lag between the Yusufeli and Camlikaya intrusive complexes provides sufficient time for the migration of arc magmatism owing to slab-dip variation. For a better understanding of the geodynamic evolution of the Eastern Pontides, complementary detailed structural geology combined with high-precision geochronology and geochemistry studies are required to place tighter constraints on the spatial and temporal evolution of the Jurassic magmatism exposed in this region.

CONCLUSIONS

1. The Yusufeli and Camlikaya intrusive complexes exposed in the Yusufeli region the Eastern Pontides arc, NE Turkey, were emplaced at 179–170 Ma and 151–147 Ma, respectively.
2. The Yusufeli intrusive complex is mainly characterized by low- and medium-K tholeiitic affinities with depleted Hf isotopic compositions, whereas the Camlikaya intrusive complex has medium- and high-K calc-alkaline affinities with relatively enriched Hf isotopic compositions.
3. Driven by cooling and/or decompression in open magmatic systems at a depth of ~5–8 km (~150–250 MPa), the Yusufeli magmas are characterized by plagioclase- and clinopyroxene-dominated fractional crystallization, whereas the Camlikaya magmas are characterized by amphibole-dominated fractional crystallization.
4. The petrographic observations, LLDs, trace element ratios, and REE and Rhyolite-MELTS modeling results all suggest that the Yusufeli intrusive rocks are derived from damp (~1–2 wt% H_2O) parental magmas as a result of decompression melting of the back-arc or fore-arc mantle wedge, and the Camlikaya intrusive rocks are derived from wet (>2 wt% H_2O) parental magmas linked with flux melting of the mantle wedge in the main arc.
5. Combined with the regional sedimentary and structural records in the Southern Zone, the spatial relationship and LLDs of the Yusufeli and Camlikaya magmatism seem to be most consistent with the southward subduction of the Paleotethys oceanic lithosphere during the Jurassic.

ACKNOWLEDGEMENTS

The authors knowledge the fruitful discussions with Nilanja Chatterjee and Liang-Liang Zhang during the early stage of preparation of this paper, and the language editing by Zachary Molitor. Constructive comments by Tod Waight, Prelević Dejan and one anonymous reviewer, and editorial handling by Tod Waight, Marjorie Wilson, and Georg Zellmer are greatly appreciated. This is CUGB petro-geochemical contribution No. PGC2015-0062.

FUNDING

This work was financially co-supported by the MOST of China (2016YFC0600304 and 2016YFC0600407), the Chinese National Natural Science Foundation (91755207 and 41225006), the 111 project (B18048), and the MOST Special Fund from the State Key Laboratory of Geological Processes and Mineral Resources (China University of Geosciences) (MSFGPMR201802). H. Rezeau acknowledges support by the Swiss National Foundation through the early post-doc mobility research grant P2GEP2_178008 and the post-doc mobility research grant P400P2_194421. The work of O. Jagoutz and H. Rezeau was supported by the National Science Foundation (EAR-1552202). Z. Liu acknowledges financial support from the International Postdoctoral Exchange Fellowship Program (No. 2020028).

DATA AVAILABILITY STATEMENT

The data underlying this article are available in the article and in its online Supplementary Material.

SUPPLEMENTARY DATA

Supplementary data are available at *Journal of Petrology* online.

REFERENCES

Adamia, S A., Lordkipanidze, M. & Zakariad, G. (1977). Evolution of an active continental margin as exemplified by the Alpine history of the Caucasus. *Tectonophysics* **40**, 183–199.

Anderson, A. T. (1979). Water in some hypersthenic magmas. *Journal of Geology* **87**, 509–531.

Andersen, T. (2002). Correction of common lead in U–Pb analyses that do not report ^{204}Pb. *Chemical Geology* **192**, 59–79.

Armstrong, J. T. (1995). Citzaf—a package of correction programs for the quantitative Electron Microbeam X-ray-analysis of thick polished materials, thin-films, and particles. *Microbeam Analysis* **4**, 177–200.

Arslan, M. & Aliyaziciğolu, I. (2001). Geochemical and petrological characteristics of the Kale (Gümüshane) volcanic rocks: implications for the Eocene evolution of eastern Pontide arc volcanism, northeast Turkey. *International Geology Review* **43**, 595–610.

Ballato, P., Parra, M., Schildgen, T. F., Dunkl, I., Yıldırım, C., Özsayın, E., Sobel, E. R., Echtler, H. & Strecker, M. R. (2018). Multiple exhumation phases in the Central Pontides (N Turkey): new temporal constraints on major geodynamic changes associated with the closure of the Neo-Tethys Ocean. *Tectonics* **37**, 1831–1857.

Beard, J. S. (1995). Experimental, geological, and geochemical constraints on the origins of low-K silicic magmas in oceanic arcs. *Journal of Geophysical Research: Solid Earth* **100**, 15593–15600.

Bektas, O., Yılmaz, C., Taslı, K., Akdağ, K. & Özgür, S. (1995). Cretaceous rifting of the eastern Pontide carbonate platform (NE Turkey): the formation of carbonates breccias and turbidites as evidences of a drowned platform. *Geologia* **57**, 233–244.

Bektas, O., Capkinoglu, S. & Akdag, K. (2001). Successive extensional tectonic regimes during the Mesozoic as evidenced by neptunian dikes in the Pontide Magmatic Arc, Northeast Turkey. *International Geology Review* **43**, 840–849.

Blichert-Toft, J. (2008). The Hf isotopic composition of zircon reference material 91500. *Chemical Geology* **253**, 252–257.

Blichert-Toft, J., Chauvel, C. & Albarède, F. (1997). Separation of Hf and Lu for high-precision isotope analysis of rock samples by magnetic sector-multiple collector ICP-MS. *Contributions to Mineralogy and Petrology* **127**, 248–260.

Bloomer, S. H., Stern, R. J., Fisk, E. & Geschwind, C. H. (1989). Shoshonitic volcanism in the Northern Mariana Arc: 1. Mineralogic and major and trace element characteristics. *Journal of Geophysical Research: Solid Earth* **94**, 4469–4496.

Bomparola, R. M., Ghezzo, C., Belousova, E., Griffin, W. L. & O'Reilly, S. Y. (2007). Resetting of the U–Pb zircon system in Cambro-Ordovician intrusives of the Deep Freeze Range, Northern Victoria Land, Antarctica. *Journal of Petrology* **48**, 327–364.

Boztuğ, D. & Harlavan, Y. (2008). K–Ar ages of granitoids unravel the stages of Neo-Tethyan convergence in the eastern Pontides and central Anatolia. *International Journal of Earth Sciences* **97**, 585–599.

Brounce, M. N., Kelley, K. A. & Cottrell, E. (2014). Variations in $Fe^{3+}/\sum Fe$ of Mariana arc basalts and mantle wedge fO_2. *Journal of Petrology* **55**, 2513–2536.

Bucholz, C. E., Jagoutz, O., Schmidt, M. W. & Sambuu, O. (2014). Fractional crystallization of high-K arc magmas: biotite- versus amphibole-dominated fractionation series in the Dariv Igneous Complex, Western Mongolia. *Contributions to Mineralogy and Petrology* **168**, 1–28.

Catlos, E. J., Huber, K. & Shin, T. A. (2013). Geochemistry and geochronology of meta-igneous rocks from the Tokat Massif, north–central Turkey: implications for Tethyan reconstructions. *International Journal of Earth Sciences* **102**, 2175–2198.

Coleman, D. S., Gray, W. & Glazner, A. F. (2004). Rethinking the emplacement and evolution of zoned plutons: geochronologic evidence for incremental assembly of the Tuolumne Intrusive Suite. *Geology* **32**, 433–436.

Davidson, J., Morgan, D. J., Charlier, B. L. A., Harlou, R. & Hora, J. M. (2007a). Microsampling and isotopic analysis of igneous rocks: implications for the study of magmatic systems. *Annual Review of Earth and Planetary Sciences* **35**, 273–311.

Davidson, J., Turner, S., Handley, H., Macpherson, C. & Dosseto, A. (2007b). Amphibole "sponge" in arc crust? *Geology* **35**, 787–790.

de Moor, J. M., Fischer, T. P., Hilton, D. R., Hauri, E., Jaffe, L. A. & Camacho, J. T. (2005). Degassing at Anatahan volcano during the May 2003 eruption: implications from petrology, ash leachates, and SO_2 emissions. *Journal of Volcanology and Geothermal Research* **146**, 117–138.

Deer, W. A., Howie, R. A. & Zussman, J. (1992). *An Introduction to the Rock-Forming Minerals*, 2nd edn. Harlow: Longman.

Deng, Z., Chaussidon, M., Savage, P., Robert, F., Pik, R. & Moynier, F. (2019). Titanium isotopes as a tracer for the plume or island arc affinity of felsic rocks. *Proceedings of the National Academy of Sciences of the USA* **116**, 1132–1135.

Dessimoz, M., Müntener, O. & Ulmer, P. (2012). A case for hornblende dominated fractionation of arc magmas: the Chelan Complex (Washington Cascades). *Contributions to Mineralogy and Petrology* **163**, 567–589.

Dewey, J. F., Pitman, W. C., Ryan, W. B. F. & Bonnin, J. (1973). Plate tectonics and the evolution of the alpine system. *Geological Society of America Bulletin* **84**, 3137–3180.

Dietrich, V., Emmermann, R., Oberhänsli, R. & Puchelt, H. (1978). Geochemistry of basaltic and gabbroic rocks from the West Mariana basin and the Mariana trench. *Earth and Planetary Science Letters* **39**, 127–144.

Dokuz, A. (2011). A slab detachment and delamination model for the generation of Carboniferous high-potassium I-type magmatism in the Eastern Pontides, NE Turkey: the Köse composite pluton. *Gondwana Research* **19**, 926–944.

Dokuz, A. & Tanyolu, E. (2006). Geochemical constraints on the provenance, mineral sorting and subaerial weathering of lower Jurassic and upper Cretaceous clastic rocks of the Eastern Pontides, Yusufeli (Artvin), NE Turkey. *Turkish Journal of Earth Sciences* **15**, 181–209.

Dokuz, A., Karsli, O., Chen, B. & Uysal, İ. (2010). Sources and petrogenesis of Jurassic granitoids in the Yusufeli area, Northeastern Turkey: implications for pre- and post-collisional lithospheric thinning of the eastern Pontides. *Tectonophysics* **480**, 259–279.

Dokuz, A., Aydınçakır, E., Kandemir, R., Karslı, O., Siebel, W., Derman, A. S. & Turan, M. (2017). Late Jurassic magmatism and stratigraphy in the Eastern Sakarya Zone, Turkey:

evidence for the slab breakoff of Paleotethyan oceanic lithosphere. *Journal of Geology* **125**, 1–31.

Dokuz, A. & Sünnetçi, K. (2019). Jurassic acidic magmatism in a back-arc setting, eastern Sakarya Zone, Turkey: Geochemical constraints and an evolutionary model. *Lithos* 332–333, 312–327.

Donnelly-Nolan, J. M., Grove, T. L., Lanphere, M. A., Champion, D. E. & Ramsey, D. W. (2008). Eruptive history and tectonic setting of Medicine Lake Volcano, a large rear-arc volcano in the southern Cascades. *Journal of Volcanology and Geothermal Research* **177**, 313–328.

du Bray, E. A., John, D. A., Sherrod, D. R., Evarts, R. C., Conrey, R. M. & Lexa, J. (2006). *Geochemical database for volcanic rocks of the western Cascades, Washington, Oregon, and California. US Geological Survey Data Series* **155**, 49 pp.

Elkins-Tanton, L. T., Grove, T. L. & Donnelly-Nolan, J. (2001). Hot, shallow mantle melting under the Cascades volcanic arc. *Geology* **29**, 631–634.

Eyuboglu, Y. (2006). Three-directional extensional deformation and formation of the Liassic rift basins in the Eastern Pontides (NE Turkey). *Geologica Carpathica* **57**, 337–346.

Eyuboglu, Y. (2015). Petrogenesis and U–Pb zircon chronology of felsic tuffs interbedded with turbidites (Eastern Pontides Orogenic Belt, NE Turkey): implications for Mesozoic geodynamic evolution of the eastern Mediterranean region and accumulation rates of turbidite sequences. *Lithos* **212–215**, 74–92.

Eyuboglu, Y., Bektas, O. & Pul, D. (2007). Mid-Cretaceous olistostromal ophiolitic mélange developed in the back-arc basin of the Eastern Pontide Magmatic Arc, Northeast Turkey. *International Geology Review* **49**, 1103–1126.

Eyuboglu, Y., Dilek, Y., Bozkurt, E., Bektas, O., Rojay, B. & Sen, C. (2010). Structure and geochemistry of an Alaskan-type ultramafic–mafic complex in the Eastern Pontides, NE Turkey. *Gondwana Research* **18**, 230–252.

Eyuboglu, Y., Dudas, F. O., Santosh, M., Xiao, Y., Yi, K., Chatterjee, N., Wu, F. Y. & Bektaş, O. (2016). Where are the remnants of a Jurassic ocean in the eastern Mediterranean region? *Gondwana Research* **33**, 63–91.

Eyuboglu, Y., Dudas, F. O., Thorkelson, D., Zhu, D.-C., Liu, Z., Chatterjee, N., Yi, K. & Santosh, M. (2017). Eocene granitoids of northern Turkey: polybaric magmatism in an evolving arc–slab window system. *Gondwana Research* **50**, 311–345.

Eyuboglu, Y., Dudas, F. O., Chatterjee, N., Santosh, M., Billor, M. Z. & Yuva, S. (2018). Petrology, geochronology and tectonic setting of early Triassic alkaline metagabbros from the Eastern Pontide Orogenic Belt (NE Turkey): implications for the geodynamic evolution of Gondwana's Early Mesozoic Northern Margin. *Tectonics* **37**, 3174–3206.

Eyuboglu, Y., Dudas, F. O., Zhu, D.-C., Liu, Z. & Chatterjee, N. (2019). Late Cretaceous I- and A-type magmas in eastern Turkey: magmatic response to double-sided subduction of Paleo- and Neo-Tethyan lithospheres. *Lithos* **326–327**, 39–70.

Francalanci, L. & Zellmer, G. F. (2019). Magma genesis at the South Aegean Volcanic Arc. *Elements* **15**, 165–170.

Fine, G. & Stolper, E. (1986). Dissolved carbon dioxide in basaltic glasses: concentrations and speciation. *Earth and Planetary Science Letters* **76**, 263–278.

Fryer, P., Sinton, J. & Philpotts, J. A. (1982). Basaltic glasses from the Mariana Trough. Initial Reports of the Deep Sea Drilling Project **60**, 601–609.

Fryer, P., Gill, J. B. & Jackson, M. C. (1997). Volcanologic and tectonic evolution of the Kasuga seamounts, northern Mariana Trough: Alvin submersible investigations. *Journal of Volcanology and Geothermal Research* **79**, 277–311.

Gale, A., Dalton, C. A., Langmuir, C. H., Su, Y. & Schilling, J. G. (2013). The mean composition of ocean ridge basalts. *Geochemistry, Geophysics, Geosystems* **14**, 489–518.

Galoyan, G., Rolland, Y., Sosson, M., Corsini, M., Billo, S., Verati, C. & Melkonyan, R. (2009). Geology, geochemistry and $^{40}Ar/^{39}Ar$ dating of Sevan ophiolites (Lesser Caucasus, Armenia): evidence for Jurassic back-arc opening and hot spot event between the South Armenian Block and Eurasia. *Journal of Asian Earth Sciences* **34**, 135–153.

Ghiorso, M. S. & Gualda, G. A. R. (2015). An H_2O–CO_2 mixed fluid saturation model compatible with rhyolite-MELTS. *Contributions to Mineralogy and Petrology* **169**, 53.

Gill, J. B. (1981). What is "Typical Calcalkaline Andesite"? In: Gill, J. B. (ed.) *Orogenic Andesites and Plate Tectonics*. Berlin: Springer, pp. 1–12.

Gribble, R. F., Stern, R. J., Bloomer, S. H., Stüben, D., O'Hearn, T. & Newman, S. (1996). MORB mantle and subduction components interact to generate basalts in the southern Mariana Trough back-arc basin. *Geochimica et Cosmochimica Acta* **60**, 2153–2166.

Gribble, R. F., Stern, R. J., Newman, S., Bloomer, S. H. & O'Hearn, T. (1998). Chemical and isotopic composition of lavas from the Northern Mariana Trough: implications for magmagenesis in back-arc basins. *Journal of Petrology* **39**, 125–154.

Grove, T. L. & Baker, M. B. (1984). Phase equilibrium controls on the tholeiitic versus calc-alkaline differentiation trends. *Journal of Geophysical Research: Solid Earth* **89**, 3253–3274.

Grove, T., Parman, S., Bowring, S., Price, R. & Baker, M. (2002). The role of an H_2O-rich fluid component in the generation of primitive basaltic andesites and andesites from the Mt. Shasta region, N California. *Contributions to Mineralogy and Petrology* **142**, 375–396.

Grove, T. L., Elkins-Tanton, L. T., Parman, S. W., Chatterjee, N., Müntener, O. & Gaetani, G. A. (2003). Fractional crystallization and mantle-melting controls on calc-alkaline differentiation trends. *Contributions to Mineralogy and Petrology* **145**, 515–533.

Grove, T. L., Till, C. B., Lev, E., Chatterjee, N. & Medard, E. (2009). Kinematic variables and water transport control the formation and location of arc volcanoes. *Nature* **459**, 694–697.

Grove, T. L., Till, C. B. & Krawczynski, M. J. (2012). The role of H_2O in subduction zone magmatism. *Annual Review of Earth and Planetary Sciences* **40**, 413–439.

Gualda, G. A. R., Ghiorso, M. S., Lemons, R. V. & Carley, T. L. (2012). Rhyolite-MELTS: a modified calibration of MELTS optimized for silica-rich, fluid-bearing magmatic systems. *Journal of Petrology* **53**, 875–890.

Güven, İ. (1993). *Doğu Pontidler'in 1:25000 ölçekli jeolojisi ve kompilasyonu* [1:25000 Scale Geology and Compilation of the Eastern Pontide]. Ankara: General Directorate of Mineral Research and Exploration of Turkey (MTA).

Hart, S. R., Glassley, W. E. & Karig, D. E. (1972). Basalts and sea floor spreading behind the Mariana Island arc. *Earth and Planetary Science Letters* **15**, 12–18.

Hässig, M., Rolland, Y. & Sosson, M. (2017). From seafloor spreading to obduction: Jurassic–Cretaceous evolution of the northern branch of the Neotethys in the Northeastern Anatolian and Lesser Caucasus regions. In: *Geological Society, London, Special Publications* **428**, 41–60.

Hawkesworth, C., O'Nions, R., Pankhurst, R., Hamilton, P. & Evensen, N. (1977). A geochemical study of island-arc and back-arc tholeiites from the Scotia Sea. *Earth and Planetary Science Letters* **36**, 253–262.

Hawkesworth, C., Gallagher, K., Hergt, J. & McDermott, F. (1993). Mantle and slab contributions in arc magmas. *Annual Review of Earth and Planetary Sciences* **21**, 175–204.

Hawkins, J. W. & Melchior, J. T. (1985). Petrology of Mariana Trough and Lau Basin basalts. *Journal of Geophysical Research* **90**, 11431–11468.

Hawkins, J. W., Lonsdale, P. F., Macdougall, J. D. & Volpe, A. M. (1990). Petrology of the axial ridge of the Mariana Trough backarc spreading center. *Earth and Planetary Science Letters* **100**, 226–250.

Holland, T. & Blundy, J. (1994). Non-ideal interactions in calcic amphiboles and their bearing on amphibole–plagioclase thermometry. *Contributions to Mineralogy and Petrology* **116**, 433–447.

Humphreys, M. C. S., Blundy, J. D. & Sparks, R. S. J. (2006). Magma evolution and open-system processes at Shiveluch Volcano: insights from phenocryst zoning. *Journal of Petrology* **47**, 2303–2334.

Hunter, A. G. (1998). Intracrustal controls on the coexistence of tholeiitic and calc-alkaline magma series at Aso Volcano, SW Japan. *Journal of Petrology* **39**, 1255–1284.

Hunter, A. G. & Blake, S. (1995). Petrogenetic evolution of a transitional tholeiitic–calc-alkaline series: Towada Volcano, Japan. *Journal of Petrology* **36**, 1579–1605.

Ikeda, Y., Nagao, K., Stern, R. J., Yuasa, M. & Newman, S. (1998). Noble gases in pillow basalt glasses from the northern Mariana Trough back-arc basin. *Island Arc* **7**, 471–478.

Ikeda, Y., Nagao, K., Ishii, T., Matsumoto, D., Stern, R. J., Kagami, H., Arima, M. & Bloomer, S. H. (2016). Contributions of slab fluid and sediment melt components to magmatism in the Mariana Arc–Trough system: evidence from geochemical compositions and Sr, Nd, and noble gas isotope systematics. *Island Arc* **25**, 253–273.

Irvine, T. & Baragar, W. (1971). A guide to the chemical classification of the common volcanic rocks. *Canadian Journal of Earth Sciences* **8**, 523–548.

Ishizuka, O., Tani, K. & Reagan, M. K. (2014). Izu–Bonin–Mariana Forearc crust as a modern ophiolite analogue. *Elements* **10**, 115–120.

Ishizuka, O., Hickey-Vargas, R., Arculus, R. J., Yogodzinski, G. M., Savov, I. P., Kusano, Y., McCarthy, A., Brandl, P. A. & Sudo, M. (2018). Age of Izu–Bonin–Mariana arc basement. *Earth and Planetary Science Letters* **481**, 80–90.

Jackson, S. E., Pearson, N. J., Griffin, W. L. & Belousova, E. A. (2004). The application of laser ablation-inductively coupled plasma-mass spectrometry to *in situ* U–Pb zircon geochronology. *Chemical Geology* **211**, 47–69.

Jagoutz, O. E. (2010). Construction of the granitoid crust of an island arc. Part II: a quantitative petrogenetic model. *Contributions to Mineralogy and Petrology* **160**, 359–381.

Jagoutz, O. (2013). Were ancient granitoid compositions influenced by contemporaneous atmospheric and hydrosphere oxidation states? *Terra Nova* **25**, 95–101.

Jagoutz, O., Müntener, O., Schmidt, M. W. & Burg, J. P. (2011). The roles of flux- and decompression melting and their respective fractionation lines for continental crust formation: Evidence from the Kohistan arc. *Earth and Planetary Science Letters* **303**, 25–36.

Jagoutz, O., Schmidt, M. W., Enggist, A., Burg, J.-P., Hamid, D. & Hussain, S. (2013). TTG-type plutonic rocks formed in a modern arc batholith by hydrous fractionation in the lower arc crust. *Contributions to Mineralogy and Petrology* **166**, 1099–1118.

Jorgenson, D. B. (1971). Origin of patchy zoning in plagioclase from gabbroic rocks of Southwestern Oregon. *Geological Society of America Bulletin* **82**, 2667–2670.

Kandemir, R. & Yılmaz, C. (2009). Lithostratigraphy, facies, and deposition environment of the lower Jurassic Ammonitico Rosso type sediments (ARTS) in the Gümüşhane area, NE Turkey: implications for the opening of the northern branch of the Neo-Tethys Ocean. *Journal of Asian Earth Sciences* **34**, 586–598.

Karsli, O., Dokuz, A. & Kandemir, R. (2017). Zircon Lu–Hf isotope systematics and U–Pb geochronology, whole-rock Sr–Nd isotopes and geochemistry of the early Jurassic Gokcedere pluton, Sakarya Zone–NE Turkey: a magmatic response to roll-back of the Paleo-Tethyan oceanic lithosphere. *Contributions to Mineralogy and Petrology* **172**, 31.

Kaygusuz, A., Arslan, M., Siebel, W., Sipahi, F., Ilbeyli, N. & Temizel, I. (2014). LA-ICP MS zircon dating, whole-rock and Sr–Nd–Pb–O isotope geochemistry of the Camibogazi pluton, Eastern Pontides, NE Turkey: implications for lithospheric mantle and lower crustal sources in arc-related I-type magmatism. *Lithos* **192–195**, 271–290.

Kaygusuz, A., Arslan, M., Sipahi, F. & Temizel, İ. (2016). U–Pb zircon chronology and petrogenesis of Carboniferous plutons in the northern part of the Eastern Pontides, NE Turkey: constraints for Paleozoic magmatism and geodynamic evolution. *Gondwana Research* **39**, 327–346.

Kelemen, P. B., Hanghøj, K. & Greene, A. R. (2014). One view of the geochemistry of subduction-related magmatic arcs, with an emphasis on primitive andesite and lower crust. In: Holland, H. D. & Turekian, K. K. (ed.) *Treatise on Geochemistry*, 2nd edn. Oxford: Elsevier, pp. 749–806.

Kelley, K. A. & Cottrell, E. (2012). The influence of magmatic differentiation on the oxidation state of Fe in a basaltic arc magma. *Earth and Planetary Science Letters* **329–330**, 109–121.

Kirkland, C. L., Smithies, R. H., Taylor, R. J. M., Evans, N. & McDonald, B. (2015). Zircon Th/U ratios in magmatic environs. *Lithos* **212–215**, 397–414.

Koch, R., Bucur, I. I., Kirmaci, M. Z., Eren, M. & Tasli, K. (2008). Upper Jurassic and Lower Cretaceous carbonate rocks of the Berdiga Limestone—Sedimentation on an onbound platform with volcanic and episodic siliciclastic influx. Biostratigraphy, facies and diagenesis (Kircaova, Kale–Gümüşhane area; NE-Turkey). *Neues Jahrbuch für Geologie und Paläontologie, Abhandlungen* **247**, 23–61.

Kohut, E. J., Stern, R. J., Kent, A. J. R., Nielsen, R. L., Bloomer, S. H. & Leybourne, M. (2006). Evidence for adiabatic decompression melting in the Southern Mariana Arc from high-Mg lavas and melt inclusions. *Contributions to Mineralogy and Petrology* **152**, 201–221.

Korkmaz, S., Tüysüz, N., Er, M., Musaoğlu, A. & Keskin, I. (1995). *Stratigraphy of the eastern Pontides, NE Turkey. Geology of the Black Sea Region*. Ankara: General Directorate of Mineral Research and Exploration, and Chamber of Geological Engineers, pp. 59–69.

Kurzawa, T., König, S., Alt, J. C., Yierpan, A. & Schoenberg, R. (2019). The role of subduction recycling on the selenium isotope signature of the mantle: constraints from Mariana arc lavas. *Chemical Geology* **513**, 239–249.

Leake, B. E., Woolley, A. R., Arps, C. E. S., Birch, W. D., Gilbert, M. C., Grice, J. D., Hawthorne, F. C., Kato, A., Kisch, H. J., Krivovichev, V. G., Linthout, K., Laird, J., Mandarino, J., Maresch, W. V., Nickel, E. H., Rock, N. M. S., Schumacher, J. C., Smith, D. C., Stephenson, N. C. N., Ungaretti, L., Whittaker, E. J. W. & Youzhi, G. (1997). Report. Nomenclature of Amphiboles: Report of the Subcommittee on Amphiboles of the International Mineralogical Association Commission on New Minerals and Mineral Names. *Mineralogical Magazine* **295**.

Lee, C. T. A. & Bachmann, O. (2014). How important is the role of crystal fractionation in making intermediate magmas? Insights from Zr and P systematics. *Earth and Planetary Science Letters* **393**, 266–274.

Leeman, W. P., Smith, D. R., Hildreth, W., Palacz, Z. & Rogers, N. (1990). Compositional diversity of Late Cenozoic basalts in a transect across the southern Washington Cascades: implications for subduction zone magmatism. *Journal of Geophysical Research* **95**, 19561–19582.

Liu, Y., Gao, S., Hu, Z., Gao, C., Zong, K. & Wang, D. (2010). Continental and oceanic crust recycling-induced melt–peridotite interactions in the Trans-North China Orogen: U–Pb dating, Hf isotopes and trace elements in zircons from mantle xenoliths. *Journal of Petrology* **51**, 537–571.

Liu, Z., Zhu, D. C., Wang, Q., Eyuboglu, Y., Zhao, Z. D., Liu, S. A. & Xu, L. J. (2018). Transition from low-K to high-K calc-alkaline magmatism at approximately 84 Ma in the Eastern Pontides (NE Turkey): magmatic response to slab rollback of the Black Sea. *Journal of Geophysical Research: Solid Earth* **123**, 7604–7628.

Lonsdale, P. & Hawkins, J. (1985). Silicic volcanism at an off-axis geothermal field in the Mariana Trough back-arc basin. *Geological Society of America Bulletin* **96**, 940–951.

Ludwig, K. R. (2011). *Isoplot/Ex Version 4.15: A geochronological toolkit for Microsoft Excel: Geochronology Center Berkeley, v. 4.*

Macpherson, C. G., Dreher, S. T. & Thirlwall, M. F. (2006). Adakites without slab melting: high pressure differentiation of island arc magma, Mindanao, the Philippines. *Earth and Planetary Science Letters* **243**, 581–593.

Mandler, B. E., Donnelly-Nolan, J. M. & Grove, T. L. (2014). Straddling the tholeiitic/calc-alkaline transition: the effects of modest amounts of water on magmatic differentiation at Newberry Volcano. *Contributions to Mineralogy and Petrology* **168**, 1066.

Marske, J. P., Pietruszka, A. J., Trusdell, F. A. & Garcia, M. O. (2011). Geochemistry of southern Pagan Island lavas, Mariana arc: the role of subduction zone processes. *Contributions to Mineralogy and Petrology* **162**, 231–252.

McNulty, B. A., Tong, W. & Tobisch, O. T. (1996). Assembly of a dike-fed magma chamber: the Jackass Lakes pluton, central Sierra Nevada, California. *Geological Society of America Bulletin* **108**, 926–940.

Merzbacher, C. & Eggler, D. H. (1984). A magmatic geohygrometer: application to Mount St. Helens and other dacitic magmas. *Geology* **12**, 587–590.

Middlemost, E. A. (1994). Naming materials in the magma/igneous rock system. *Earth-Science Reviews* **37**, 215–224.

Miller, J. S., Matzel, J. E. P., Miller, C. F., Burgess, S. D. & Miller, R. B. (2007). Zircon growth and recycling during the assembly of large, composite arc plutons. *Journal of Volcanology and Geothermal Research* **167**, 282–299.

Miyashiro, A. (1974). Volcanic rock series in island arcs and active continental margins. *American Journal of Science* **274**, 321–355.

Moore, G. & Carmichael, I. S. E. (1998). The hydrous phase equilibria (to 3 kbar) of an andesite and basaltic andesite from western Mexico: constraints on water content and conditions of phenocryst growth. *Contributions to Mineralogy and Petrology* **130**, 304–319.

Morel, M. L. A., Nebel, O., Nebel-Jacobsen, Y. J., Miller, J. S. & Vroon, P. Z. (2008). Hafnium isotope characterization of the GJ-1 zircon reference material by solution and laser-ablation MC-ICPMS. *Chemical Geology* **255**, 231–235.

Moyen, J. F., Champion, D. & Smithies, R. H. (2009). The geochemistry of Archaean plagioclase-rich granites as a marker of source enrichment and depth of melting. *Earth and Environmental Science Transactions of the Royal Society of Edinburgh* **100**, 35–50.

Müntener, O. & Ulmer, P. (2018). Arc crust formation and differentiation constrained by experimental petrology. *American Journal of Science* **318**, 64–89.

Mutch, E. J. F., Blundy, J. D., Tattitch, B. C., Cooper, F. J. & Brooker, R. A. (2016). An experimental study of amphibole stability in low-pressure granitic magmas and a revised Al-in-hornblende geobarometer. *Contributions to Mineralogy and Petrology* **171**, 85.

Nandedkar, R. H., Ulmer, P. & Müntener, O. (2014). Fractional crystallization of primitive, hydrous arc magmas: an experimental study at 0·7 GPa. *Contributions to Mineralogy and Petrology* **167**, 1015.

Okay, A. I. & Şahintürk, O. (1997). Geology of the eastern Pontides. In: Robinson A. G. (ed) Regional and petroleum geology of the Black Sea and surrounding, AAPG Memoir **68**, 291–311.

Okay, A. I., Celal Şengör, A. M. & Görür, N. (1994). Kinematic history of the opening of the Black Sea and its effect on the surrounding regions. Geology **22**, 267 10.1130/0091-7613 (1994)022<0267:KHOTOO>2.3.CO;2

Okay, A. I. & Tüysüz, O. (1999). Tethyan sutures of northern Turkey. In: Durand, B., Jolivet, L., Horvath, F. & Seranne, M. (ed) The Mediterranean Basins: Tertiary Extension within the Alpine Orogen. Geological Society, London, Special Publications **156**, 475–515.

Okay, A. I., Sunal, G., Tüysüz, O., Sherlock, S., Keskin, M. & Kylander-Clark, A. R. C. (2014). Low-pressure–high-temperature metamorphism during extension in a Jurassic magmatic arc, Central Pontides, Turkey. *Journal of Metamorphic Geology* **32**, 49–69.

Osborn, E. F. (1959). Role of oxygen pressure in the crystallization and differentiation of basaltic magma. *American Journal of Science* **257**, 609–647.

Panjasawatwong, Y., Danyushevsky, L. V., Crawford, A. J. & Harris, K. L. (1995). An experimental study of the effects of melt composition on plagioclase–melt equilibria at 5 and 10 kbar: implications for the origin of magmatic high-An plagioclase. *Contributions to Mineralogy and Petrology* **118**, 420–432.

Parlak, O. (2016). The Tauride ophiolites of Anatolia (Turkey): a review. *Journal of Earth Science* **27**, 901–934.

Paton, C., Hellstrom, J., Paul, B., Woodhead, J. & Hergt, J. (2011). Iolite: freeware for the visualisation and processing of mass spectrometric data. *Journal of Analytical Atomic Spectrometry* **26**, 2508–2518.

Pearce, J. A. & Peate, D. W. (1995). Tectonic implications of the composition of volcanic ARC magmas. *Annual Review of Earth and Planetary Sciences* **23**, 251–285.

Petford, N. (1996). Dykes or diapirs? Transactions of the Royal Society of Edinburgh. Earth Sciences **87**, 105–114.

Putirka, K. (2016). Amphibole thermometers and barometers for igneous systems and some implications for eruption mechanisms of felsic magmas at arc volcanoes. *American Mineralogist* **101**, 841–858.

Rapp, R. P. & Watson, E. B. (1995). Dehydration melting of metabasalt at 8–32 kbar: implications for continental growth and crust–mantle recycling. *Journal of Petrology* **36**, 891–931.

Ratajeski, K., Sisson, T. W. & Glazner, A. F. (2005). Experimental and geochemical evidence for derivation of the El Capitan Granite, California, by partial melting of hydrous gabbroic lower crust. *Contributions to Mineralogy and Petrology* **149**, 713–734.

Reagan, M. K., Hanan, B. B., Heizler, M. T., Hartman, B. S. & Hickey-Vargas, R. (2008). Petrogenesis of volcanic rocks from Saipan and Rota, Mariana Islands, and implications for the evolution of nascent island arcs. *Journal of Petrology* **49**, 441–464.

Reagan, M. K., Ishizuka, O., Stern, R. J., Kelley, K. A., Ohara, Y., Blichert-Toft, J., Bloomer, S. H., Cash, J., Fryer, P., Hanan, B. B., Hickey-Vargas, R., Ishii, T., Kimura, J.-I., Peate, D. W., Rowe, M. C. & Woods, M. (2010). Fore-arc basalts and subduction initiation in the Izu–Bonin–Mariana system. *Geochemistry, Geophysics, Geosystems* **11**, Q03X12.

Rezeau, H., Moritz, R., Wotzlaw, J.-F., Tayan, R., Melkonyan, R., Ulianov, A., Selby, D., d'Abzac, F.-X. & Stern, R. A. (2016). Temporal and genetic link between incremental pluton assembly and pulsed porphyry Cu–Mo formation in accretionary orogens. *Geology* **44**, 627–630.

Rezeau, H., Leuthold, J., Tayan, R., Hovakimyan, S., Ulianov, A., Kouzmanov, K. & Moritz, R. (2018). Incremental growth of mid- to upper-crustal magma bodies during Arabia–Eurasia convergence and collision: a petrological study of the calc-alkaline to shoshonitic Meghri–Ordubad Pluton (Southern Armenia and Nakhitchevan, Lesser Caucasus). *Journal of Petrology* **59**, 931–966.

Rickwood, P. C. (1989). Boundary lines within petrologic diagrams which use oxides of major and minor elements. *Lithos* **22**, 247–263.

Ringwood, A. E. (1974). The petrological evolution of island arc systems: twenty-seventh William Smith Lecture. *Journal of the Geological Society, London* **130**, 183–204.

Robinson, A. G., Banks, C. J., Rutherford, M. M. & Hirst, J. (1995). Stratigraphic and structural development of the Eastern Pontides, Turkey. *Journal of the Geological Society* **152**, 861–872.

Rolland, Y., Hässig, M., Bosch, D., Bruguier, O., Melis, R., Galoyan, G., Topuz, G., Sahakyan, L., Avagyan, A. & Sosson, M. (2020). The East Anatolia–Lesser Caucasus ophiolite: an exceptional case of large-scale obduction, synthesis of data and numerical modeling. *Geoscience Frontiers* **11**, 83–108.

Rowe, M. C., Kent, A. J. R. & Nielsen, R. L. (2009). Subduction Influence Oxygen Fugacity and Trace and Volatile Element in Basalts Across the Cascade Volcanic Arc. *Journal of Petrology* **50**, 61–91.

Russell, W. A., Papanastassiou, D. A. & Tombrello, T. A. (1978). Ca isotope fractionation on the Earth and other solar system materials. *Geochimica et Cosmochimica Acta* **42**, 1075–1090.

Rutherford, M. J. & Devine, J. D. (2003). Magmatic conditions and magma ascent as indicated by hornblende phase equilibria and reactions in the 1995–2002 Soufrière Hills magma. *Journal of Petrology* **44**, 1433–1453.

Sano, Y., Nishio, Y., Gamo, T., Jambon, A. & Bernard, M. (1998). Noble gas and carbon isotopes in Mariana Trough basalt glasses. *Applied Geochemistry* **13**, 441–449.

Schmidt, M. W. & Poli, S. (1998). Experimentally based water budgets for dehydrating slabs and consequences for arc magma generation. *Earth and Planetary Science Letters* **163**, 361–379.

Schmidt, M. W. & Jagoutz, O. (2017). The global systematics of primitive arc melts. *Geochemistry, Geophysics, Geosystems* **18**, 2817–2854.

Şen, C. (2007). Jurassic volcanism in the Eastern Pontides: is it rift related or subduction related? *Turkish Journal of Earth Sciences* **16**, 523–539.

Şengör, A. M. C. & Yilmaz, Y. (1981). Tethyan evolution of Turkey: a plate tectonic approach. *Tectonophysics* **75**, 181–241.

Şengör, A. M. C., Yilmaz, Y. & Ketin, I. (1980). Remnants of a pre-Late Jurassic ocean in northern Turkey: fragments of Permian–Triassic Paleo-Tethys? *Geological Society of America Bulletin* **91**, 599–609.

Şengör, A. M. C., Özeren, M. S., Keskin, M., Sakınç, M., Özbakır, A. D. & Kayan, İ. (2008). Eastern Turkish high plateau as a small Turkic-type orogen: implications for post-collisional crust-forming processes in Turkic-type orogens. *Earth-Science Reviews* **90**, 1–48.

Shervais, J. W. (1982). Ti–V plots and the petrogenesis of modern and ophiolitic lavas. *Earth and Planetary Science Letters* **59**, 101–118.

Sinton, J. M. & Fryer, P. (1987). Mariana Trough lavas from 18°N: implications for the origin of back arc basin basalts. *Journal of Geophysical Research* **92**, 12782–12802.

Sisson, T. & Grove, T. (1993). Experimental investigations of the role of H_2O in calc-alkaline differentiation and subduction zone magmatism. *Contributions to Mineralogy and Petrology* **113**, 143–166.

Sisson, T. W., Ratajeski, K., Hankins, W. B. & Glazner, A. F. (2005). Voluminous granitic magmas from common basaltic sources. *Contributions to Mineralogy and Petrology* **148**, 635–661.

Sláma, J., Košler, J., Condon, D. J., Crowley, J. L., Gerdes, A., Hanchar, J. M., Horstwood, M. S. A., Morris, G. A., Nasdala, L., Norberg, N., Schaltegger, U., Schoene, B., Tubrett, M. N. & Whitehouse, M. J. (2008). Plešovice zircon—a new natural reference material for U–Pb and Hf isotopic microanalysis. *Chemical Geology* **249**, 1–35.

Stern, R. J. & Bibee, L. D. (1984). Esmeralda Bank: geochemistry of an active submarine volcano in the Mariana Island Arc. *Contributions to Mineralogy and Petrology* **86**, 159–169.

Stern, R. J., Bloomer, S. H., Lin, P.-N. & Smoot, N. C. (1989). Submarine arc volcanism in the southern Mariana Arc as an ophiolite analogue. *Tectonophysics* **168**, 151–170.

Stern, R. J., Lin, P.-N., Morris, J. D., Jackson, M. C., Fryer, P., Bloomer, S. H. & Ito, E. (1990). Enriched back-arc basin basalts from the northern Mariana Trough: implications for the magmatic evolution of back-arc basins. *Earth and Planetary Science Letters* **100**, 210–225.

Stern, R. J., Kohut, E., Bloomer, S. H., Leybourne, M., Fouch, M. & Vervoort, J. (2006). Subduction factory processes beneath the Guguan cross-chain, Mariana Arc: no role for sediments, are serpentinites important? *Contributions to Mineralogy and Petrology* **151**, 202–221.

Sun, S. S. & McDonough, W. F. (1989). Chemical and isotopic systematics of oceanic basalts: implications for mantle composition and processes. In: Saunders, A. D. & Norry, M. J. (eds) *Magmatism in the Ocean Basins. Geological Society, London, Special Publications* **42**, 313–345.

Tamura, Y., Ishizuka, O., Stern, R. J., Shukuno, H., Kawabata, H., Embley, R. W., Hirahara, Y., Chang, Q., Kimura, J. I., Tatsumi, Y., Nunokawa, A. & Bloomer, S. H. (2011). Two primary basalt magma types from northwest Rota-1 volcano, Mariana Arc and its mantle diapir or mantle wedge plume. *Journal of Petrology* **52**, 1143–1183.

Tatsumi, Y., Takahashi, T., Hirahara, Y., Chang, Q., Miyazaki, T., Kimura, J. I., Ban, M. & Sakayori, A. (2008). New insights into andesite genesis: the role of mantle-derived calc-alkalic and crust-derived tholeiitic melts in magma differentiation beneath Zao Volcano, NE Japan. *Journal of Petrology* **49**, 1971–2008.

Topuz, G., Altherr, R., Satır, M. & Schwarz, W. H. (2004). Low-grade metamorphic rocks from the Pulur complex, NE Turkey: implications for the pre-Liassic evolution of the Eastern Pontides. *International Journal of Earth Sciences* **93**, 72–91.

Topuz, G., Altherr, R., Schwarz, W. H., Dokuz, A. & Meyer, H. P. (2007). Variscan amphibolite-facies rocks from the Kurtoğlu metamorphic complex (Gümüşhane area, Eastern Pontides, Turkey). *International Journal of Earth Sciences* **96**, 861–873.

Topuz, G., Celik, O. F., Sengor, A. M. C., Altintas, I. E., Zack, T., Rolland, Y. & Barth, M. (2013). Jurassic ophiolite formation and emplacement as backstop to a subduction–accretion complex in northeast Turkey, the Refahıye ophiolite, and relation to the Balkan ophiolites. *American Journal of Science* **313**, 1054–1087.

Ulmer, P. (1988). High-pressure phase equilibria of a calc-alkaline picro-basalt: implications for the genesis of calc-alkaline magmas. *Carnegie Institution of Washington Yearbook* **87**, 28–35.

Ulmer, P., Kaegi, R. & Müntener, O. (2018). Experimentally derived intermediate to silica-rich arc magmas by fractional and equilibrium crystallization at 1·0 GPa: an evaluation of phase relationships, compositions, liquid lines of descent and oxygen fugacity. *Journal of Petrology* **59**, 11–58.

Ustaömer, T., Robertson, A. H. F., Ustaömer, P. A., Gerdes, A. & Peytcheva, I. (2013). Constraints on Variscan and Cimmerian magmatism and metamorphism in the Pontides (Yusufeli–Artvin area), NE Turkey from U–Pb dating and granite geochemistry. In: Robertson, A. H. F., Parlak, O., and Ünlügenç, U. C. (ed.) Geological development of Anatolia and the easternmost Mediterranean region. Geological Society, London, Special Publications 372, 49.

Uysal, I., Ersoy, E. Y., Dilek, Y., Escayola, M., Sarıfakıoğlu, E., Saka, S. & Hirata, T. (2015). Depletion and refertilization of the Tethyan oceanic upper mantle as revealed by the early Jurassic Refahiye ophiolite, NE Anatolia—Turkey. *Gondwana Research* **27**, 594–611.

Vermeesch, P. (2012). On the visualisation of detrital age distributions. *Chemical Geology* **312–313**, 190–194.

Villiger, S., Ulmer, P., Müntener, O. & Thompson, A. B. (2004). The liquid line of descent of anhydrous, mantle-derived, tholeiitic liquids by fractional and equilibrium crystallization—an experimental study at 1·0 GPa. *Journal of Petrology* **45**, 2369–2388.

Villiger, S., Ulmer, P. & Müntener, O. (2006). Equilibrium and fractional crystallization experiments at 0·7 GPa; the effect of pressure on phase relations and liquid compositions of tholeiitic magmas. *Journal of Petrology* **48**, 159–184.

Volpe, A. M., Douglas Macdougall, J. & Hawkins, J. W. (1987). Mariana Trough basalts (MTB): trace element and Sr–Nd isotopic evidence for mixing between MORB-like and arc-like melts. *Earth and Planetary Science Letters* **82**, 241–254.

Wade, J. A., Plank, T., Stern, R. J., Tollstrup, D. L., Gill, J. B., O'Leary, J. C., Eiler, J. M., Moore, R. B., Woodhead, J. D., Trusdell, F., Fischer, T. P. & Hilton, D. R. (2005). The May 2003 eruption of Anatahan volcano, Mariana Islands: geochemical evolution of a silicic island-arc volcano. *Journal of Volcanology and Geothermal Research* **146**, 139–170.

Walker, B. A., Bergantz, G. W., Otamendi, J. E., Ducea, M. N. & Cristofolini, E. A. (2015). A MASH zone revealed: the mafic complex of the Sierra Valle Fértil. *Journal of Petrology* **56**, 1863–1896.

Wiebe, R. A. & Collins, W. J. (1998). Depositional features and stratigraphic sections in granitic plutons: implications for the emplacement and crystallization of granitic magma. *Journal of Structural Geology* **20**, 1273–1289.

Wiedenbeck, M., Allé, P., Corfu, F., Griffin, W. L., Meier, M., Oberli, F., Quadt, A. V., Roddick, J. C. & Spiegel, W. (1995). Three natural zircon standards for U–Th–Pb, Lu–Hf, trace element and REE analyses. *Geostandards and Geoanalytical Research* **19**, 1–23.

Woodhead, J., Hergt, J., Shelley, M., Eggins, S. & Kemp, R. (2004). Zircon Hf-isotope analysis with an excimer laser, depth profiling, ablation of complex geometries, and concomitant age estimation. *Chemical Geology* **209**, 121–135.

Woodhead, J., Hergt, J., Greig, A. & Edwards, L. (2011). Subduction zone Hf-anomalies: mantle messenger, melting artefact or crustal process? *Earth and Planetary Science Letters* **304**, 231–239.

Workman, R. K. & Hart, S. R. (2005). Major and trace element composition of the depleted MORB mantle (DMM). *Earth and Planetary Science Letters* **231**, 53–72.

Yilmaz, Y., Tüysüz, O., Yigitbas, E., Can Genç, S. & Sengör, A. M. C. (1998). Geology and tectonic evolution of the Pontides. In: Robinson A. G. (ed) Regional and petroleum geology of the Black Sea and surrounding, AAPG Memoir 68, 183–226.

Zhang, L. L., Zhu, D. C., Wang, Q., Zhao, Z. D., Liu, D. & Xie, J. C. (2019). Late Cretaceous volcanic rocks in the Sangri area, southern Lhasa Terrane, Tibet: evidence for oceanic ridge subduction. *Lithos* **326–327**, 144–157.

Zimmer, M. M., Plank, T., Hauri, E. H., Yogodzinski, G. M., Stelling, P., Larsen, J., Singer, B., Jicha, B., Mandeville, C. & Nye, C. J. (2010). The role of water in generating the calc-alkaline trend: new volatile data for Aleutian magmas and a new tholeiitic index. *Journal of Petrology* **51**, 2411–2444.